DESIGN REPORT FOR PRR

OUTER CYLINDER

Equipment/system description:

The Outer Cylinder is the primary integration structure of the ATLAS ITk, it provides structural support to the Strip Barrel shells, the inner most of which is also the Pixel Support Tube, and to the Strip Endcaps. It also provides a gas enclosure and faraday cage for the ITk.

This report describes the performance of an integrated model of the ITk Global support structures within the Outer Cylinder. This version includes nominal Pixel Interface loads. It will be updated in conjunction with ITk Pixel Global Support FDR ~March 2021 to include performance of the 'PST' which is also 'L0' of the Strip Barrel.

Associated Documents:

Document:	**Reference:**
System specification	AT2-IG-ES-0001

TRACEABILITY

Main Author(s): Giorgio VALLONE, Eric ANDERSSEN
Other Authors: D. Boettcher, T. Claybaugh, C. Evans, N. Hartman, M. Janda

Checked by:	**Date:**
M. Vreeswijk, I. Wilmut	

Approved by:	**Date:** 2019-12-11
Released for Information	

Rev. No.	*Date*	***Description of Changes** (major changes only, minor changes in EDMS)*
V1	2018-11-16	Initial release for review Nov-2018
V2	2019-06-04	Second release for follow up review June-2019
V3	2019-12-x	Third release for PRR December-2019

This document is uncontrolled when printed. Check the EDMS to verify that this is the correct version before use

CONTENTS

This document is uncontrolled when printed. Check the EDMS to verify that this is the correct version before use

This document is uncontrolled when printed. Check the EDMS to verify that this is the correct version before use

This document is uncontrolled when printed. Check the EDMS to verify that this is the correct version before use

Nomenclature and Definitions:

AB:	Argon Barrel (includes Solenoid and Tile Calorimeter)
ABS:	Assembly Breakdown Structure
AE:	Liquid Argon Endcap (includes Tile Calorimiter)
ACL:	Acceptance Criterial List
ANSYS:	Finite Element Analysis Software
A-Side:	-Z direction of ATLAS (direction Aeroport)
ASD:	Acceleration Spectral Density (g^2/Hz)
Barrel:	Central Part of ITk
BSM:	Barrel Service Module
C-Sid:	+Z direction of ATLAS (direction Charlie's)
CAD:	Computer Aided Design
CDD:	CERN Drawing Database
EC:	Endcap
EDMS:	Engineering/Electronic Document Management System at CERN
EMI:	Electro Magnetic Interference (in reference to Faraday Cage)
FDR:	Final Design Review
FE:	Finite Element
FEM:	Finite Element Model
Forward:	Higer |Z| components
HGDT:	High Granularity Tracking Detector (Timing detector monted to AE)
ICD:	Interface Control Document/Drawing
ID:	Inner Detector (Replaced by ITk)
ITk:	Inner Tracker (Phase II Upgrade)
IWV:	Inner Warm Vessel of the AB
LS2:	Long Shutdown 2 (maintenance period of LHC 2019-2021)
LS3:	Long Shutdown 3 (maintenance period of LHC 2024-2027)
MLI:	Multi Layer Insulation (aluminized kapton)
MPC:	Multi Point Constraint
OC:	Outer Cylinder
OSV:	Outer Service Volume
PRR:	Production Readiness Review
NCR:	Non Conformace Report
PDM:	Product Data Management
PM:	Polymoderator required to reduce radiation background
PP1:	Patch Panel 1 (Strip Barrel/EC andPixel)
PST:	Pixel Support Tube
SB:	Structural Bulkhead
SR1:	Surface Integration Cleanroom at Point 1
TC:	ATLAS Technical Coordination
Type 2/II:	Services external to the ITk detector volume attached to PP1 in OSV
VI:	Beampipe (Vaccuum Chamber, Inner)
WI:	Work Instructions
Windchill:	LBNL PDM Database

This document is uncontrolled when printed. Check the EDMS to verify that this is the correct version before use

0 CHANGELOG AND HISTORY

The present document is the third version of the Outer Cylinder design report. The first version was released for the first FDR in November 2018. The second version was released for the second FDR in June 2019. The version contained the following major additions:

- Section 4 with a detailed description of the new strip barrel FE model and the experimental test results;
- Section 5, containing the description and the results from the integrated FE model analysis;
- Section 6 (now section 7), containing the result summary and the answer to the action items outlined by the reviewers in the first FDR.

This third updated version was released before the PRR in November 2019. The following parts were added to the document:

- Section 4.3, containing new experimental results relative to the strip barrel mechanical performances;
- Section 6, detailing the variations made to the design to prepare it for production, along with the additional FE analyses performed in order to guarantee similar performances to the FDR design;
- Section 7.2, containing the answer to the relevant recommendations from the second FDR follow-up.

The review material can be found at the following locations:

- 1st FDR: https://indico.cern.ch/event/768533/
- 2nd FDR: https://indico.cern.ch/event/813218/
- PRR: https://indico.cern.ch/event/854551/

1 OVERVIEW

The Outer Cylinder is the primary integration structure for the Phase II upgrade Inner Tracker (ITk). It supports all detectors of the ITk, with an internal barrel portion of the neutron polymoderator (PM), and provides elements for a sealed gas environment, and the ITk Faraday cage. Its primary mechanical interfaces are to the ATLAS Argon Barrel Cryostat Inner Warm Vessel (AB IWV), via rails designed and provided by ATLAS Technical Coordination (TC). A similar interface (cradle with similar IWV rail segments) is replicated on the surface during ITk integration. All sub-detectors will be assembled and installed on the surface into the OC in SR1 (cleanroom near Point 1), and the ITk will be lowered as a complete package into the ATLAS pit. Lift points near the rail interface are provided on the OC for this transfer.

Internal mechanical interfaces include support of the Strip Barrel and their service modules, rails to support and insert the Strip Endcaps, and ties via the Structural Bulkhead to all service penetrations for Strip and Pixel Detectors at their first patch panel (PP1).

The envelope of the OC is controlled by an envelope model/drawing and accounts for insertion clearances for detectors and service envelopes internally. External envelopes are driven both by final insertion of the ITk package into the IWV, as well as clearances during lowering into the ATLAS Cavern which has an envelope for both the ITk package, and the lift fixture (dummy test during LS2). Additionally, the length of the OC was driven by detector service routing in the Outer Service Volume (OSV) of the Type 2 services of the Pixel and Strip detectors

This document is uncontrolled when printed. Check the EDMS to verify that this is the correct version before use

The OC is required at CERN in SR1 by spring of 2021 for the onset of Strip Barrel integration. The Production Readiness Review (PRR) is planned for October 2019 in anticipation of release for production in early 2020.

1.1 Scope

This document covers the design details and structural performance of the ITk Outer Cylinder (OC), and describes the loads that the structure must support. These are primarily the Strip Barrel, its Service Modules, and the Strip Endcap (Strip Endcap Services are integrated with its structure and the Structural Bulkhead). The Structural Bulkhead (SB) which helps to hold the OC round at the extremities, and forms the rest of the gas and EMI enclosure is included in the structural performance; it has significant interfaces to Strip and Pixel Patch Panels (PP1). The contributions of the SB to the structural performance of the Integrated models are primarily in |Z| stiffness. Auxiliary tooling is required to hold the OC round during assembly facilitating later mechanical assembly of the SB, this will be described. Dry fit of the SB and their corresponding OC Forward flanges is foreseen prior to shipment of the SB to DESY and NIKHEF for incorporation into their respective Strip Endcaps.

Strength considerations are covered—the OC is largely a composite structure designed for low deflections, thus low mechanical strain, excepting locations of load introduction (mount pads). These will have metallic inserts and will have prototype materials and interfaces tested to failure during prototype phase after the FDR, prior to production

Interfaces to the IWV rails and lift/transfer procedures will be treated in a separate document under preparation; interfaces to that operation will be finalized after addressing any issues raised during the FDR. A test lift of a physical envelope model of the ITk was conducted in the early phases of LS2.

It is assumed that this document will be updated with performance data from prototypes, both for material properties and stress allowances in preparation for the PRR. ‘Value Engineering’ will also be considered in progression toward the PRR. Vendors may propose alternate fabrication techniques that can meet the performance criteria of the design presented here, e.g. splitting the OC shell into segments versus a complete cylindrical shell with segments assembled on tooling. These will be addressed at the PRR if any changes are accepted during the proposal process.

2 DESIGN DESCRIPTION

2.1 Summary Specifications

The primary specification that can be assessed independently is the gravity sag under applied loads (sub-detector masses). This is related to the stability requirement described in the ‘Alignment and positioning requirements for the ATLAS phase II tracker’ EDMS document ATU-SYS-ES-0027 which stipulates a 2 μm short term stability. Short term stability is described in that document, but in the broad sense applies to vibration and is the most stringent requirement. Photon conversion data from the existing ID Pixel detector shows that with 50 μm gravity sag, the detector is stable at under 0.2 μm which is consistent with the Miles equation and our measured vibration spectrum presented in section 5.9.

Other requirements in the specification document relate to gas and EMI seals, which cannot be validated independent of a whole system. The OC flanges can be verified to meet sealing and EMI compatibility independently with prototype measurements of sealing, and simple resistance measurements across interface gaps (flanges).

This document is uncontrolled when printed. Check the EDMS to verify that this is the correct version before use

2.2 Envelope Model

The envelope model is maintained in CATIA and is available in neutral 3D CAD and as a drawing in EDMS document AT2-IC-EP-0001 it is the primary method to communicate mechanical interfaces within the ITk. It will be released and subject to change control after the FDR. It includes the envelope models of the Argon Barrel and Endcap (AB/AE), which are controlled by ATLAS TC and will shortly be in the released/approved state due to ties to older models in EUCLID, so can be released to CDD. TC is working on a solution to allow us to release this via Smart Team (CATIA PDM) to CDD to then follow the normal CERN release procedure.

It should be noted that the length of the ITk was shortened by 15 cm on each end between the specification review and the FDR to account for service routing in the regions of PP1 and to allow for installation of the HGTD which required 6 cm incursion into the original ID envelope. The envelope model has also changed since the previous review to increase the OD of the OC by 8mm and re-distribute internal insertion clearances for the Strip Endcap. That ECR has been approved by ITk and is awaiting approval by the USC. Once approved, the Envelope model v1.9 will be released as v2.0 and approved via EDMS/CDD, with changes afterward requiring an ECR.

The Envelope model will be the primary ICD for most of the ITk and neighbouring detectors. ICD's specific to internal sub-systems, in particular ones requiring phi information and dimensions will be generated and controlled separately. Their geometry will be included in the Envelope Model, but not the 2D section referred to as the Envelope Drawing.

This document is uncontrolled when printed. Check the EDMS to verify that this is the correct version before use

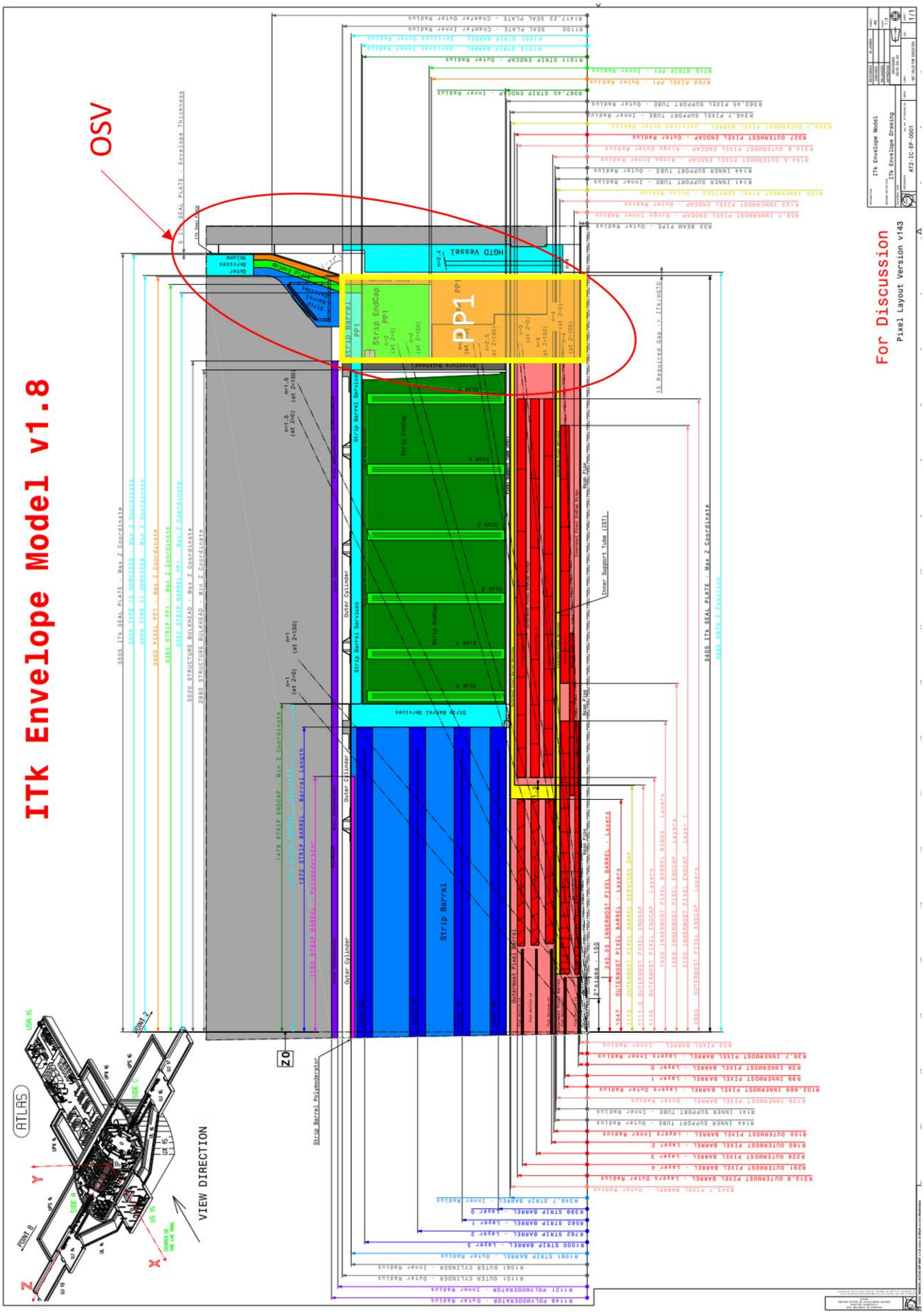

Figure 1 ITk Envelope Drawing

This document is uncontrolled when printed. Check the EDMS to verify that this is the correct version before use

2.3 Outer Cylinder Design Considerations

The OC is required to allow integration of the ITk on the surface in SR1, rather than the method used on the current Inner Detector (ID). The ID was assembled in Barrel and Endcaps, each were installed and serviced separately inside the IWV. The ID Pixel system was then installed in the ID PST after the other 3 systems (Barrel, Endcap A, Endcap C) were installed. The ID Barrel had to be connected to its service chain inside the IWV before either endcap, and Pixel insertion followed most of the service connection of both Endcaps. This process took 3 years underground working inside the IWV. LS3 is presently 30 months, and the areas near the IWV will be activated.

The OC is intended as an analog for the IWV allowing all sub-detectors of the ITk to be assembled on the surface instead of the activated regions in the cavern. The ITk package will present bulkhead connectors at its extremities (PP1) that should allow for rapid connection after the ITk package is lowered and inserted. The termination of the services is expected to take ~12 weeks, if they are installed prior to detector lowering (schedule under discussion with TC).

Another function of the OC is to provide the outer radius of a faraday cage, and to maintain a dry gas environment inside the ITk volume, the SB and Pixel PP1 close the ends of the Faraday Cage, and terminate to a foil on the Beam Pipe (VI) which forms the inner radius of the Faraday Cage. Additionally, when the OC is on the surface in SR1, several cold tests will be performed. The OC will have heaters integrated into the shell that will provide some few kW heating to maintain the surface temperature above the dewpoint. On the surface these will operate continuously, in the cavern, they will only operate if the OSV is open, and the detector is cold.

2.3.1 Layout of the Outer Cylinder main structural components

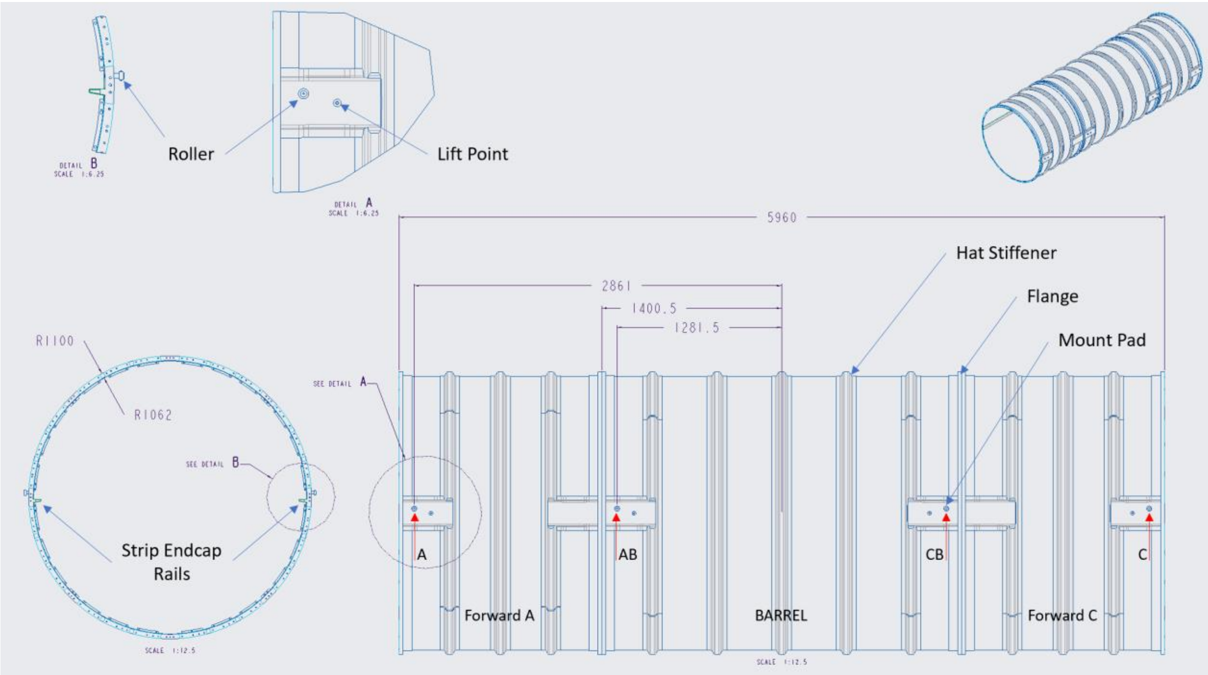

Figure 2 Outer Cylinder Features and Load Points

The OC is composed of 3 similar cylinders, the Barrel, Forward A, and Forward C. Each are terminated with CFRP end flanges, that have location features machined into them to position each assembly relative to the others, and to define precision mount points internally to allow precise placement of the detector elements to machined component precision. The Barrel Flanges join to mating Barrel End Flanges on each forward shell via through-hole M8 Ti fasteners, with 2 M8 pins on diameter at +/- X. There will be a Viton O-ring for a gas seal, and an EMI O-ring to

This document is uncontrolled when printed. Check the EDMS to verify that this is the correct version before use

assure electrical contact between the 3 shells. Each shell is stiffened with 'Hat Stiffeners', and reinforced at the load introduction locations with 'Mount Pads.' The Mount pads in 4 locations per side (A, AB, CB, C) in figure above have titanium Studs where plane roller bearings are installed, and nearby have titanium inserts to install lift buckles. Two of the rollers, (A,C) on the +X side are Vee shaped with the rest flat to not over-constrain the motion. Inside of the two Forward shells are rails that will allow the Strip Endcaps (A/C) to be installed, similarly these will have V and Flat rails, with only 2 rollers per side.

The laminates are in general quasi-isotropic, with all Mount Pads, and Hat Stiffeners produced from CN60 or equivalent fiber in a cyanate ester matrix (EX1515). This is a 650 GPa modulus fiber, with a QIBS modulus of 130 GPa. The shells will similarly be CN60, with an equivalent hoop modulus of 130 GPa. Final laminates will be designed after deflection and strength testing of the load introduction points. A segment of shell, flange, hat-stiffener, and mount pads will be fabricated with nominal laminates as described, with some articles tested to failure. Results will feed back into the design for fabrication after these results are available from vendor prototypes.

2.3.2 Roller and Lift Point Design

Rollers are used to reduce the friction required to insert the ITk into the IWV on Vee and Flat rails. The radial envelope has an insertion gap of 10 mm, in which TC may require the ITk to be 'positioned'. The internal clearances of the ITk detectors are such that no internal adjustment is allowed, so that the Beampipe (VI) is fixed on nominal detector center. The machine requires VI to be located on nominal beam axis (concentric with) to an envelope of 4 mm Diameter [1]. The Argon Barrel, which holds the IWV can be adjusted vertically if required, horizontal adjustment of the ITk can be achieved by replacing the Vee roller with a nominal offset in X. This must be surveyed and determined before lowering to allow roller replacement. Similarly, if a vertical (Y) fine adjustment is required, rollers of different diameters can be installed.

The rollers themselves are plain sleeve bushings of Vespel pressed into 304 Stainless Steel rollers. The Plain bearing rides directly on the titanium studs and is captured by a cap, and shoulder on the stud.

$$D_{shaft} = 0.625\ in$$

$$L_{shaft} = 0.74\ in$$

$$Load = 500\ kgf$$

$$P = \frac{Load}{D_{shaft}L_{shaft}} = 2.352x10^3\ psi$$

$$P_{allowable} = 4900\ psi$$

$$\frac{P_{allowable}}{P} = 2.084$$

Apologies for units, bushing selected from Bunting Bushing Engineering Catalog, in Imperial units. The allowable load is pulled directly from their catalog in psi, so for tracability of the calculation, imperial units were used. A factor of safety of 2 against the largest static reaction load is achieved. Depending on final design of rollers, a Vespel bearing may be machined in-house if additional features are required versus a simple bushing. The coefficient of friction is under 0.1 so with an overall mass of ~3.2 T, a traction force of 320 kgF is required.

This document is uncontrolled when printed. Check the EDMS to verify that this is the correct version before use

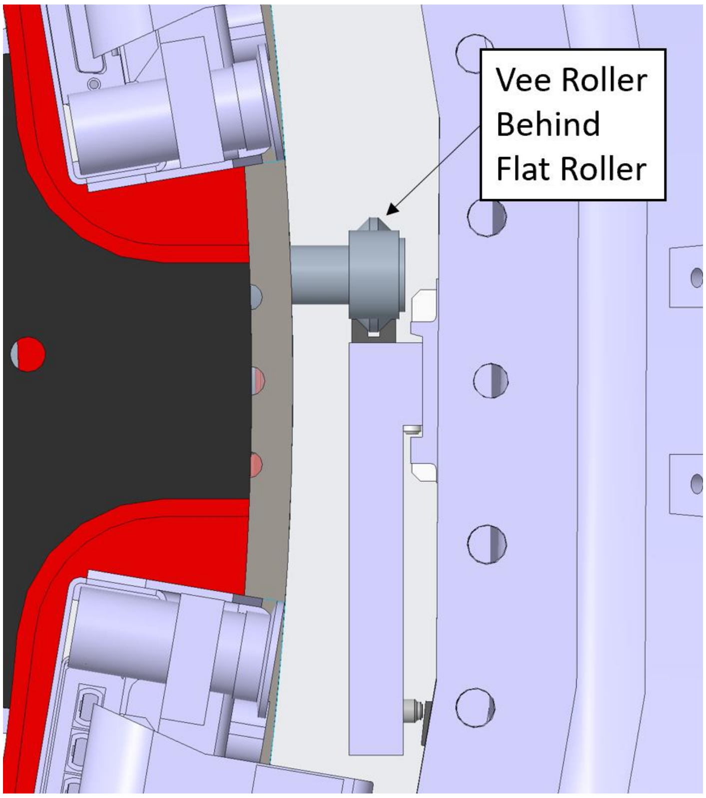

Figure 3 Rollers shown on Inner Warm Vessel Rail

The Rail design for the IWV Vee rail, will be discussed with TC to allow a larger flat surface for the flat roller on top of the Vee rail. If the ITk is required to be installed off-center, the rollers will be machined just prior to lowering and after a final survey of the ITk, and the nominal beam axis, which will have changed due to replacement of the focusing quadrupoles installed for HL-LHC upgrade.

2.3.3 Heater and Faraday Cage Design

It has not been determined if heater/faraday panels will be co-cured in each shell or laminated onto the shells afterward. This will be a discussion with the vendor after a market survey. For the purpose of this discussion, it will be assumed that they are co-cured. The Faraday cage is required to be conductivity equivalent to a continuous sheet of 36.4 μm Copper foil (one-ounce Cu in flex-circuit terminology). Specially made carbon fiber laminates, with layers separated at the edges for individual electrical contact, have been tested for electrical conductivity with results showing that all layers within the laminate are electrically in contact with each other, and that ~3.5mm thickness of a CFRP laminate is equivalent to one-ounce copper. As the shell laminate of the OC may be as thin as 2.5mm (3mm nominal), this is not quite enough to meet the conductivity requirement. Addition of an independent layer of one ounce Cu foil independent of the contribution from the CFRP allows for meeting the conductivity requirement of the Faraday Cage.

The proposed design for heater pads will require splicing them electrically. They will be fabricated as flexible circuits at the maximum panel size available (TBD), but ~ 0.6m X 1.2m have been acquired before. These panels will have heater traces on one side, and an edge exposed Cu foil on the other, as illustrated below. The Anti-static mat is a 35μm non-woven product with a mix of fiberglass and carbon fiber. It has been used to construct CFRP electro-static shrouds tested up to 6 kV/cm fields with no sign of corona, demonstrating that it provides excellent surface conductivity, a good electrical tie to the underlying laminate, and does not produce stray fiber

This document is uncontrolled when printed. Check the EDMS to verify that this is the correct version before use

asperities even when sanded into to remove surface resin, else it would not have held off corona. This will be used to assure strong electrical contact of the laminate with the copper ground plane.

The heater pads will be installed with gaps to provide defined placement tolerance within the laminate with no overlap, allowing direct access to the exposed ground plane for a splice with copper tape. The adhesive in Cu Tape is filled with Cu particles to assure conductivity but is not deemed radiation tolerant. The splice tape will be held in place with Kapton strip glued in place with structural epoxy known to be radiation tolerant.

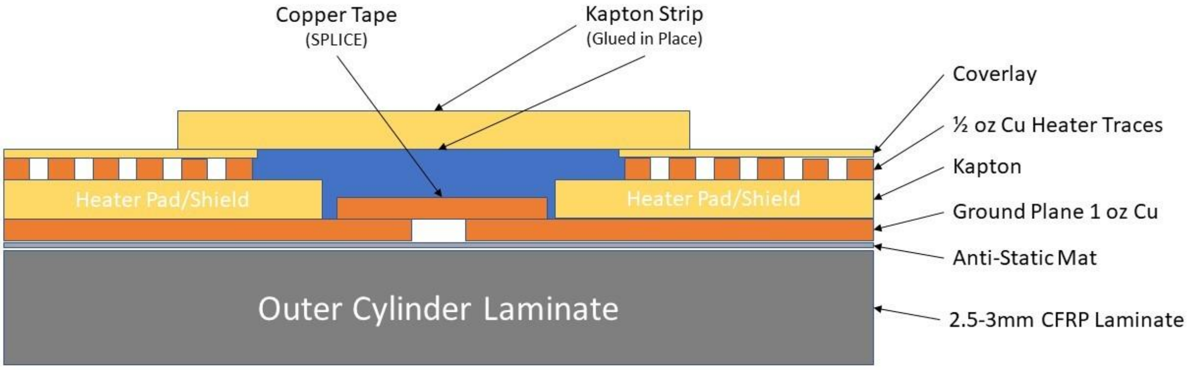

Figure 4 Heater Pad Ground Plane Splice Detail

The external connectivity of the heaters has not been designed but will use a similar design to the currently installed and operating ID PST [2]. These heater pads had half-ounce Cu traces, 0.75mm wide laid out in a serpentine path. The ampacity of traces of this width with a 20C temperature rise is 1.5A in air, it is much higher when laminated to a conductive substrate such as the OC shell laminate. The traces are ganged with 5 in parallel. The current required to provide sufficient heat is 0.3A/trace (1.5A/circuit). This sizing allows for a trace to fail, in fact one trace can carry the full current delivered, operating hotter thus dissipating the same power. Tests showing the performance of heater panels with specifically open traces were performed for the original PST including loss of an entire panel (unlikely failure scenario due to trace redundancy). The thermal boundary conditions are the same for the ITk, e.g. internal gas temperature of -25C, and a dewpoint of +15C externally.

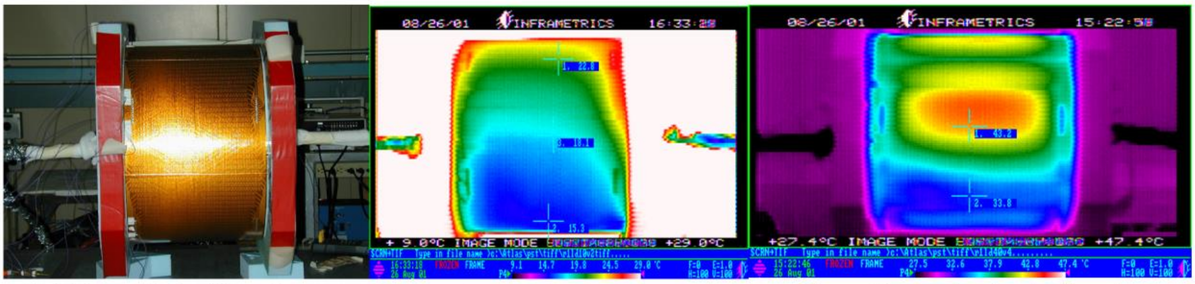

Test Setup with 6m 12mm Cu tubing coiled inside with -25C coolant temperature

Thermal Image showing heaters at 20% full power just meets dewpoint requirement in free convection

Thermal Image showing heaters at 80% with fully disabled panel on bottom (worst case)

Figure 5 PST Heater thermal reliability study

The thermal images above show that nominal power requirement of 20% of the ampacity gives required performance for fully working heaters in free convection (open air)—this is nominally the case in SR1, but can be improved with a few layers of MLI (Multi-Layer Insulation) to cut off most of the convective losses, reducing power requirements. The image on the left completely

This document is uncontrolled when printed. Check the EDMS to verify that this is the correct version before use

disabled the heater pad on the bottom, which is the worst case as this is the coldest region due to thermal striation of the gas internal to the volume. This indicates that the thermal conductivity of the CFRP Shell is sufficient to distribute heat from failed traces, or heater pads, with nominally increased power. It also indicates that for reduced power input to the detector that the heaters should be powered in zones, e.g. Top/Middle(Sides)/Bottom, and that temp sensors should be redundant and current controlled globally, not by zone in case one fails.

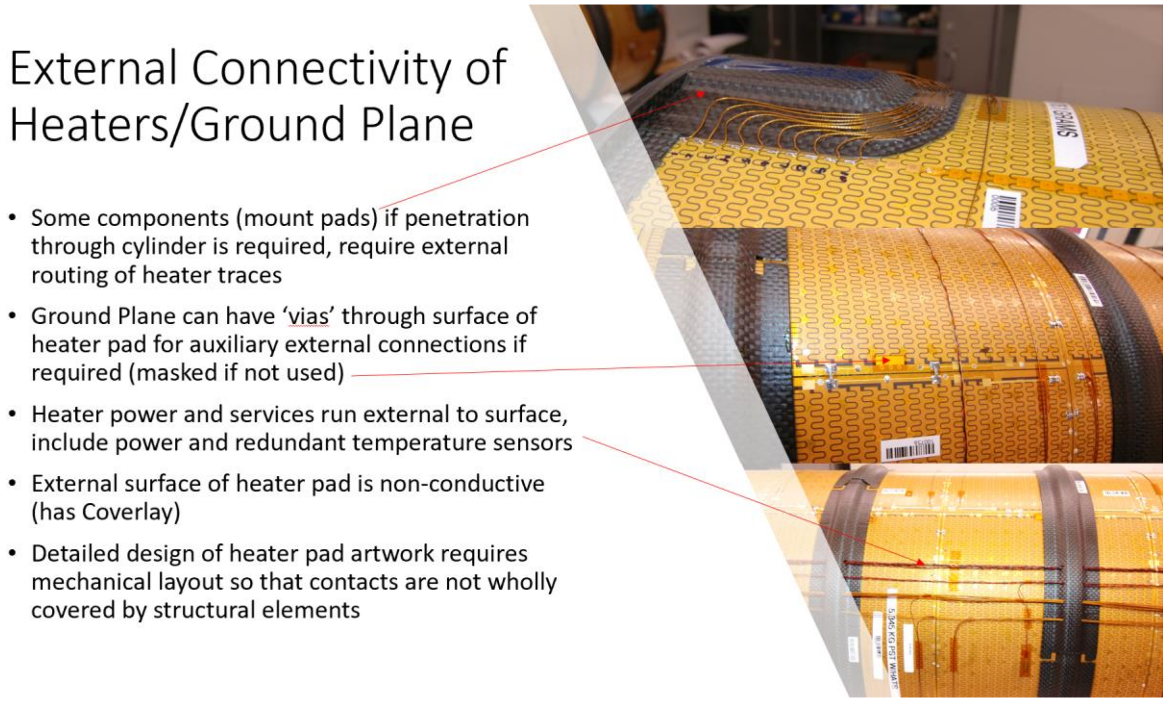

Figure 6 External Connectivity of Heaters and Ground Plane

As seen in the above figure, the heater pads are part of the shell laminate. The flex circuits used will have epoxy adhesive rather than the more common acrylic. These laminates including heater pad flex have been tested in thickly adhered shear tests (ASTM D695) showing no preference for failure in the heater interfaces during the original PST construction. As noted above, detailed layout of the circuits and their external connection needs to assure that relevant pads are not covered by structural elements. Detailed design of circuit layout to minimize the number of configurations will follow the FDR in conjunction with vendor RFP.

2.3.4 Internal Structural Interface to Strip Barrel Shell

As mentioned above in 2.3.1, the Strip Barrel and Endcaps have mounts internal to the OC. For the Strip Barrel Shells, 8 interlinks mount to radial protrusions inside of the OC Barrel Flange at +/-X and support the largest of the shells near the diameter of the flange, and ~1.4m |Z| with approximately 90mm length interlinks shown in figure below. 8 are required (+/- Y) in each of the four locations to allow removal of one or the other to give clearance for insertion of a Strip Barrel Stave (primary detecting element). In the final configuration, only 4 of the 8 brackets are installed. Not shown in Figure 7 is the rail required to insert the Strip Endcaps. This rail mechanically interferes with stave insertion in this location so will be installed after completion of the Strip Barrel Integration. It should be noted that flexure in the OC during loading amounts to 'rotation' of the interlink interface to the Strip Barrel Shell assembly. For the fully loaded detector, this rotation component, projected by the 90mm interlink length, contributes to 110 μm of the vertical displacement. This flexure in the OC increases as subsequent Strip Barrel layers are added, but after the Polymoderator (PM) is installed which is about 300kg mass. The Strip Barrel

This document is uncontrolled when printed. Check the EDMS to verify that this is the correct version before use

is ~650kg and its services an additional ~400kg, representing most of the load, and increases finally as the Strip Endcaps and finally the Pixel detector are installed. It is desirable to constrain only one of the two interlinks shown below for position, allowing the other to 'slide' such that a moment load is not introduced into the largest Strip Barrel Shell as mass is added during Strip Barrel assembly. A procedure shall be developed to minimize this potential load and has been analysed in the load cases presented in section 5.1177. A mitigating strategy is that during assembly, direct access to these interlinks is available until the Strip Endcaps, and Pixel detector is installed, locking the other interlink in shear (by bolted preload) at the end of Barrel integration. Of the ~1000kg load at each barrel end, only 175kg additional load is added by installing the Strip Endcaps and Pixel detector. Local strains can be managed during assembly by not locking one of the two interlinks until just prior to Strip Endcap insertions and removing them prior to closing the detector. This potential 100 μm rotation strain in the Strip Barrel largest cylinder could then be limited to 175/1000 i.e. 18 μm localized radial displacements in the outer Strip Barrel Shell. This is considered in the calculations of the Strip Barrel Shells, and stress calculations in their mount flanges The numbers are small, so should not represent major impact in stress to either design or procedure, but should be accounted for at the interface during detail design for fabrication.

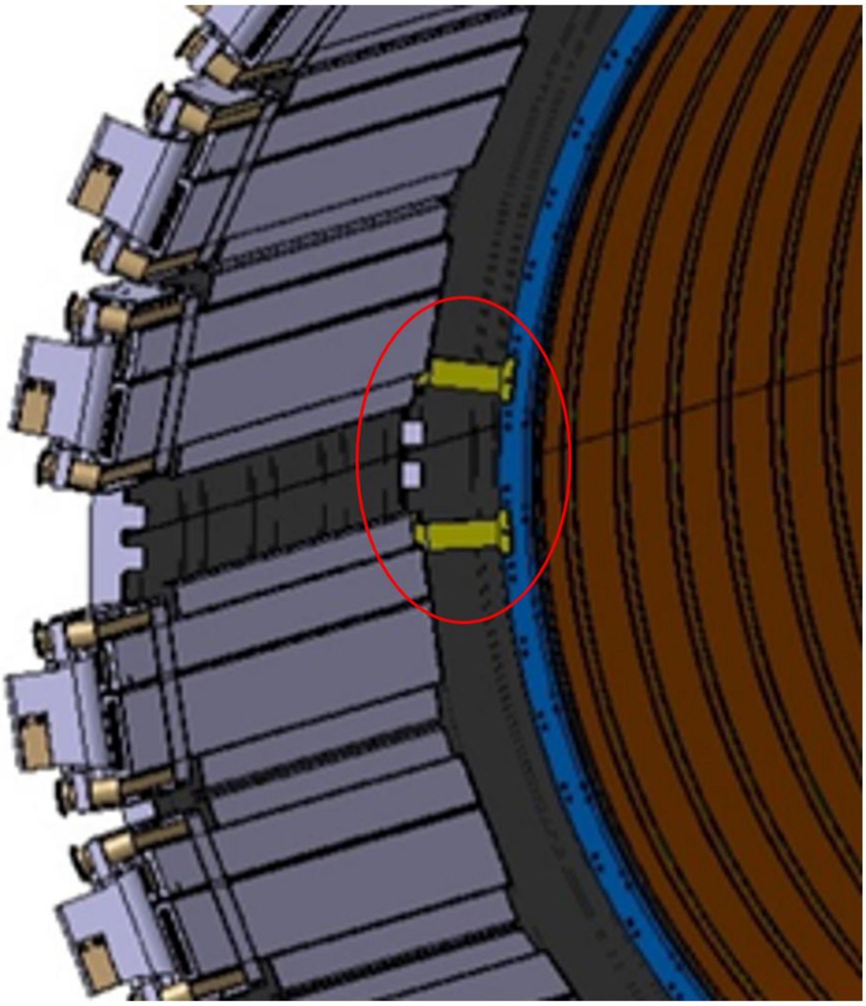

Figure 7 Strip Barrel Supports to Outer Cylinder

The features shown above on the Forward OC shell are from an older figure, they are intended to locate the rail for the Strip Endcap. The rail for the strip endcap will be installed after all Strip

This document is uncontrolled when printed. Check the EDMS to verify that this is the correct version before use

Barrel Service Modules (BSM) are installed as shown above, the Endcap rail will be bonded in place to the OC after Strip Barrel integration is complete. The figure above shows all BSM installed, but this is not the case until all Strip Barrel layers are completely installed (not shown in the figure above.

2.3.5 Internal Structural Interface to the Strip Endcap

The Strip Endcaps will be supported by rails inside the OC, bonded to the inside surface of the OC Forward Shells, between the Strip Barrel Service Modules. Each Strip Endcap has 4 rollers with ~75kgF load, and a required deflection to meet their stability requirements. The rail bonded to the OC will follow OC deflections, but positionally will be bonded after the majority of the loads have been introduced into the OC. The Strip Endcap rails can be introduced in the OC in an 'ideal' location. It is TBD what that location is, i.e. true to ideal beamline, or aligned with the gravity displaced Strip Barrel.

The rails provided for the Strip Endcap inside the OC shell are a single laminate, bonded to the inner surface of the OC Shell, with periodic internal 'shear webs' that stiffen local deflection. The shear webs also include a PEEK insert to allow bolting of the adjustable rail that will be aligned to the global ITk coordinate system after bonding the structural rail. The adjustable rail is a 10mm thick 25mm wide solid laminate with a machined groove that holds either a cylinder or flat rail composed of Stainless Steel. These rails are segmented to allow for differential thermal expansion, with only short segments bonded rigidly near the final resting place of the Strip Endcap rollers. Intermediate segments are allowed to float to compensate thermal expansion.

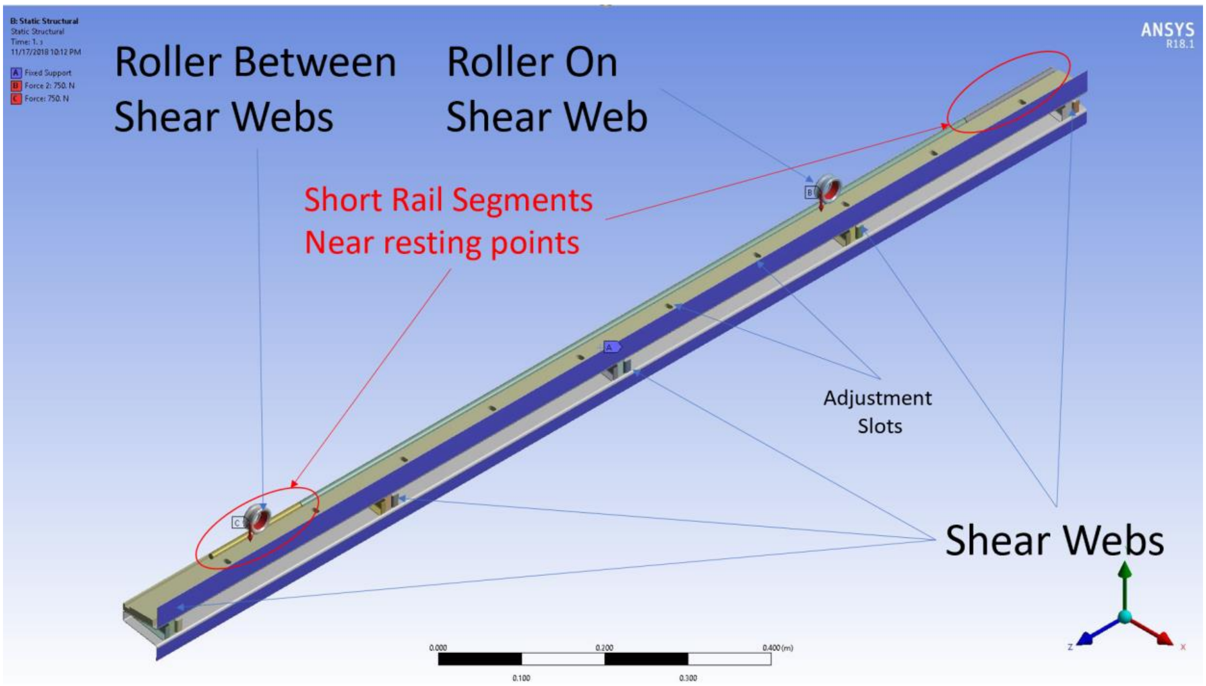

Figure 8 Strip Endcap Rail Analysis Model

Figure 8 above shows the positions considered for analysis, not the final resting position of the Strip Endcap. In the figure, the shear webs are aligned with the 'hat-stiffeners' on the OC Forward Shells. Additional shear webs can be added to better align with both final roller positions, and adjustment slots in the rails. Model above was used to estimate worst- and best-case relative deflection during insertion—shear webs will be placed as required to minimize global deflections of the Strip Endcaps in their installed position, limit displacement/deflection during installation,

This document is uncontrolled when printed. Check the EDMS to verify that this is the correct version before use

and provide sufficient bolt locations for adjusting the Strip Endcap rails. Expected deflections are shown in Figure 9 below.

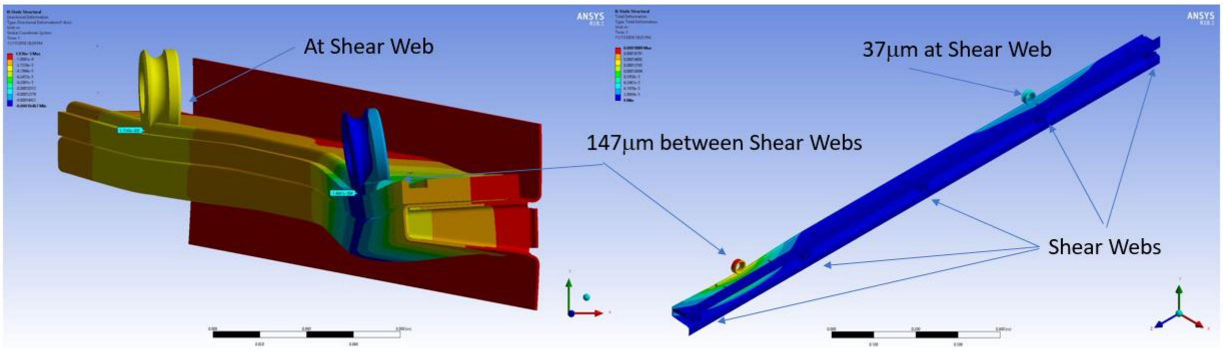

Figure 9 Strip Endcap Rail performance between and on Shear Webs

The adjustable rail is mounted onto the adhesively bonded rail. The rail shown in Detail B of Figure 2 in section 2.3.1 above is the structural component bonded to the OC inner surface. The adjustable rail is shimmed and aligned to a designated position TBD. The adjustable rail will be bonded to the structural rail by injecting adhesive into the gap after final placement.

2.4 Assembly Breakdown Structure and Quality Assurance/Control

Quality assurance is established via testing of prototype structures that then set criteria to test against during production to control quality during production (QC). As most global mechanics are singular structures, QA and QC are nearly indistinguishable as there is not a large production run against which quality is controlled. Methodology to control quality is described in this section.

2.4.1 ABS and Quality Control

Quality Assurance starts with configuration control of documents and traceability. The Assembly sequence and procedures are the backbone of the Quality Assurance program at LBNL where the OC and similar structures will be procured whether from an offsite vendor or fabricated and assembled in-house. The procedures take the form of Work Instructions (WI), which describe the fabrication/assembly process for various components/assemblies with defined verification steps for quality, e.g. measurement of mass, geometry checks, survey etc. The acceptance criteria will be defined during the fabrication and test of prototypes with WI and associated acceptance criteria lists (ACL) at the time of the PRR. The document lists and procedures will follow the ABS (Assembly Breakdown Structure) embedded in EDMS allowing documents such as material certifications, drawings, mass, and WI to be tied uniquely to components and assemblies. A snapshot of the draft ABS for the Barrel OC is shown below.

This document is uncontrolled when printed. Check the EDMS to verify that this is the correct version before use

1						**Barrel Cylinder Instrumented**	
	1					Solder	
	1					Adhesive	
	4					Strain Guage Wire Harness	
	48					Cable Ties	
	48					Cable tie supports	
	12					Heater Wire Harness	
	24					NTC	
	1					**Barrel Cylinder Mechanical Assembly**	
		1				Adhesive	
		2				**Mount Pad Assembly +X**	
			1			Adhesive	
			1			Strain Guage Adhesive	
			4			Strain Guage	
			1			Mount Pad Laminate +X	AU-1000-3504
			1			Lift Point Boss	AU-1000-3534
			1			Roller Stud	AU-1000-3502
		2				**Mount Pad Assembly -X**	
			1			Adhesive	
			1			Strain Guage Adhesive	
			4			Strain Guage	
			1			Mount Pad Laminate -X	AU-1000-3503
			1			Lift Point Boss	AU-1000-3534
			1			Roller Stud	AU-1000-3502
		1				**Barrel Cylinder with Stiffeners**	
			1			Adhesive	
			3			**Hat Stiffener Assembly**	
				4		Hat Stiffener, Normal	
			2			**Hat Stiffener Flat Assembly**	**AU-1000-2381**
				2		Hat Stiffener, Normal	AU-1000-2380
				2		Hat Stiffener, Moun Pad Flavor	AU-1000-2876
			1			**Barrel Cylinder Faraday**	
				1		Adhesive	
				1		Kapton Strips	
				1		Copper Tape	
			1			**Barrel Cylinder with Flanges**	
				1		Adhesive	
				1		Flange, Barrel Side C	AU-1000-3443
				1		Flange, Barrel Side A	AU-1000-3443
				1		**Barrel Shell**	
					20	Heater Pad	
					4	Heater Pad, Side Flavor	
					1	Barrel Shell CFRP Laminate	AU-1000-2322

Figure 10 Assembly Breakdown Structure (ABS) of the Barrel Cylinder of the OC

The ABS is read from the bottom up, with Bold Items, with the quantity required listed to the left, and items in **Bold** being assemblies. CAD model trees will be built to this allowing each assembly to have a unique drawing. Shading indicates a unique WI and associated ACL. Presently, the CAD models are 'flat' with all components appearing at the same assembly level. This will change as assembly procedures, tooling, and make/buy decisions are made in preparation for the PRR.

The AU-XXXX-XXXX numbers shown are record locators in the LBNL Windchill PDM Database. This DB will be used to manage the CAD models, design documents, WI, and all procurement documents to assure traceability and configuration control during production. LBNL gives defined access to this DB to vendors and collaborators to collect quality assurance data during offsite fabrication, and to assure that the latest approved information is available directly. After delivery of components to CERN, a subset of these documents, and As-Built drawings/models will be transferred to CERN EDMS and CATIA (CERN CAD) via this ABS structure.

2.4.2 Quality Control of Composite Materials and Component traceability

The primary consideration in composite materials is that the delivered material meets strength and modulus requirements. LBNL has alternately tested delivered materials with external testing vendors and relied on the vendor supplying the materials to provide mechanical test results as part of material delivery. No difference has been noted in the past 20yrs of direct experience with vendors. With this experience, LBNL requires tensile test of prepreg composites delivered with each batch of material and asks the material vendor to provide these certifications.

An auxiliary requirement is on 'out-life' of pre-impregnated composites (prepreg), which have a limited time allowed at room temperature prior to full cure due to the chemical nature of the resin(s) used to make the composite. Typical 'out-life' is 7 days, with a nominal expiration of 6 months for any given batch. While it has been shown that prepregs perform adequately after 6-month shelf life (stored below 0C), and perhaps after 7 days at room temperature, these are considered off specification, this 'quality threshold' is tracked. LBNL has developed an

This document is uncontrolled when printed. Check the EDMS to verify that this is the correct version before use

hierarchical DB to track out-life of rolls within a given batch, and part 'kits' from a roll of material that inherits 'out-life' properties. This assures that any given composite component will be produced with material that is within out-life specification, and not expired prior to cure. The bar-code labels shown in Figure 6 are from this database. The database allows for traceability of the component materials included in any laminate by batch, which includes material test data, and to assure compliance with out-life and expiration specification. It is also is traceable to the cure cycle in the Autoclave via links to that process DB.

This DB described, and that of the Autoclave are nearing 20yrs of use with several Java modules and older server links not working... LBNL is in the process of acquiring newly written DB in conjunction with ITk production DB vendor that meets the same requirements. Reports will be integrated into Windchill with 'as-built' data for future traceability.

2.4.3 Survey and Alignment

This is an auxiliary consideration and needs discussion within the community for the strategy. The structures will deflect gravitationally as mass is added during assembly. Nominal deflection is 0.5-1mm. Defining how to describe the 'center' of the ITk is an open issue. The ITk is built by adding mass, this can be accounted for via simulation, or just accepted. Provisions for survey of the Strip Barrel are a variety of precision holes in each layer as requested by CERN Survey—there will be a combination of 'Laser Tracker' target holes for external reference, and a number of precision holes for Photogrammetric survey of 'roundness' of each shell. These can be related to targets on the end of the OC, and to the OC Rails during assembly. Later insertion of the Strip Endcaps will deflect the PST, but with full access to the PST bore, a new center can be surveyed. Insertion of the Pixel detector is ~10% of the mass.

A survey plan is anticipated, but not yet defined. Inclusion of strain measurements in either the mount pads, or studs is planned, and correlation with survey results will be done.

2.4.4 Shipment and Handling

The OC will fit into a standard shipping crate for transport by sea. Air transport can save ~10wks on delivery schedule with a moderate cost increase and better environmental control—this is being investigated. Both would have similar handling loads. The OC is designed to support ~10X its mass (at maximal load points) with minimal deflection. As the OC is a deflection limited design and will be shipped without any imposed loads, it can easily handle 10g shock loads that are typical for un-careful handling during transport. Heated and humidity-controlled environments during shipping will be investigated.

An auxiliary flange is foreseen to hold the extremity of the OC round to maintain interface tolerances with the Structural Bulkhead. These flanges are used both during shipment, and while the OC is used during detector integration in SR1. They will assure that the forward flanges are maintain round with sufficient tolerance to install the SB. Auxiliary interface holes on the back side of the OC Forward flanges are provided to prevent interference during ITk integration.

This document is uncontrolled when printed. Check the EDMS to verify that this is the correct version before use

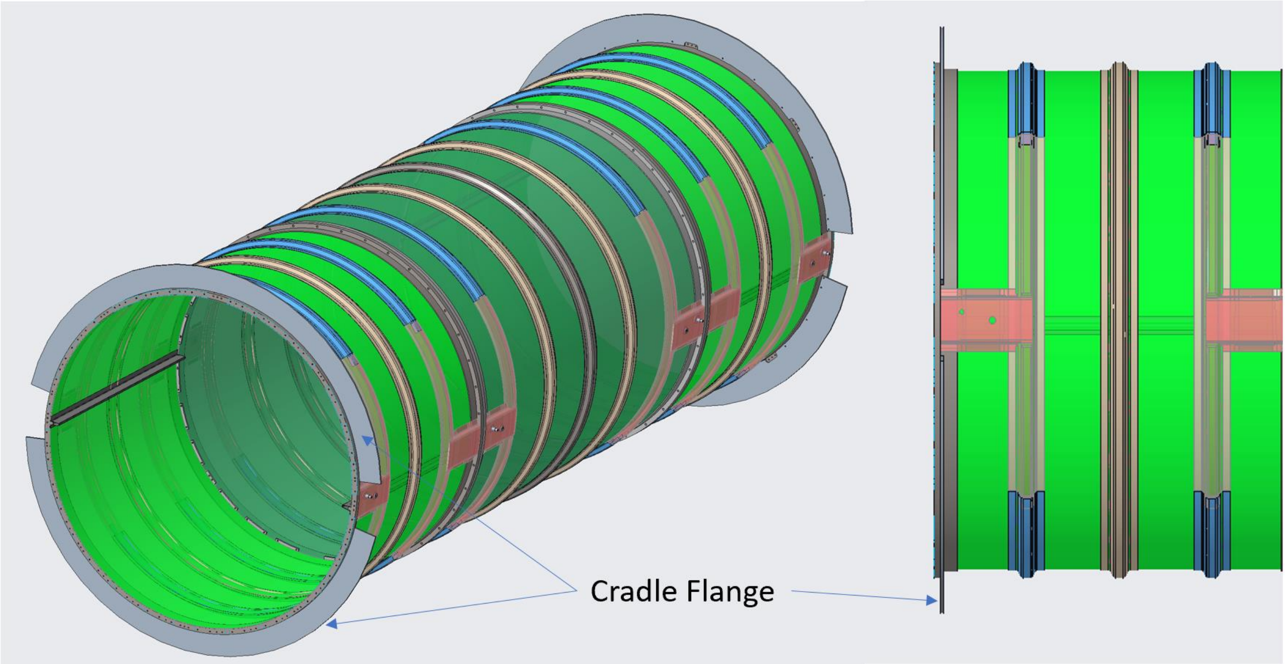

Figure 11 Eccentric Flange Detail

The cradle flange may interact with the cradle used during SR1 assembly. In principle these structures occupy different |Z| space and can be treated separately. ITk service integration may take advantage of this stiffener, but presently not planned. It should be noted that analysis indicates that the fully loaded structure can go out of round at the few hundred-micron level—this flange is required to assure proper mating and sealing of the SB. A dry-fit of the SB is planned with these auxiliary supports in place prior to shipment.

This document is uncontrolled when printed. Check the EDMS to verify that this is the correct version before use

3 OC DESIGN ANALYSIS

3.1 Introduction

The outer cylinder (OC) will be supported inside the Inner Warm Vessel (IWV) by the rails on the horizontal plane. The cylinder will in turn support the inner tracker services, the pixel detector, the strip barrel and endcap detectors. The main parameters driving the OC structure performance were optimized in a stand-alone model. The final design was then tested in an integrated model. The results from the integrated model did not drive changes in the OC structure which was kept the same. The integrated model was however of crucial importance in the evaluation of the performances of the whole system. The integrated model contained the following components of the detector: the outer cylinder, the strip barrel, the structural bulkhead, and the Pixel Support Tube and a simplified representation of the pixel barrel region. Both the strip and Pixel end-caps were not integrated in the FE model: as they are iso-statically connected to the other structures, their structural contribution is well represented by simple localized loads. This section discusses the requirements and the design of the OC. It then shows the optimization of various structural parameters. The integrated model results are presented in the following sections.

3.2 Design requirements

Table 1 Summary of the stability requirements in the azimuthal direction. Stability requirements in the other directions are ten times higher. Table from [3]**.**

	Timescale	Requirement	Comment
Short	1 d	2 um	Always within sub-systems, on a global scale only between seismic events
Medium	1 m	5 um	
Long	Several months to years	as assembly placement accuracy	

The main design requirements are described in [4], and derived from [3]. Requirements on performance are described via time-constants related to the initial survey and later software alignment capability during operation described in [3] with differing levels of performance, as listed in Table 1.

Short, medium, and long term stability have different requirements. Short term stability is the most stringent requirement and will be addressed primarily in this document to demonstrate performance during operation. Load cases are presented later to capture the likely deviations from survey positions at Room Temperature to positions during operation. Variations in loads due to operation contribute to medium term stability and can be controlled by detector operation. Sensitivity to medium term stability can be derived from results presented. The medium timescale applies within sub-system all the time, and on an overall global scale only between seismic events as the global movements are easy to be reconstructed by offline alignment [3].

The most stringent requirement is the stability during operation. The RMS stability has to be lower than 2 μm in the azimuthal direction, and of 100 μm in the radial and longitudinal dimensions. In the early design stages the RMS stability (displacement) Y_{RMS} can be estimated by means of the Miles equation:

$$Y_{RMS} = \sqrt{\frac{Q_n[ASD]}{32\pi^3 f_n^3}}$$

This document is uncontrolled when printed. Check the EDMS to verify that this is the correct version before use

where f_n is the natural frequency of the system, Q_n is the quality factor at the natural frequency f_n, [ASD] is the input Acceleration Spectral Density at f_n. The first natural frequency in the studied direction can be estimated from the gravity sag u_g by comparing the system to a 1D spring-mass oscillator:

$$f_n = \frac{1}{2\pi}\sqrt{\frac{K}{m}} = \frac{1}{2\pi}\sqrt{\frac{g}{u_g}}$$

where g is the acceleration of gravity. Figure 11 shows typical relevant results for our system: the Miles equation results are shown for $10^{-11}g^2/Hz$ and $10^{-10}g^2/Hz$. For example, if the gravity sag is equal to 0.95 mm, the relative natural frequency will be around 16 Hz. If the RMS acceleration at the supports is equal to $10^{-11}g^2/Hz$, the Miles equation provides an RMS stability of about 1 µm.

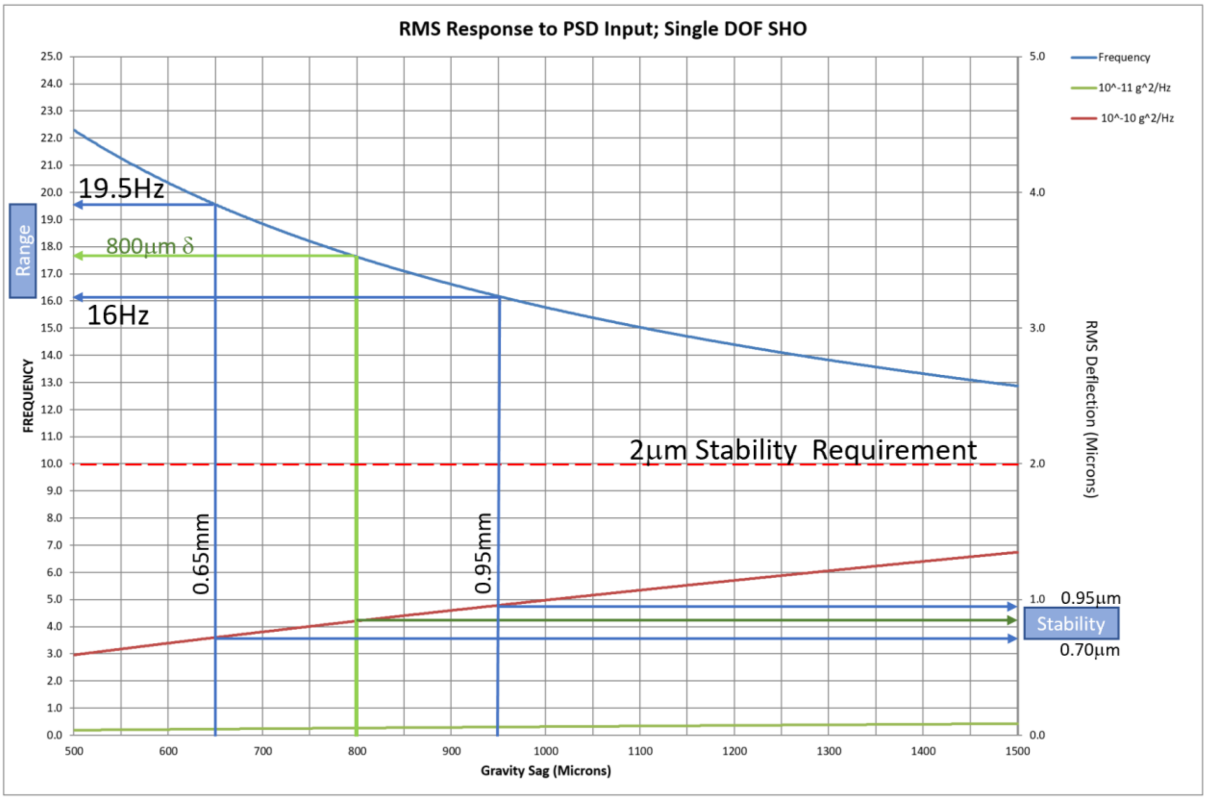

Figure 12 Fundamental Frequency and Expected Stability as Function of Gravity Sag

3.3 Analysis Description

The OC structure is composed of four main structural components (refer to Figure 2): the shell, the hat stiffeners, the flanges and the mounting pads. The mount pads are connected to studs which are supported by rails in the IWV. The loads are given by the polymoderator, barrel services and the weight of the barrel, the endcaps and the pixel detector. The structure will be stiffened by the addition of the structural bulkhead (SB) which will keep the structure circular, in the assembly phase the cradle flange will provide this constraint, and then later by the structural bulkheads that are installed with the Strip Endcaps.

The structure is held by the mount pads, which transmit the gravity load to the IWV, assembly cradle, or to the lifting hooks. The detector loads are introduced inside the structure on titanium flanges at the Barrel/Forward transition. These can be divided in two main categories: service loads and detector loads (pixel and barrel and endcaps detectors). To these it has to be added the weight of the OC polymoderator, which is not negligible. The flanges also hold the various services.

This document is uncontrolled when printed. Check the EDMS to verify that this is the correct version before use

The loads are distributed as shown in Table 2. The values were provided by the sub-system engineers and are not under configuration control presently.

Hereafter we present the analysis performed by means of Finite Element (FE) analysis on the structure. After introducing the model structure and the various assumptions, the main results are presented. A parametric study evaluating the impact of various parameters on the structural stiffness and the total sag is then discussed. Finally, a range of parameters are identified that satisfy the above mentioned requirements and allow a parametric space to investigate 'value engineering' with prospective vendors.

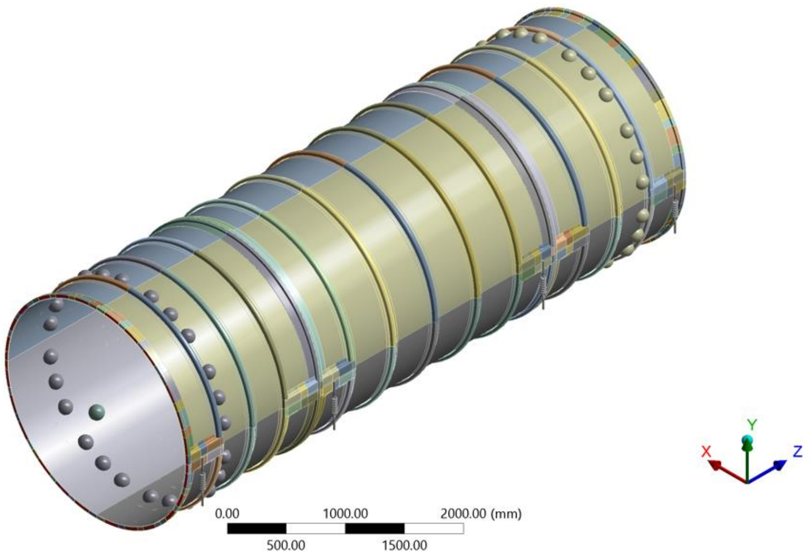

Figure 13 FE Model geometry

Figure 13 shows the overall geometry of the model, as well as the location of the point masses used to introduce the loads inside the structure. A number of details were removed as considered non-relevant for the analysis presented here. For example, the holes in the flanges, the division of the hat stiffeners in four pieces etc. to simplify the meshing for performance.

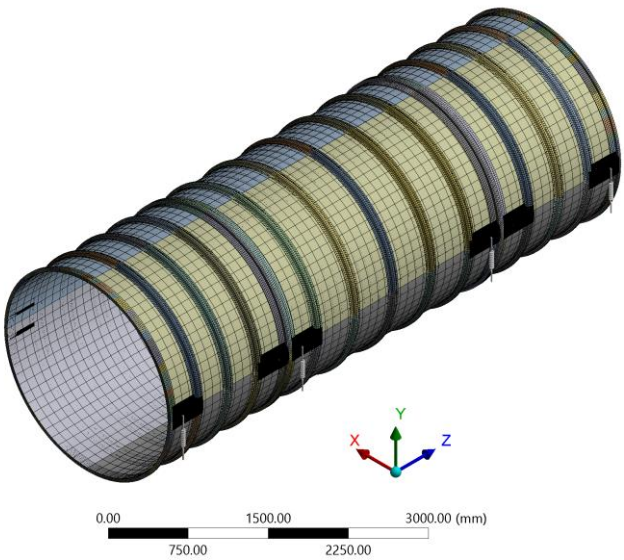

Figure 14 FE Model mesh

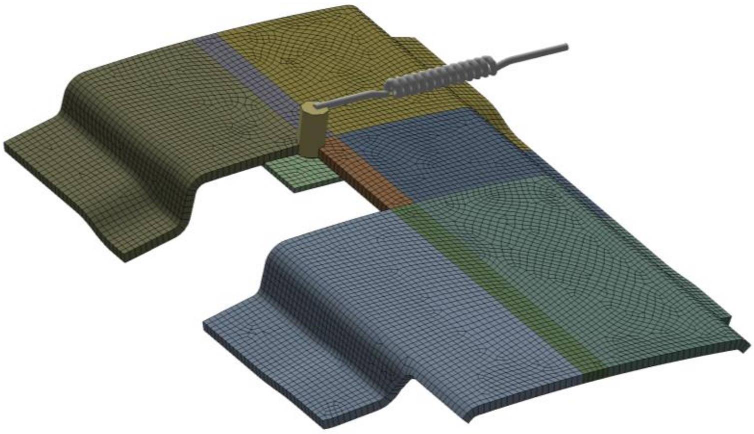

Figure 15 Detail of the mesh on a mount pad

The model mesh is visible in Figure 14: the geometry was partitioned in order to allow in most places a quad or hexagonal mesh. The picture also shows the distribution of the springs, used to introduce the stiffness of the IWV. The IWV represents then an 'elastic bed'; the relative stiffness of the OC and IWV is considered to understand the distribution of reaction loads at the various support points.

3.4 OC FE Model Description

The OC was modelled in ANSYS with a mix of solid, shell and beam elements. In particular, the shell, the mount pads and the hat stiffeners are modelled with SHELL281 elements, the flanges with SOLID186 elements, and the studs with BEAM188. Multi-point constraints (MPC) are used to link some Mass components with eccentric positions to the OC shell elements. SHELL281 employs quadratic elements that can reproduce the behaviour of moderately thick shells.

Connections are introduced using bonded joints, multi-point constraints and springs. The bonded joints are introduced with the surface/surface contact and target elements CONTA174 and TARGE170. These are 8 node surface to surface contact elements. The bonds are considered in this context to be perfect, so that the connected bodies share the same displacements at the interfaces. The interfaces bonded in this way are: the hat stiffeners with the shell, the mounting pads with the shell, the hat stiffeners with the shell, the mounting pad with the hat stiffners and the flanges. The flanges at the barrel/forward interface have no significant shear (behave as bonded).

The connection between the mount pad and the IWV rails is realized by the stud (roller support) which is supported on the IWV side by springs representing the computed stiffness of the IWV and rails system at the various load points. On the other side the stud is connected to a plate via MPC. The plate, modelled with the usual shell elements, (SHELL281) is then bonded to the mount pad. The mount pad plate is linked radially to the beam representing the stud, transmitting both displacement and rotations for latter displacement calculations.

3.4.1 IWV Stiffness Computation

The IWV FE model used for the purpose of dimensioning the bolts required for the IWV Rails, was provided by ATLAS TC and used in turn to determine the vertical stiffness of the vessel at our

This document is uncontrolled when printed. Check the EDMS to verify that this is the correct version before use

defined load points (roller locations on the rails) (see ATLAS Project Document ATU-SYS-EA-0024). The model geometry is shown in Figure 16. The model considered two symmetries: along the length and on the vertical plane and at Z=0. Displacement constraints normal to the symmetry planes were applied and one of the two cross-sections was fixed at the end of the IWV, which is attached to a large radial plate so considered fixed for this analysis. A vertical load, representative of the ITk weight, was then applied on the rail in two different position to simulate the rollers in different longitudinal positions. The stiffness was then simply extracted as ratio between the displacement and the force applied. The following values were obtained: 64 kN/mm and 12.5 kN/mm for the two rollers (respectively CB and C in Figure 2). As expected the stiffness at the roller closer to the flange support, considered infinitely rigid, is higher. These values were used for the springs, modelled with ANSYS element COMBIN14. This element can reproduce the behavior of longitudinal and torsional springs and dampers.

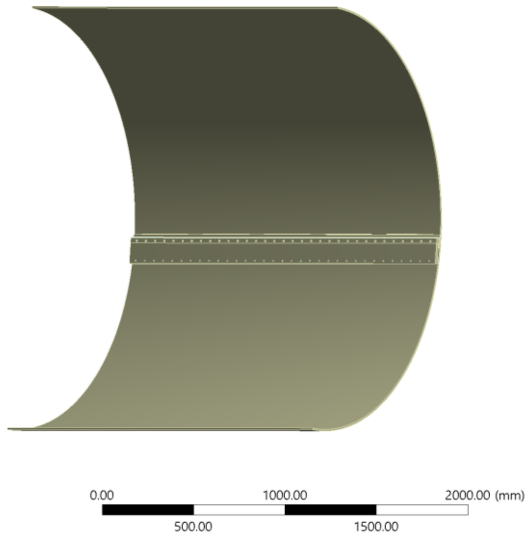

Figure 16 IWV model used to estimate the spring stiffness to be used in the OC model

3.4.2 Strip Endcap Rail Stiffness

The rails that support the Strip Endcap are described in section 2.3.5, with the rollers shown in two arbitrary positions, one in the least stiff configuration, the other aligned with the reinforcing webs. In the installed position, there will be webs located directly underneath the roller, and lock points. The intermediate position was analyzed to determine the expected sag during insertion.

This document is uncontrolled when printed. Check the EDMS to verify that this is the correct version before use

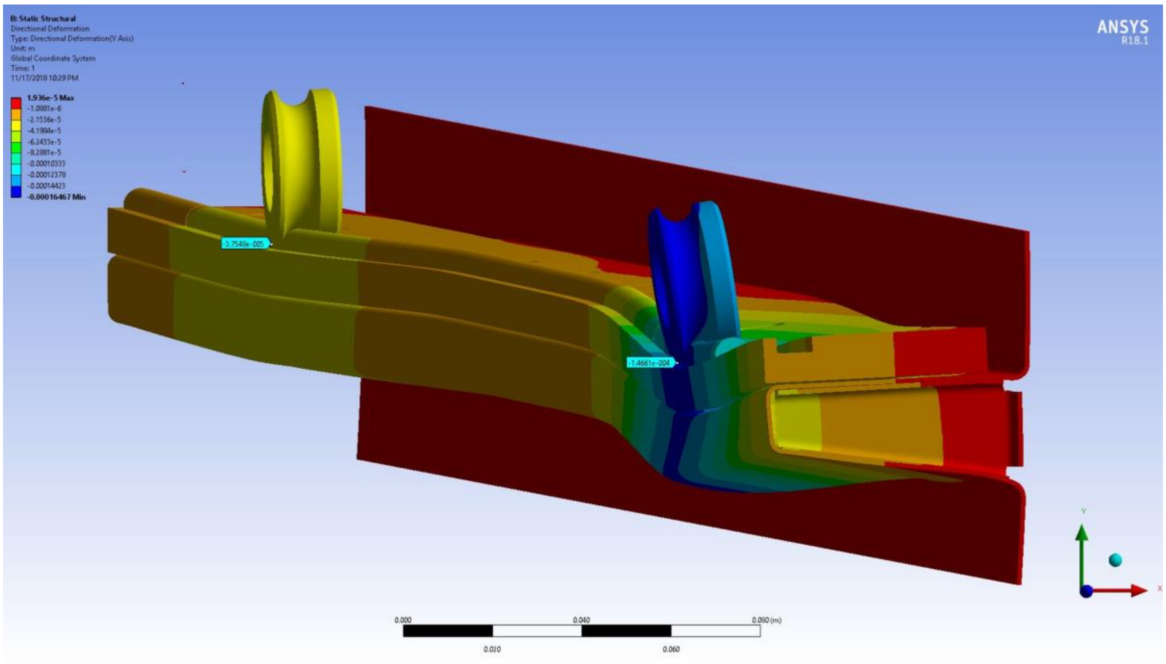

Figure 17 Vertical (Y) Deflection Contour Plot of Strip Endcap Rail

Each Roller has 75 kg load applied. The vertical deflection when aligned with the shear web is 38 µm, and when in between rollers it is 147 µm. The bond area is fixed in this model and assumed to move with the OC shell inner surface. As the expected deflection is so small, this deflection was not considered a useful probe to optimize the OC overall deflection. This rail meets the requirements stipulated in the Strip Endcap ICD.

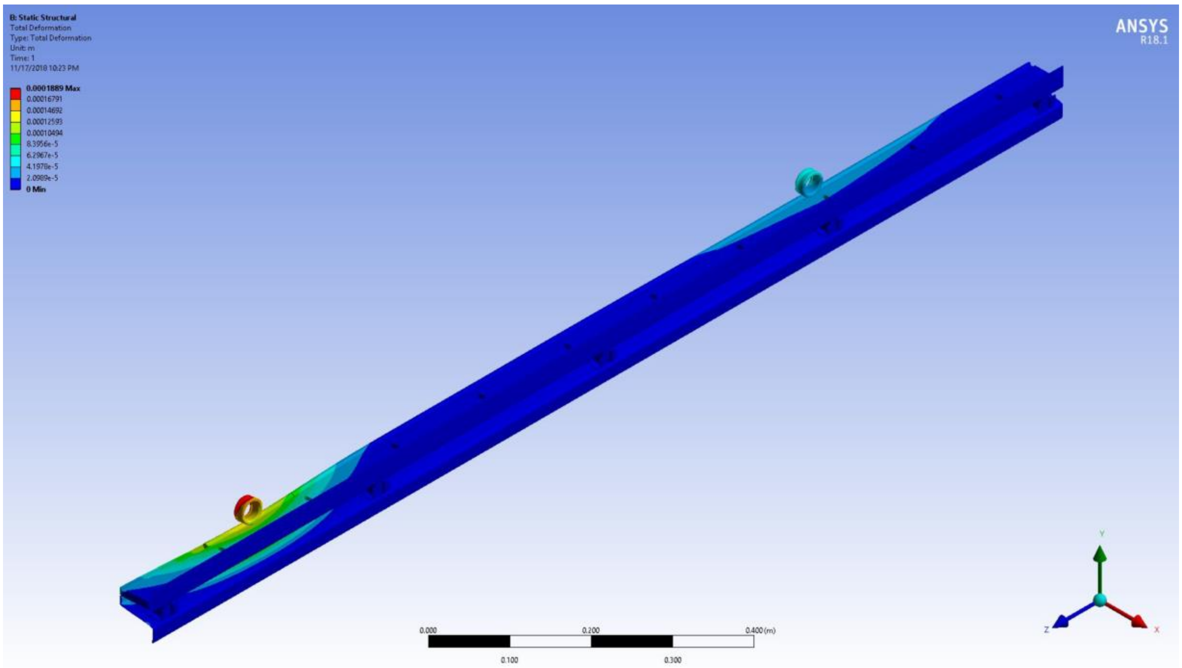

Figure 18 Total Deflection plot showing the web locations inside rail

This document is uncontrolled when printed. Check the EDMS to verify that this is the correct version before use

3.4.3 Materials

The flange, the studs and the stud connection plates will be made out of Titanium. A modulus of 130 GPa was used based on material testing on other programs. The shell, hat stiffeners and the mounting pads will be produced out of carbon fiber. As mentioned in Section 2.3.1, the composite materials have a similar modulus to titanium. The idea behind this approach is that one can initially simplify the modelling process by assuming that the only advantage of such a structure is in the lower weight of the composite material. Obviously further advantages are available with optimized fiber orientation, but only if required—only Quasi Isotropic properties are used for this analysis. More complex material properties will be analysed after requisite test structures are available.

3.4.4 Loads

Table 2 Weights applied to the OC structure (kg)

	Total	**Flange**			
		A	*AM*	*CM*	*C*
Services (each)	15	10.5	4.5	4.5	10.5
Services (total)	720	504	216	216	504
Pixel	400	100	100	100	100
Barrel	652	0	326	326	0
Endcap	600	150	150	150	150
Total	2387				

Table 3 Mass of the Outer Cylinder (kg)

	Weight	**Number**	**Total**
Shell		1	177
Hat Stiffener	3.3	11	36
Flange	46	6	276
Mount Pad	1.35	12	16
Polymoderator		1	318
Total			823

The total non-structural load is equal to 2387 kg representing the current mass estimates of the Strip Barrel, Endcaps, their services, and the Pixel Detector. The weight of the single components and their distribution on the four flanges is tabulated in Table 2. These non-structural weights were introduced in the model as point masses (MASS21 element), connected to the structure via rigid links (MPC184). The linked surface was however allowed to deform under the effect of these links – this allows to connect the structure to the loads without adding unnecessary stiffness to the linked part.

The mass of the OC components is provided in Table 3, and includes the Polymoderator. The total weight of the structure is 823 kg. Neglecting the polymoderator (Polyethylene) this becomes 500 kg. It was considered part of the OC, even if the stiffness added to the structure is negligible. The total weight, considering structural and non-structural components is 3210 kg.

This document is uncontrolled when printed. Check the EDMS to verify that this is the correct version before use

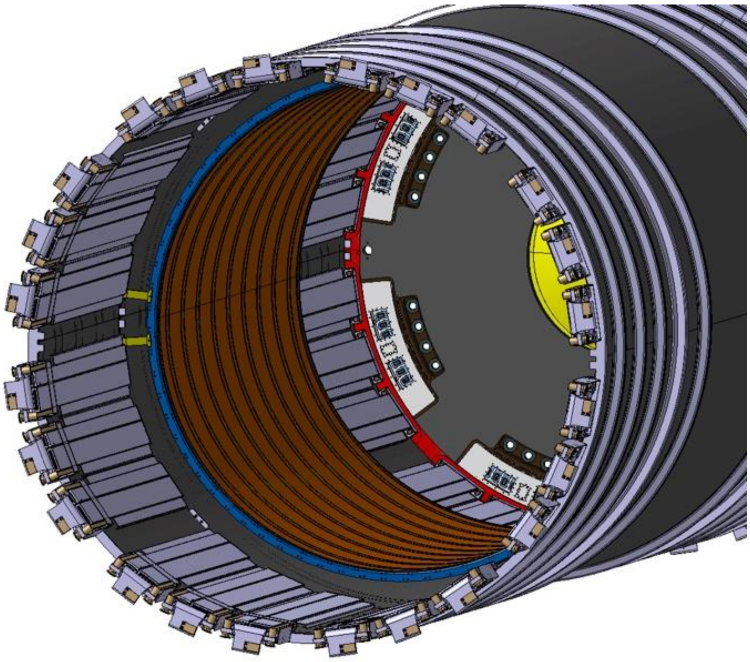

Figure 19 CAD Model showing the connections between the OC and the Strip Barrel and it's services

3.4.5 Boundary Conditions

The OC will be supported by the IWV. The rail shape will be either flat or v-shaped. This will allow to constrain the assembly both horizontally and vertically. The location of these support points is shown in Figure 20: the constraints on the left (negative x-axis) are considered to be 'flat', and providing a simple support in the vertical plane with the spring. Additional constraints were added on the supports on the right (positive x-axis) in order to simulate the Vee-shaped rollers. The location of the horizontal constraint (Vee) was tested inside the model but no particular advantages were detected locating them at the barrel or forward ends of the OC.

The model presented here is symmetric both in the XY mid plane and on the YZ plane. This means that a quarter model could have been simulated. However, for a greater flexibility of analysis in the future the model was realized considering the whole structure and without exploiting these symmetries. The time required to run the model is of the order of 1 minute. The analysis set-up takes a little bit longer, and the whole geometry update, result processing and storage takes about 6 minutes on a standard workstation. Clearly this type of analysis is not largely scalable but performable in parallel across different machines/processors.

This document is uncontrolled when printed. Check the EDMS to verify that this is the correct version before use

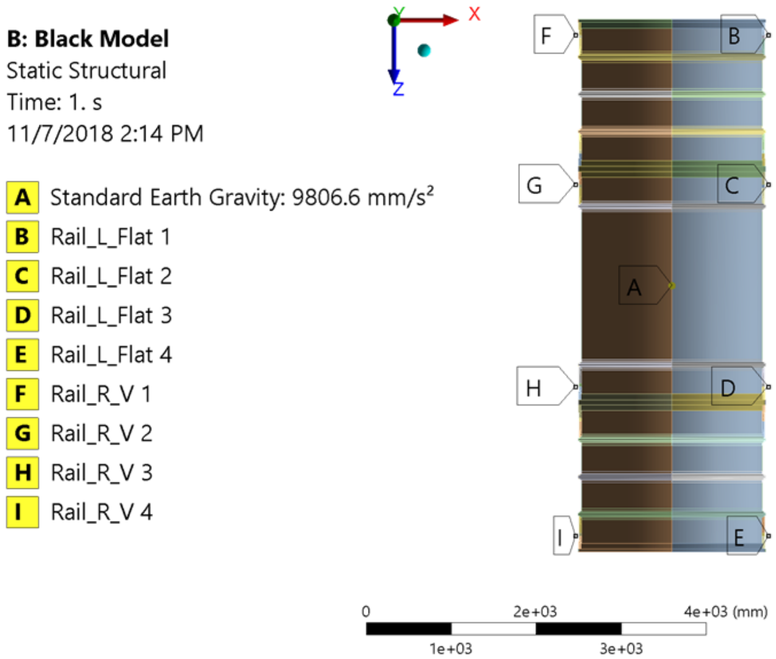

Figure 20 Gravity loads and connection of the OC model with the IWV springs.

3.5 Results

The results presented in this section consider the nominal model parameters, prior to the parametric study analysis. The improvements introduced with the new parameter set will be discussed in Section 3.6. It is worth to notice that the structure performances reported below are still able to satisfy the stiffness requirements provided in Section 0.

3.5.1 Reactions

The loads are quite uniformly distributed across different supports. Larger values are detected for the side supports, due to the higher stiffness of the IWV in this region (closer to its own support). The reaction loads at the spring elements forward/barrel are respectively 4714 N and 3196 N. This corresponds to a vertical deformation of the supports of 73 μm and 255 μm. It should be noted that the reaction loads change based on the relative stiffness of the OC, with stiffer designs shifting more weight to the barrel mounts. The reactions are on the IWV rails, which are a flexible bed. As the forward mount is closer to the chamfer region of the IWV, that rail point is much stiffer—see section 3.6.3 for results of optimized design.

3.5.2 Vertical Sag

A magnified view of the deformed shape of the OC is shown in Figure 21. The contours show the local vertical deflection. The maximum deflection is localized around the mounting pads at the AB and BC flanges. The cross-section deformation is instead shown in Figure 22. From this picture is evident the local rotation of the mount pads, which will in turn increase the displacement at the outer barrel.

The vertical sag at the outer barrel can be divided among three main components: the deformation of the IWV structure and rails, the bolt bending, shear deflection and rotation, and the mounting pad and shell rotation in the load application region. The deflection of the IWV is 255 μm at the strip barrel flange. The stud deflection can be estimated to be 94 μm (see Sec. 3.4). The displacement at the mounting pad is 0.67 mm. This further increases because of the local rotation of the mount pad: the displacement at the barrel holding point on the flange is then equal to 0.79

This document is uncontrolled when printed. Check the EDMS to verify that this is the correct version before use

mm (rotation of the mount pad); and the final deflection at the barrel is equal to 0.81 mm from un-deflected shape.

The vertical deformation of the OC shell is shown as a function of the longitudinal position in Figure 23. The load introduction produces the higher vertical sag on the sides, and a lower one at the top and bottom surfaces of the shell, that are pushed in the upward direction by the moment generated. Because of the model symmetry the left and right results are superimposed.

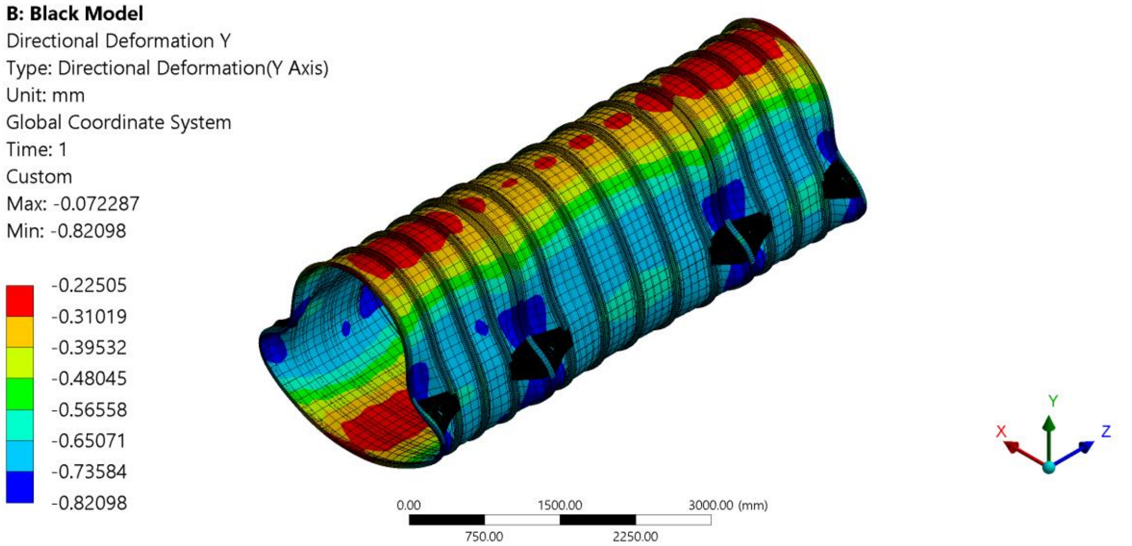

Figure 21 Vertical Deformation Contours (380X)

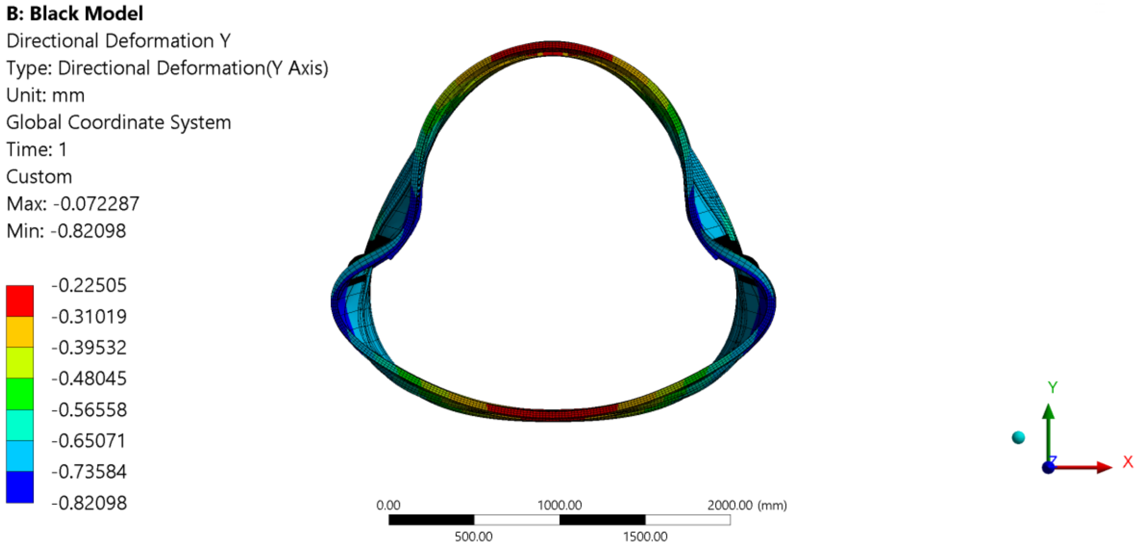

Figure 22 Vertical Deformation End View

The shape is typical of a thin-walled structure where the loads are introduced from the sides.

This document is uncontrolled when printed. Check the EDMS to verify that this is the correct version before use

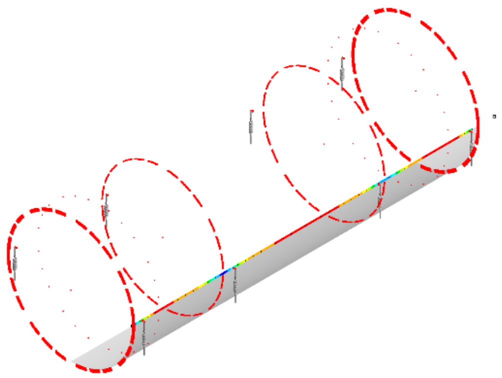

(a)

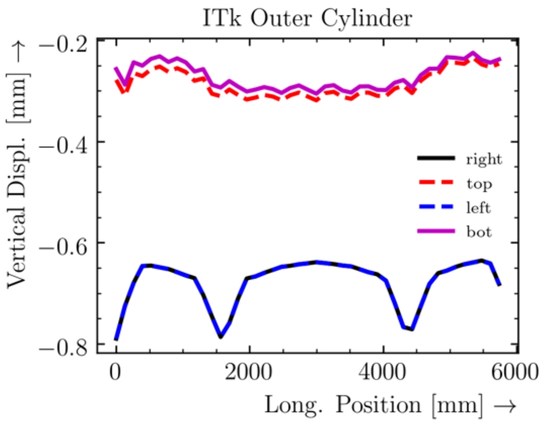

(b)

Figure 23 Vertical deformation along the OC length: (a) path position; (b) vertical deformation

3.5.3 Cross-section deformation

The two cross-sections at the OC extremities will accommodate the structural bulkheads. The deformation of these cross-section could however prevent their installation. It is then interesting to evaluate the deformation of the flanges placed in these cross-sections. The deformed shape is plotted in Figure 24. The horizontal and vertical displacements on a path running clockwise from the negative X axis are provided in Figure 25. The maximum vertical deflection, equal to 0.8 mm, is obtained close to the mounting pads. This is reasonable as this is the region where the higher loads are introduced. On the other hand, the minimum of 0.3 mm is obtained in the vertical plane. The deformed shape was then fitted with a circle, after removing the rigid displacement component of the section, equal to the average motion. The residual error on the radius is shown in Figure 26. The deformed radius was found 14 μm larger than the nominal one. The deformation along the average circle is within ± 1 mm. The average radius was found to be 14 μm more than the underformed one, and the displacement contained within ±1 mm. As expected radial deviation is positive in the bottom half of the OC and negative in the upper one. An improvement of these results can be obtained mounting the cradle flange.

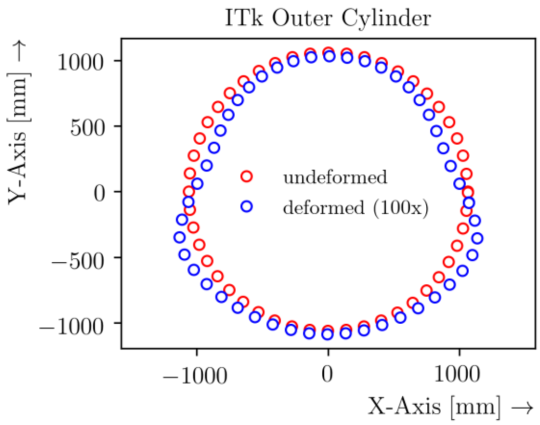

Figure 24 A and C Flanges magnified deformation compared with their original position.

This document is uncontrolled when printed. Check the EDMS to verify that this is the correct version before use

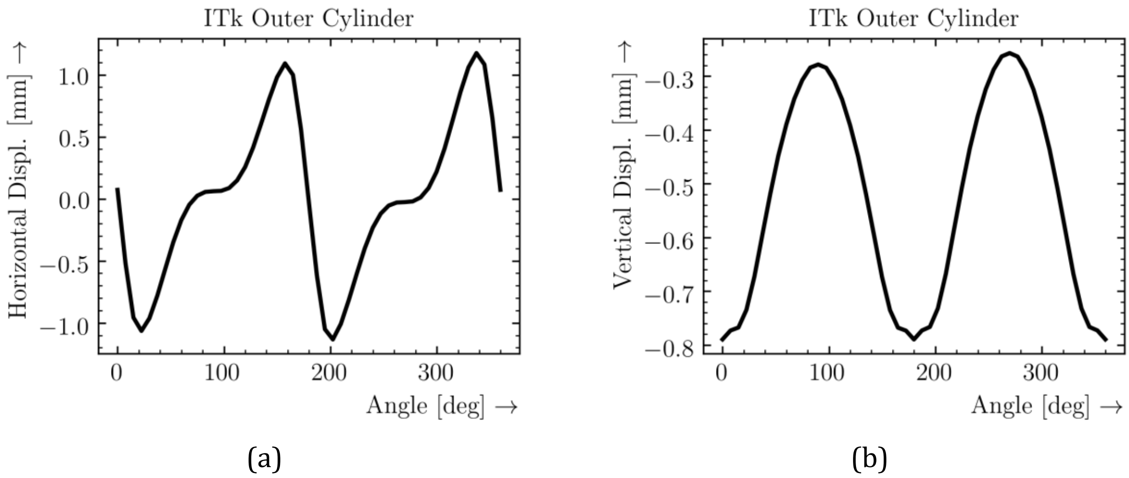

Figure 25 Horizontal (a) and vertical (b) displacements at the A and C flanges.

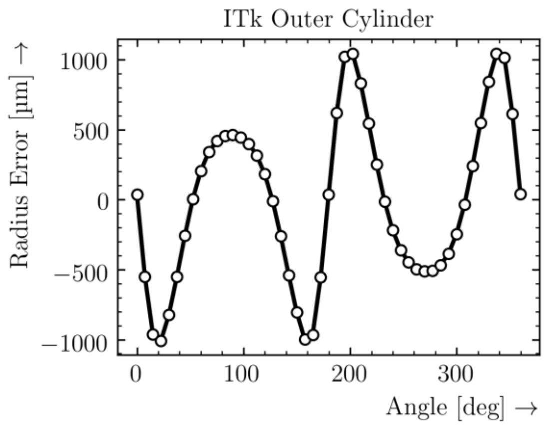

Figure 26 Radial distance between the circle fitted onto the deformed flange and the actual deformed shape.

3.5.4 Stud Deformation

The studs deformation can be estimated considering the sum of the bending and shear actions:

$$\delta_y = \frac{L^3 P}{3EI} + \frac{LP}{AGk}$$

where δ_y is the vertical delta of the stud, L the length, P the vertical load applied, A the cross sectional area, E the elastic modulus, I the moment of inertia and k is the shear coefficient, for a solid circular cross-section equal to:

$$k = \frac{6(1+\nu)}{7+6\nu}$$

where ν is the Poisson's ratio. The deflection for a 27.5 mm long stud, with a radius of 8 mm, is 94 µm. The deflection due to shear is equal to 20 µm. Increasing the radius to 12 mm reduces the deflection to 23 µm, of which 9 µm due to shear. As expected, the relative contribution of shear is

This document is uncontrolled when printed. Check the EDMS to verify that this is the correct version before use

more significant when the ratio between the length and radius decreases and the stud becomes thicker.

3.6 Parametric Analysis of the OC behavior

3.6.1 Parameters and Response Description

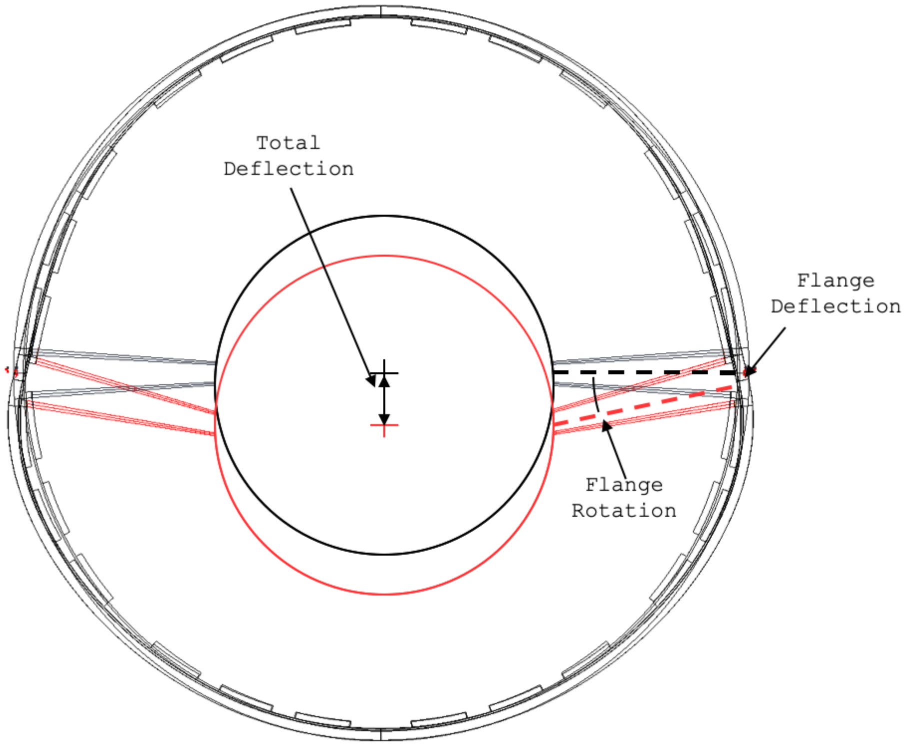

Figure 27 Main output parameter: vertical displacement of the Strip Barrel

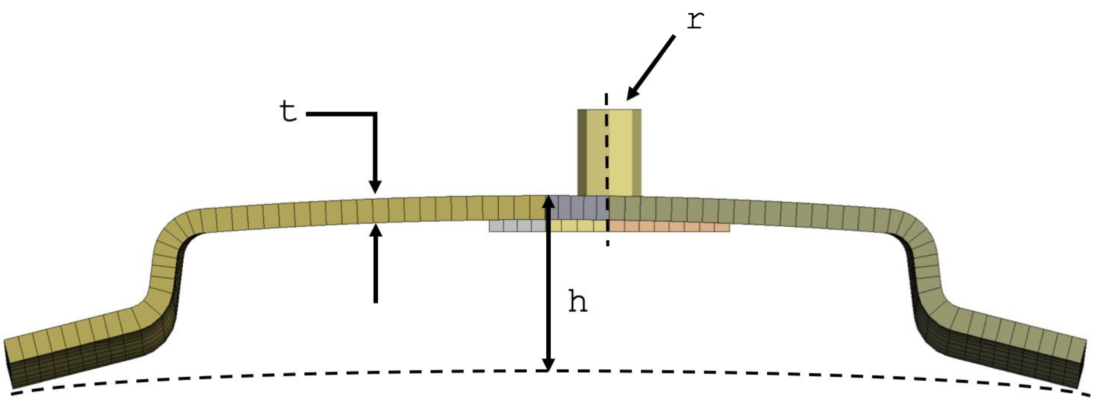

Figure 28 Description of the parameters: t is the mount pad thickness, h the mount pad height, r the stud radius

The ANSYS model was parameterized by means of Python scripts. The parametric analysis was performed in order to explore the design space and understand the response of the structure at the main structural changes that are allowed at this stage. The response selected was the vertical deflection at the barrel supports (see Figure 27). In particular, the deflection was considered as a

This document is uncontrolled when printed. Check the EDMS to verify that this is the correct version before use

sum of the vertical displacement of the supporting surface and its own rotation which further increases the sag. The contribution due to the rotation at the barrel was added to the vertical deflection at the OC flange connections. The outer barrel and in general the detector was considered as a soft component in this regard This means that its motion is assumed to follow the deformation of the outer cylinder, without adding any stiffness to the OC. The sag increase due to the outer barrel deformation was instead already discussed in Section 0.

As described in Section 3.5.2, the sag contributions are distributed on the path that goes from the IWV rail to the barrel supports. Therefore, the main parameters that will influence this deformation will be stiffness of the mount pad and of the bolts, as well as the local stiffness of the OC. The analysis considered the following parameters (see Figure 28): the mount pad thickness, the mount pad height increase and the stud radius. For reference, the parameters used to obtain the results presented in Section 3.5 were: 6 mm for the thickness, 0 mm for the height increase, 8 mm for the stud radius.

The parametric space was explored with a factorial analysis. The boundaries for this space were chosen to be 5 mm and 8 mm for the thickness, 0 mm and 10 mm for the height increase, and 6 mm and 12 mm for the stud radius. The only real constraint to these values is the maximum height of the mount pad, that is obviously constrained by the envelope of the IWV. The stud radius and mount pad thickness boundaries are instead tentative ones and could be further increased in the future, if the performance would require it.

For this analysis all the components were assigned isotropic properties to simplify optimization studies. The flange, the studs and the stud connection plates will be made out of Titanium. A modulus of 130 GPa was used based on material testing on other programs. The shell, hat stiffeners and the mounting pads will be produced out of carbon fiber. As mentioned in Section 2.3.1, the composite materials have a similar modulus to titanium. The idea behind this approach is that one can initially simplify the modelling process by assuming that the only advantage of such a structure is in the lower weight of the composite material. Obviously further advantages are available with optimized fiber orientation, but only if required—only Quasi Isotropic properties are used for this analysis. More complex material properties will be analysed after requisite test structures are available.

3.6.2 Results

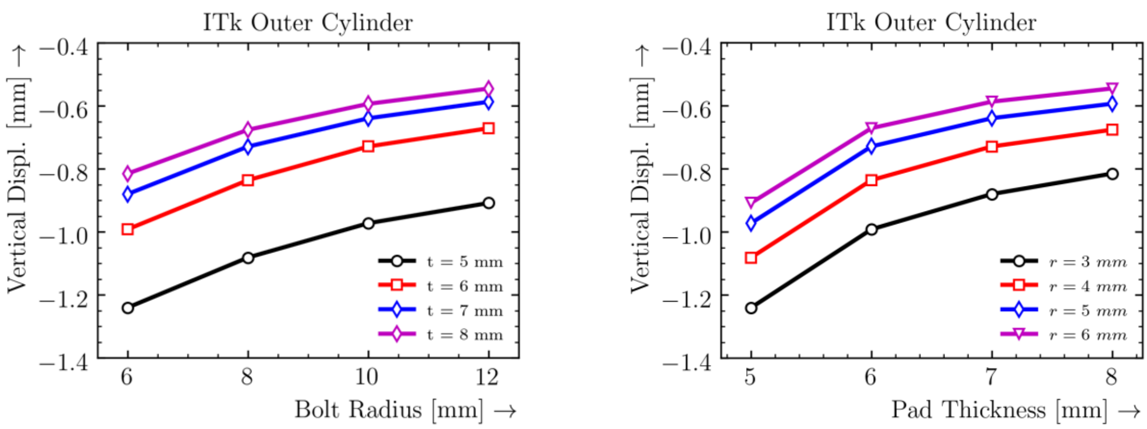

Figure 29 Vertical Displacement as functions of (t) and (r), for a null height increase

This document is uncontrolled when printed. Check the EDMS to verify that this is the correct version before use

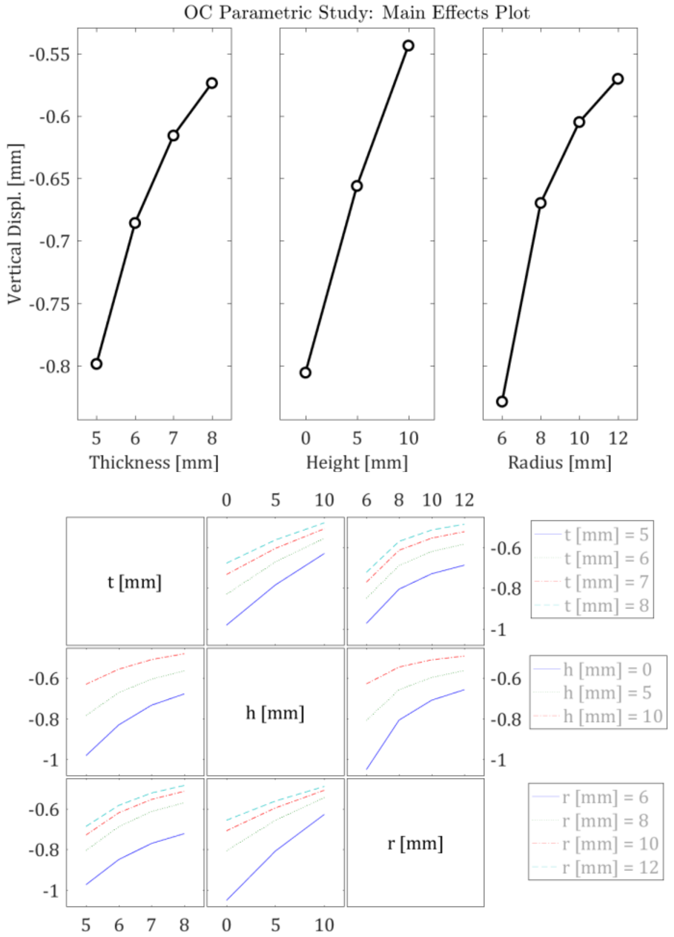

Figure 30 OC Parametric study: main effects and interaction plots

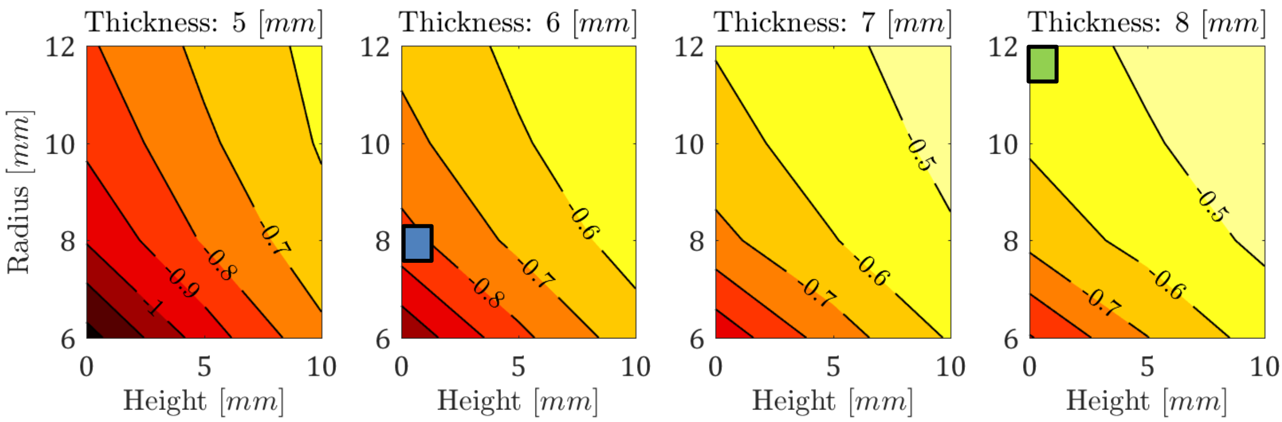

Figure 31 Vertical deflection at the strip barrel as function of the 3 variables

Example results as a function of the bolt radius and the mount pad thickness are provided in Figure 29. The main effect and interaction plots are instead provided in Figure 30: these plots are obtained averaging out one or both parameters and then plotting the output variable as a function of the remaining ones. It is interesting to notice that the increase of the bolt radius from 8 mm to 12 mm would reduce the vertical displacement of about 100 µm. The analytical computation of Section 3.5.4 predicts instead an increase of 70 µm. The increased contribution is mainly due to the amplification introduced by the local rotation. The most sensitive parameter seems to be the

This document is uncontrolled when printed. Check the EDMS to verify that this is the correct version before use

mount pad height. It is also the only one that does not saturate on the higher end of the explored design space. The interaction plot shows that the parameters are roughly independent – the variation of two parameters generally generate only an offset in the response surface function of the other parameter. However, there is a saturation effect: for example, varying the radius of the bolts when the height increase is equal to 10 mm will provide no real advantage on the response. This is expected, as the

The contours in Figure 31 show the total sag at the barrel connection as a function of the mount pad height increase, the stud radius and the mount pad thickness. As the mount pad is stiffened, the contribution of height decreases (less 'rotation' of the stud at its base). The vertical sag of the barrel varies between 1.2 mm to almost 0.4 mm in the design space considered. The stability requirements provided in Figure 12 are satisfied for multiple points in these contour points. In general, to achieve a vertical sag lower than 0.6 mm, it is possible to maximize two parameters out of three or to choose an average increase of all of them. The design described in Section 3.5 is indicated by the blue box in Figure 31, and a possible improved design, covered in the next section, by the green box.

3.6.3 Improved Design

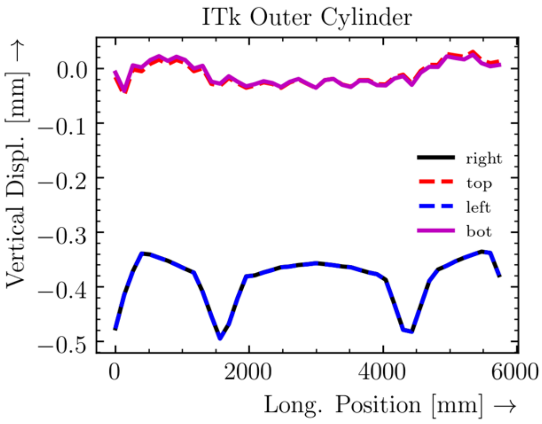

Figure 32 Vertical deformation along the OC length

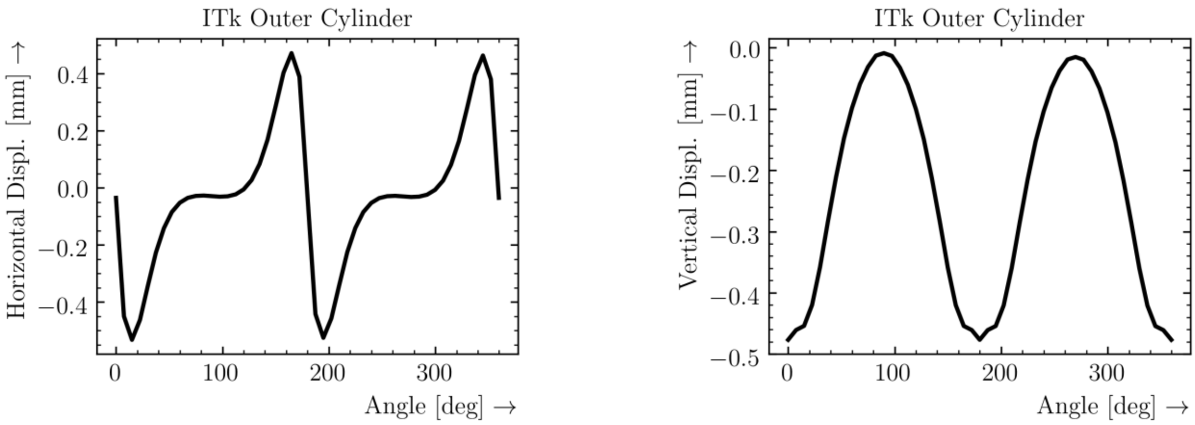

Figure 33 Horizontal and Vertical displacements with the updated parameters

This document is uncontrolled when printed. Check the EDMS to verify that this is the correct version before use

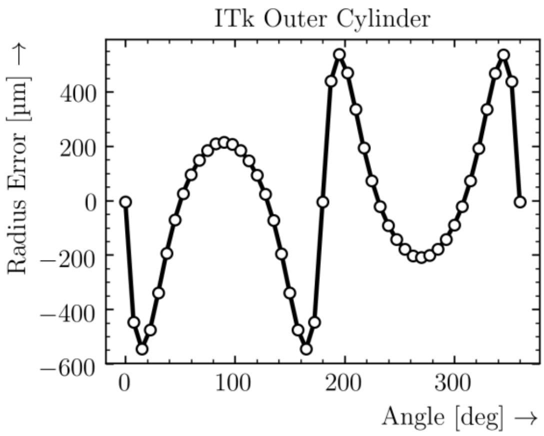

Figure 34 Radial deformation of the OC at the A/C flanges

The design was updated using the results from the parametric analysis of Section 33. The following parameter values were selected: 8 mm mount pad thickness, 0 mm height increase, 12 mm bolt radius. The sag at the strip barrel with these assumptions is equal to 0.55 mm, which would provide a total stiffness at the higher end of expected stability requirement of Section **Error! Reference source not found.**.

The increased stiffness of the OC redistributes the reaction between the supports. The reaction load at the forward support is now equal to 5234 N, while the central one sees 2684 N. This result is expected as the higher stiffness reduces the compliance that the structure can provide to follow the deformation of the IWV. The deformations of the springs for this deformation are respectively equal to 81 μm and 215 μm.

The vertical deflection of the OC shell along the longitudinal axis is provided in Figure 32. The vertical displacement is now contained with values always lower of 0.5 mm. Figure 33 and Figure 34 show the deflection at the A and C flanges. The horizontal and vertical displacements are provided, along with the residuals obtained fitting a circumference to the A and C flanges. The residuals are now significantly lower than the ones provided before and contained within ±0.5 mm. The radius variation was lower than 1 μm.

This document is uncontrolled when printed. Check the EDMS to verify that this is the correct version before use

4 STRIP BARREL MODEL

4.1 Description

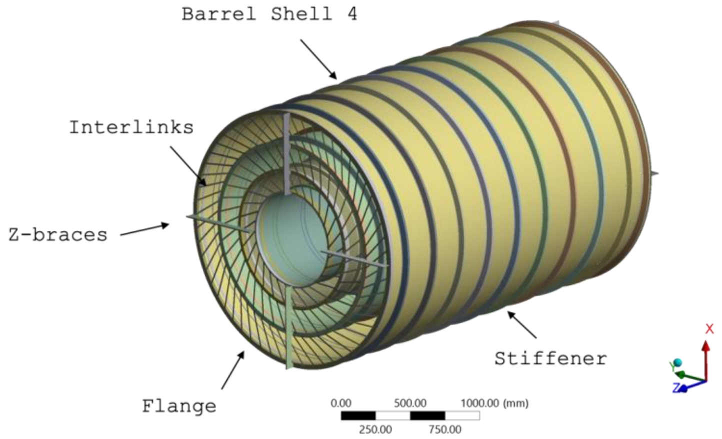

Figure 35 Strip barrel geometry and part names.

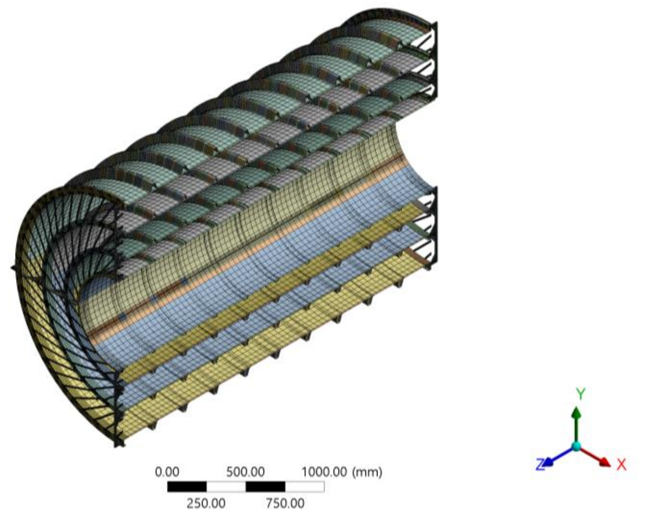

Figure 36 Strip barrel FE model mesh.

The strip barrel structure, shown in Figure 35, is composed of 4 layers, each one with a shell, nine hat stiffeners, and two flanges at the extremities. The inner layer (L0) has two additional flanges at the extremities to connect the PST barrel to the PST forwards. Finally, the PST barrel hosts the rails supporting the Pixel barrel and End-cap. For further details on the design please refer to [5].

4.1.1 Connections

The flanges and the hat stiffeners were *glued* by means of bonded contacts to the shells. The flanges are designed to be built in two pieces [5]. The two components of the flanges were similarly connected by bonded contacts. The Pixel rails were bonded to the PST. The Pixel barrel was simulated by means of beam elements with representative stiffness, connected to the PST with MPC elements. The pixel end-cap is introduced as a distributed mass on the rails.

This document is uncontrolled when printed. Check the EDMS to verify that this is the correct version before use

4.1.2 Material properties

The components were all created by means of layered shell elements whose stiffness was computed by means of the ACP code. The material properties for the laminates were obtained from both literature and past measurements performed at LBNL. Table 4 reports the fiber modulus, strength and elongation, and the values used for the single ply laminate, assumed quasi-isotropic. Finally, the table contains the maximum strain allowed in the various directions, used in the next section to verify the structure.

Table 4 Material properties used for the Carbon Fiber laminates in the integrated model

ATLAS ITk Carbon Fiber Properties																	
	Fiber Properties				Laminate Properties												
Material	Modulus	Strength	Elongation	Density	Ex	Ey	Ez	Exy	Eyz	Exz	Ax	Ay	Az	Axy	Ayz	Axz	Density
/	GPa	MPa	%	g/cm3	GPa	GPa	GPa	GPa	GPa	GPa	%	%	%	%	%	%	g/cm3
M55J	540	4020	0.8	1.91	255	4.49	4.49	2.46	1.77	2.46	0.8	6.68	6.68	82.93	16.95	12.20	1.52
CN-60	620	3430	0.6	2.12	94.5	94.5	6.5	41.5	4	4	0.6	0.6	4.62	1.37	14.18	7.50	1.74
CN-80	780	3430	0.5	2.17	118.9	118.9	6.5	52.2	4	4	0.5	0.5	4.62	1.14	14.86	7.50	1.74
K13C2U	896	3792	0.42	2.2	463	5.6	5.6	9.23	9.23	9.23	0.42	5.36	5.36	21.07	3.25	3.25	1.54

This document is uncontrolled when printed. Check the EDMS to verify that this is the correct version before use

4.1.3 Loads

The stave weight was applied by linking portions of the hat stiffeners and flanges surfaces to a point mass. The location of the point mass is computed on the basis of a simplified beam model. The idea is to reproduce the amount of force and moment that would be applied on the supporting structure by the stave weight. The stave system can be simplified for our scopes in a beam fixed on the two extremities, with a distributed load applied over the length, as shown in Figure 37. In this case, indicating with q the distributed load, with L the stave length, the force and moment applied on the two supports A and B will be equal to:

$$R_A = R_B = \frac{qL}{2}$$
$$M_A = M_B = \frac{qL^2}{12}$$

As a consequence, by creating two point masses at $L/6$ and $5L/6$ and linking them to the staves is possible to reproduce the correct reaction loads on the support structure.

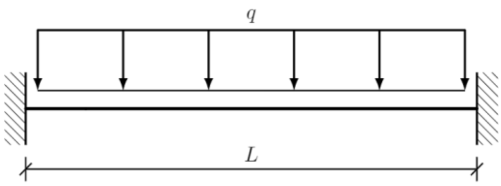

Figure 37 Simplified representation used to position the point-masses modelling the staves

4.2 Interlink/Flanges Experimental Test and Model Calibration

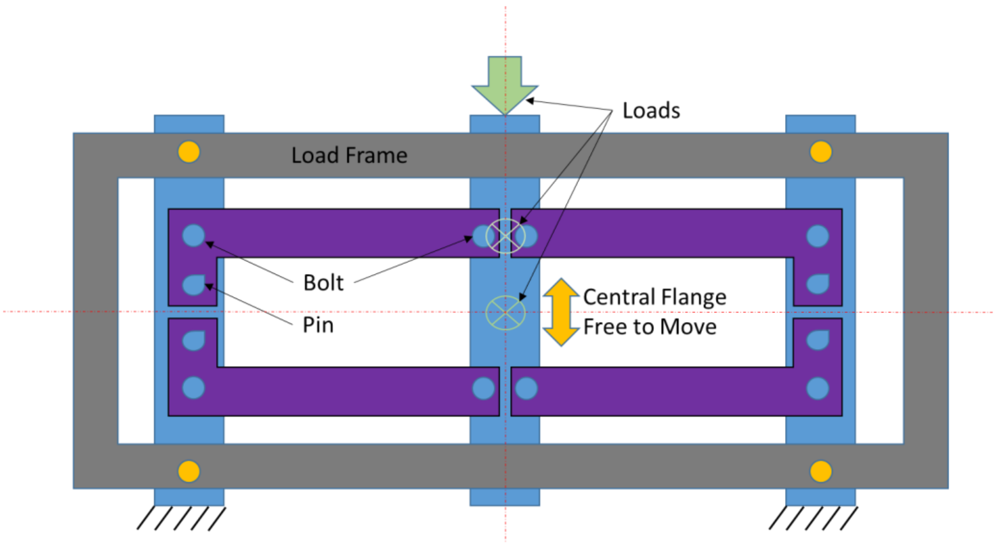

Figure 38 Schematization of the experimental set-up used to test the actual stiffness of the flange-interlink system as designed for the strip barrel structure.

The interlink connecting the various layers were tested in a simplified setup shown in Figure 38. The set-up is made of the following components: a load frame, connected with shoulder bolts to

This document is uncontrolled when printed. Check the EDMS to verify that this is the correct version before use

three flanges, and four interlinks connected with bolt and pins to the flanges. Three test configurations were used: load normal to the interlinks plane, load in the interlinks plane, parallel to the flanges, and normal to the flanges. The loads are applied by means of lead weights, positioned on the flange or connected by means of a string (see Figure 39). The interlinks and flanges were built in Aluminium, giving a reference point for performances and FE validation, and then in the CFRP planned for production (CN-80). The material properties used are provided in section x of this chapter. The test was performed varying the following parameters: load direction, torque applied on the interlink bolts, and flange-interlink material. The applied torque can be defined as a function of the bolt radius, yield stress, and friction between the connected components:

$$T_i \cong K_i F_i d$$

$$K_i \cong \left[0.50\mu + \frac{\tan\lambda\cos\alpha}{\cos\alpha - \mu\tan\alpha} + 0.625\mu_c\right]$$

Where μ_c is the friction coefficient between the head or nut, μ is the thread friction coefficient, d is the bolt diameter, K_i the torque coefficient, λ the lead angle, F_i the preload force and T_i the tightening torque.

The torque was defined considering an applied stress equal to 80% of the yield stress of the bolts for the Aluminum flanges. However, this condition may be critical for the CFRP flanges, which may be crushed under such pressure. The actual maximum torque applicable is a function of the friction coefficient and the washer's thickness and size. In fact, it would be possible in principle to gradually increase the area through which the stresses flow inside the flanges and the interlinks. There are however limits to the washer size (the interlink head diameter). A gradual increase of the torque was applied on the bolts, studying the variation of the experimental results as a function of this value. It is important also to remark that it is actually difficult to estimate the actual pressure applied locally on the CFRP components for a specific torque. In fact, the friction coefficient is unknown for the CFRP configuration. The torque was measured, but unfortunately it was not possible to correlate it with the longitudinal force applied to the bolts. In particular, the longitudinal deformation of the bolts was measured, but their length was too small to produce a significant elongation and the obtained values were unreasonably dispersed.

A FE model was developed to study and support the experiment. The model results are shown in Figure 41. The modelling approach is fully consistent with the one that was then used in the Strip Barrel FE model. The pins joints are introduced considering a cylindrical joint. The bolts joints are introduced with a sum of a cylindrical joint and a longitudinal link with defined stiffness. The stiffness can be set very high to simulate a 'perfect joint' condition, where no motion is allowed by the bolt (friction and normal stiffness are blocking completely the relative motion of the two parts).

The test results for the out of plane load case are shown in Figure 40, left. The measured displacement was equal to 1.57 mm for the Aluminum parts, and 1.55 mm for the CFRP ones. The experiment showed a very small variation of the response as a function of the applied torque. It is also interesting to compare the measurements with the expected motion computed on a FE model: the results are very similar (within 6%) to what was computed considering perfect joints (no rotation or normal separation allowed at the bolts).

The test results for the in-plane load case are shown in Figure 40, right. The motion shows a clear hysteresis cycle, and a permanent displacement produced by the first loading cycle. The applied torque substantially changed the outcome of the experiment, decreasing the permanent displacement and increasing the overall stiffness. The total displacement reported in the Table was extracted from the data neglecting the first load cycle. This is in fact corresponds more to an assembly variable, and does not impact the stability. In particular, with the Aluminum parts the

This document is uncontrolled when printed. Check the EDMS to verify that this is the correct version before use

lower torque produced a displacement of 0.85 mm. This is far from what was expected by the FE model results (0.55 mm). Increasing the torque to 32 in lbs reduced the displacement to 0.575 mm. This is within 5% of the value predicted by the FE model with perfect joints. A similar effect was measured on the CFRP parts: the displacement with a torque of 16 in lbs was equal to 1.05 mm. Increasing to 32 in lbs reduced the displacement to 0.775 mm. This is still far from the predictions of the FE model. As this model was able to predict the Aluminum performances and also the CFRP behavior for the out-of-plane load, it is reasonable to imagine that the discrepancy is only due to the fact that the bolts are allowing some relative motion of the interlinks with respect to the flanges. A modelling strategy able to reproduce this kind of behavior is explored in the following sections.

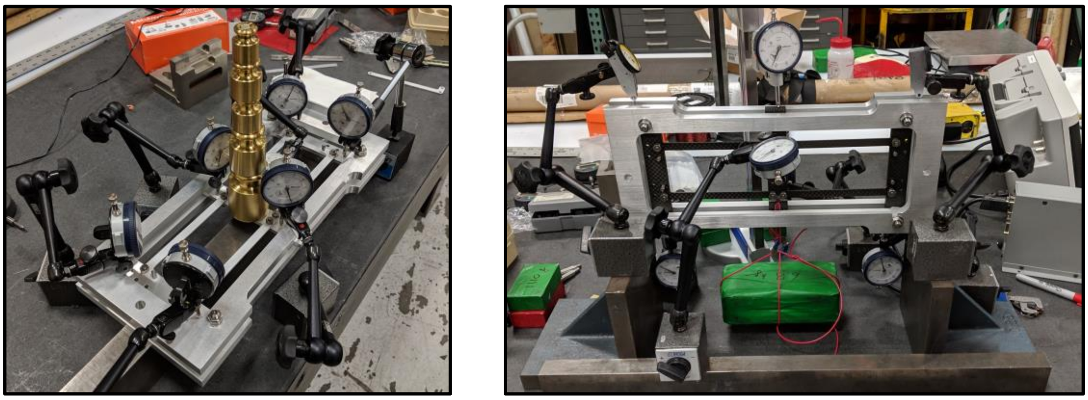

Figure 39 Photo of the experimental set-up used to test the stiffeness of the flange-links system under a normal load (Left) and in-plane load (Right).

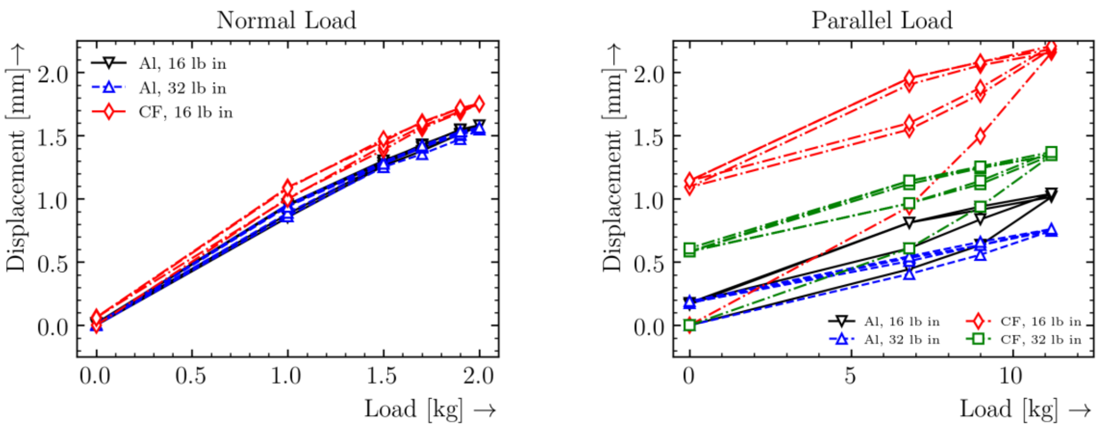

Figure 40 Displacement as a function of the applied load for the normal load condition (left) and parallell load case (right). The results are shown for the Al. and CFRP flanges/interlinks, considering different torque values (16 lb in and 32 lb in) for both. The normal solution is not influenced by the amount of torque, while the parallel load is significantly dependant.

This document is uncontrolled when printed. Check the EDMS to verify that this is the correct version before use

Table 5 Results from the interlink experiment and FE model comparison, normal load

Material	Torque	Weight	Force	Max Delta Meas.	Max Delta FE	Error
	in lbs	kg	N	mm	mm	%
Al	16	2	19.6	1.571	1.48	6%
Al	32	2	19.6	1.558	1.48	5%
CFRP	16	2	19.6	1.552	1.55	0%

Table 6 Results from the interlink experiment and FE model comparison, in-plane load

Material	Torque	Weight	Force	Max Delta Meas.	Max Delta FE	Error
	in lbs	kg	N	mm	mm	%
Al	16	11.2	109.9	-0.85	-0.55	55%
Al	32	11.2	109.9	-0.575	-0.55	5%
CFRP	16	11.2	109.9	-1.05	-0.47	123%
CFRP	32	11.2	109.9	-0.775	-0.47	65%

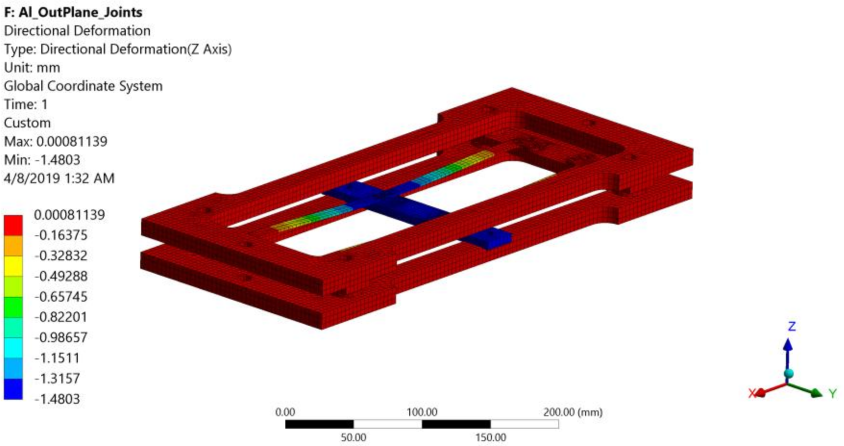

This document is uncontrolled when printed. Check the EDMS to verify that this is the correct version before use

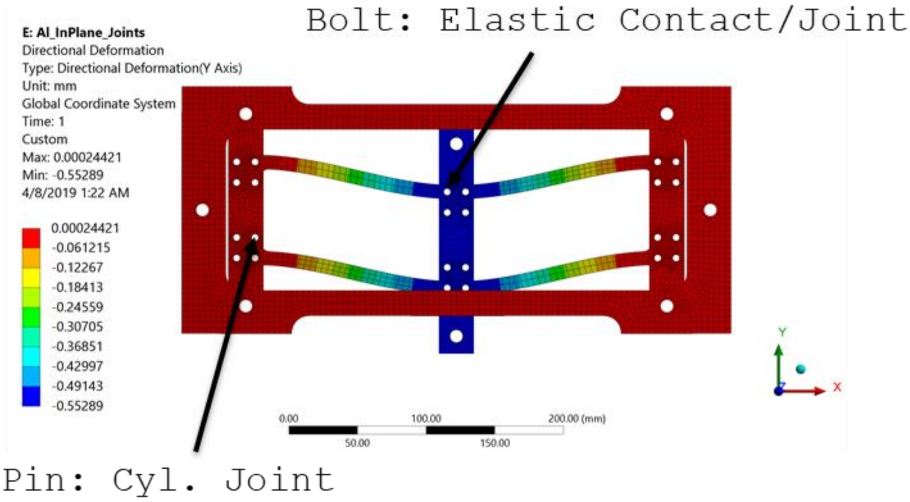

Figure 41 Displacement in the load direction for the out of plane (top) and in plane (bottom) load cases, with Aluminum flanges/interlinks.

4.2.1 Radial Test

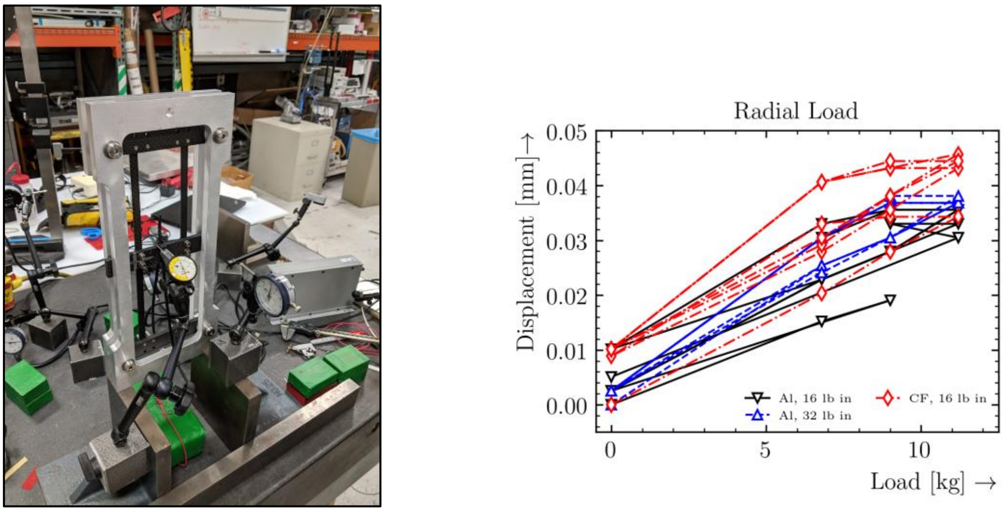

Figure 42 Radial loading configuration and measured displacement

In the last static test the interlinks were loaded 'radially'. The weight was applied in the middle of the flange, introducing tension in the top interlinks and compression in the bottom ones. The measured displacement, shown in Figure 42 along with the test set-up, was equal to 30 μm. This was significantly larger than the expected displacement, equal to 10 μm. It is difficult to understand where this difference comes from, as the problem is clearly very simple to solve. The only factor that might explain the mismatch in the stiffness is the fact that only a part of the interlinks is carrying the load. If this is the case the difference would probably be negligible in a global assembly with more links, where the different tolerances can redistribute the load. There was no discernible impact of the torque applied on the bolts.

This document is uncontrolled when printed. Check the EDMS to verify that this is the correct version before use

4.2.2 Dynamic Test

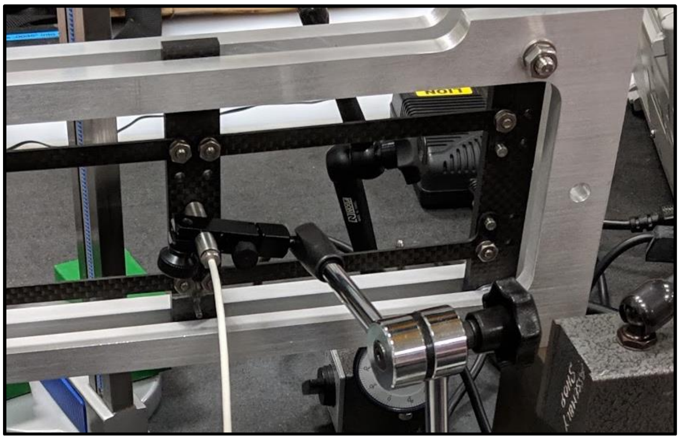

Figure 43 Capacitive probe set-up used to measure the impulse excitation response of the interlink/flange system

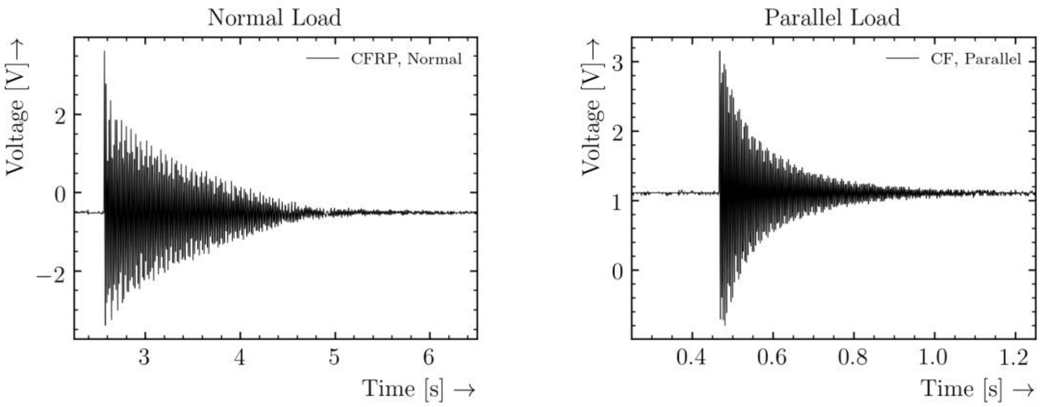

Figure 44 Dynamic test results under normal load excitation (left) and parallel load (right).

The set-up was then excited with an impulse (hit with a small rod) and the response was measured by means of a capacitive probe. The experiment, whose results are shown in Figure 44 for a representative run, allows to estimate the fundamental frequency and the amplification factor of the system. These are useful to estimate then the modal response of the whole SB system under the excitation from externally applied random vibrations. The critical frequencies were found to be 250 Hz and 60.2 Hz for the normal and parallel load respectively.

4.2.3 FE Model Calibration

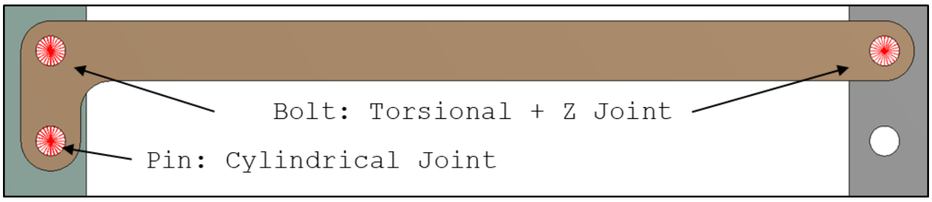

Figure 45 MPC constraints used in the FE models

This document is uncontrolled when printed. Check the EDMS to verify that this is the correct version before use

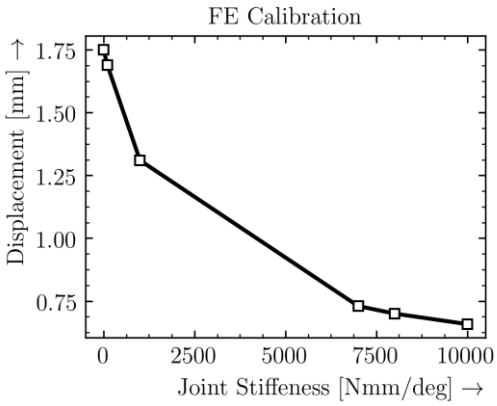

Figure 46 FE calibration results: the best fit is obtained assuming a joint torsional stiffness of 7000 Nmm/deg.

The pin and bolt are represented in the FE models by means of MPC constraint (ANSYS element MPC184). As showed in Figure 45, the pins are considered as cylindrical joints, blocking the relative motion in the plane, and allowing the motion and rotation on the bolt axis; the bolts instead are introduced applying a torsional joint with a specified stiffness opposing the hole axis rotation, and an additional lock for the longitudinal (z axis) displacements.

A parametric analysis of the FE model of the interlink/flange set-up was performed to calibrate the results on the experimental results. The displacements as function of the applied bolt cylindrical stiffness is shown in Figure 46. The solution is bound by the hinge solution when the stiffness is very small, and to a rigid link for stiffness higher than 10000 Nmm/deg. The best fit of the measured displacement, for the higher torque of 32 lbs-in are obtained assuming a joint torsional stiffness of 7000 Nmm/deg.

The modal solution (free body) obtained with this strategy is shown in Figure 47.The relevant modes are the 1st and 4th one. Their fundamental frequency is equal respectively to 63 Hz and 278 Hz. With respect to the measured values, this represent a 5% and an 11% error. Considering that the boundary conditions are not exactly the same as in the experiment this seems acceptable.

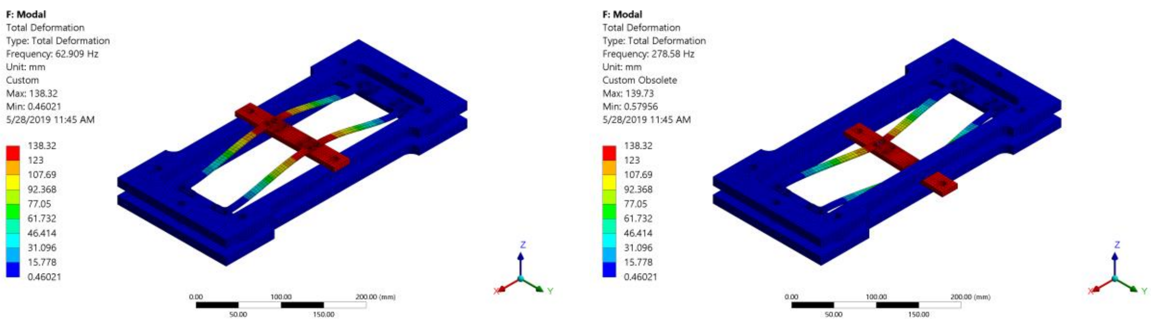

Figure 47 Modal solution: 1st mode (normal load) computed frequency is 63 Hz; 4th mode (parallel load) frequency is 278 Hz.

This document is uncontrolled when printed. Check the EDMS to verify that this is the correct version before use

4.3 Preload Loss Measurements

Figure 48 Specimen for preload loss measurement. A total of 6 bolts were bolted in this configuration.

It was shown in the previous sections that the preload impact significantly only the results for the *parallel* loads. The same impact was not detected on the integrated FE model: here, varying the torsional stiffness of the joints does not affect the overall performances in a measurable way. This is due to design of the strip barrel: the interlinks are generally able to carry the load in the stiffer radial direction. This mechanism design does not allow for the rotation around the bolts that is increasing the measured displacement on the interlink test set-up.

Nevertheless, to guarantee that the bolts are behaving as intended, an experimental campaign to verify the preload loss as a function of the time and temperature was started. The preload variation was verified on dedicated specimen, shown in Figure 48. This specimen is composed of two CN-80 plates, connected by means of Titanium bolts. The elongation during bolting was measured with a micrometre. This value is obviously proportional to the pressure and frictional force developed between the plates. The resulting displacements for the six bolts as a function of the applied torque are shown in Figure 49: the measured points can be fit with a line, with a R^2 of 0.9. The first three bolts (I, II and III in Figure 49) where loaded to a target torque of 16 in-lbs. The total length of the bolts was then measured every once in a while for a total period of 2 months. No real preload loss was detected. As a consequence, three more bolts (IV, V and VI in Figure 49) where preloaded to the higher value of 32 in-lbs.

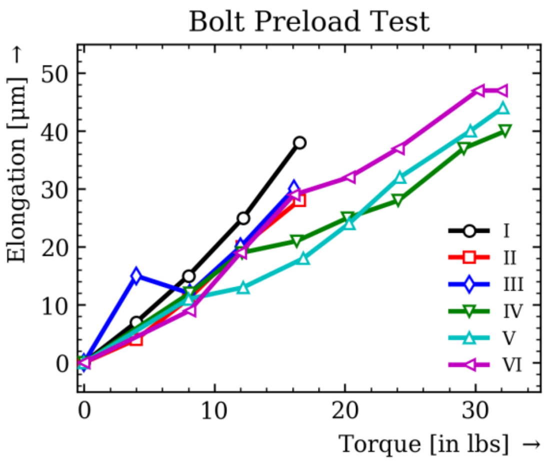

Figure 49 Bolt elongation as a function of the applied torque.

This document is uncontrolled when printed. Check the EDMS to verify that this is the correct version before use

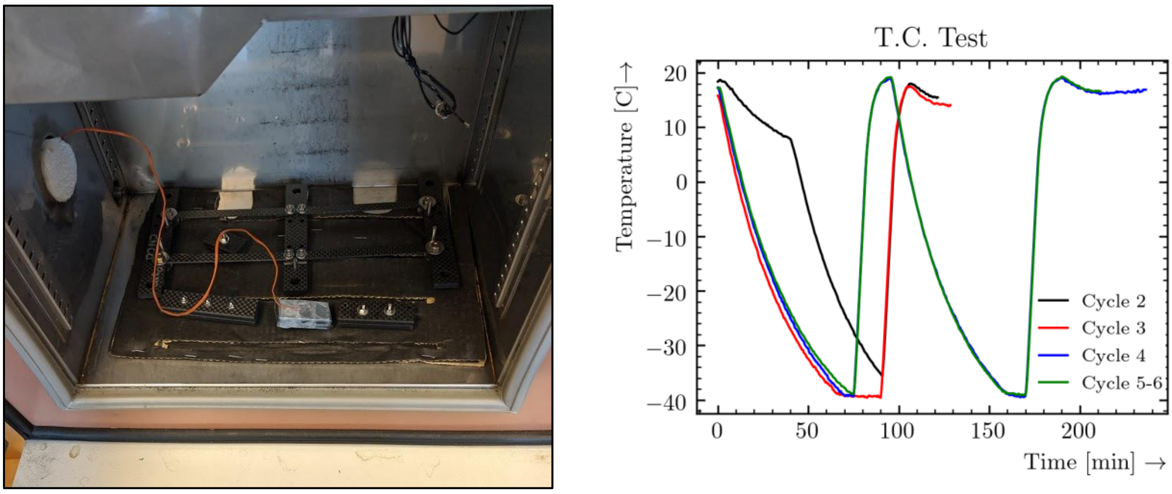

Figure 50 Interlinks/Flange and bolted specimen in the thermal chamber (left). Thermal cycle test results: the overall time to thermal cycle all the specimen is of 90 minutes.

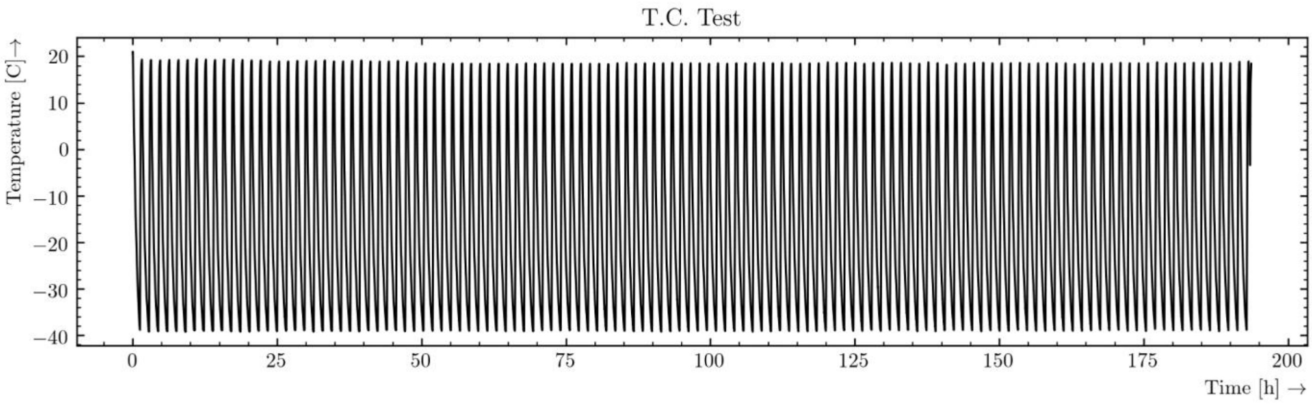

Figure 51 Measured CFRP temperature during cycling in the thermal chamber.

The bolts and the interlink/flange set-up where then introduced in a thermal chamber and cycled from room temperature, 20 °C, to the minimum operating temperature of the detector, -40 °C. A picture of the specimen in the thermal chamber is provided in Figure 50, left. The picture also shows an additional set of two plates taped together. A thermocouple is inserted between the plates to measure the temperature at the center of the specimen. This allows to verify that the thermal cycle design is correct and the desired temperature is reached everywhere in the specimen. A number of thermal cycle tests were performed. The resulting measured temperature on the CFRP is shown in Figure 50, right. The final cycle duration was of 90 minutes. 135 cycles were performed in total. The measured temperature during these cycles is shown in Figure 51: the thermal chamber performed as expected and the fiber always reached the target warm and cold temperatures.

The interlink-flange set-up was then reassembled in the fixture and tested. Figure 52 shows the static deflection in the *parallel* direction after assembly, after 1 week, after the 1st thermal cycle and after the 135 cycles. The measurements show a variability of ±25 µm, probably due to the angle between the dial gauges and the moving flange. The experiment result suggests that there is no preload loss due to the thermal cycling.

This document is uncontrolled when printed. Check the EDMS to verify that this is the correct version before use

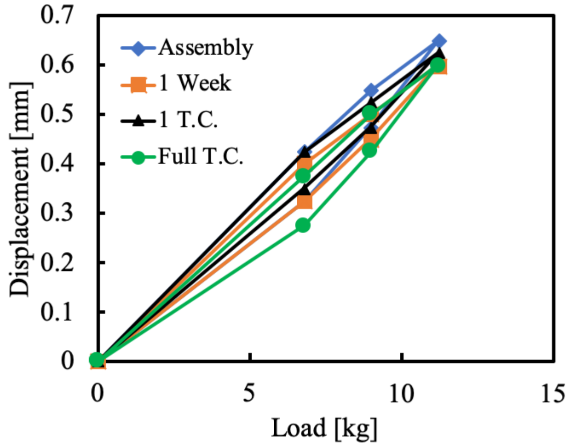

Figure 52 Static response variation of the interlink set-up under parallel load.

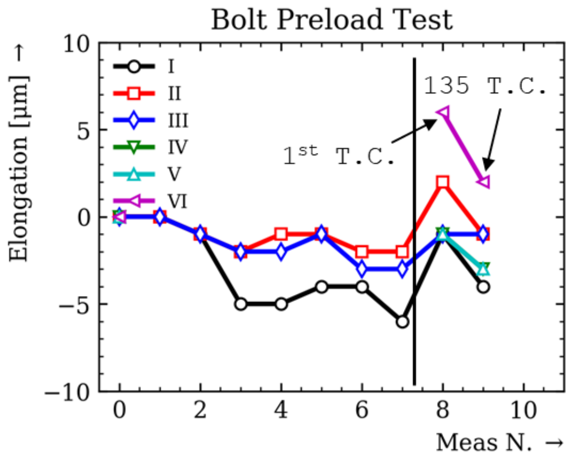

Figure 53 Bolt length measurement as a function of the time and temperature cycles.

The measurement results from the bolt lengths are shown in Figure 53: there is also here a random variability of the measurements. The results suggest that the measurement error is within at least ±2.5 µm.

4.4

4.5 PST Design

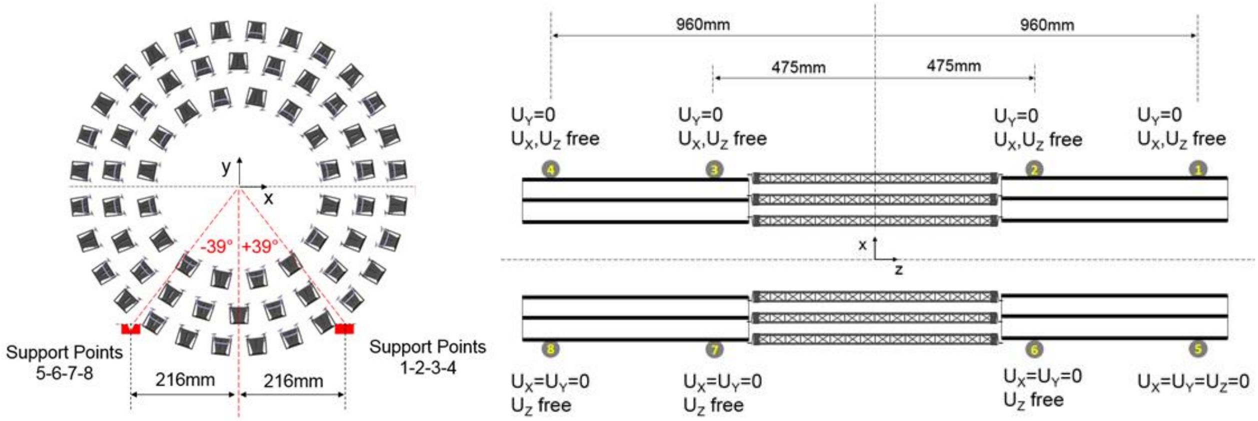

This document is uncontrolled when printed. Check the EDMS to verify that this is the correct version before use

Figure 54 Configuration of the Pixel Support Tube supports: on the left, the location in the X-Y plane, and on the right their longitudinal (Z) position. Drawings courtesy of x.

The PST supports the Pixel Barrel and Pixel End-Caps. The weight of each of these components is expected to be equal to 200 kg. The Pixel End-Caps will be supported by 4 supports on 2 longitudinal locations. As a consequence, neglecting the impact of possible alignment errors, it is possible to assume that the structural load will be equally distributed. The Pixel Barrel will be instead supported on eight locations distributed on four longitudinal positions, as showed in Figure 54. The distribution of the loads will then be a function of the relative stiffness of the Pixel barrel and the PST (and the rest of the ITk). In particular, a stiffer Pixel will increase the amount of force applied on the higher z locations (4/8 and 1/5 in Figure 54). A softer Pixel will instead deform following the deformations of the PST and increase the load applied to the central support locations (3/7 and 2/6 in Figure 54). At the present moment, the design of the Pixel barrel is still under development. It was therefore not possible to obtain a safe value for the stiffness of the Pixel. It was then modelled as a circular beam made of black Titanium, with an outer radius of 295 mm, equal to half of the external radius of the Pixel Barrel, and a thickness of 0.6 mm.

Figure 55 shows the deformation obtained considering the current local supports location. The deformed shape well shows that the results may be significantly impacted by the load location. In particular, when the load is introduced far from the stiffeners, there is a significant contribution of the local deflection. To avoid local deformations of this component it would be useful to move the support points in corresponding locations to the local stiffener. This option is being considered. As the hat stiffeners cannot be moved (their location is dictated by the stave geometry), another option would be to add further stiffening features where the load is introduced. This can be considered once the Pixel design will be at a more advanced stage.

In the meantime, the support location was moved in correspondence of the closest hat stiffener. The resulting deformation is shown in Figure 56 and Figure 57 with two different lay-up configurations. The significant increase in stiffness obtained with the second configuration is due to the increase of the fiber angle with respect to the z-axis, providing in this way an increased bending stiffness in the XY plane.

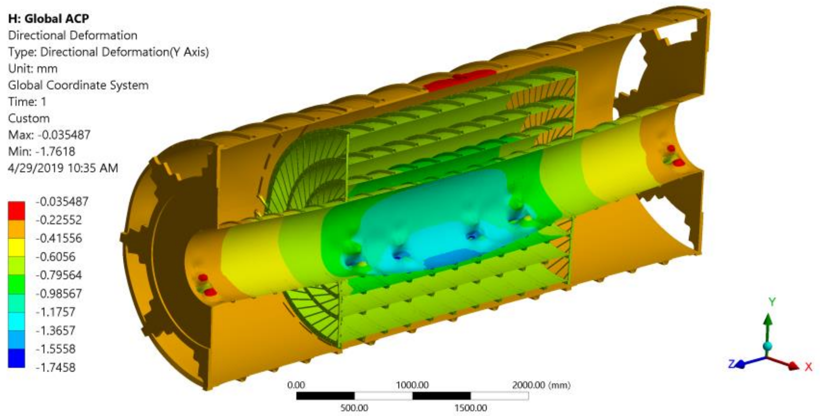

Figure 55 FE solution representative of the effect obtained introducing the PST loads far from the hat stiffeners. The local deflection is contributing to most of the total deformation.

This document is uncontrolled when printed. Check the EDMS to verify that this is the correct version before use

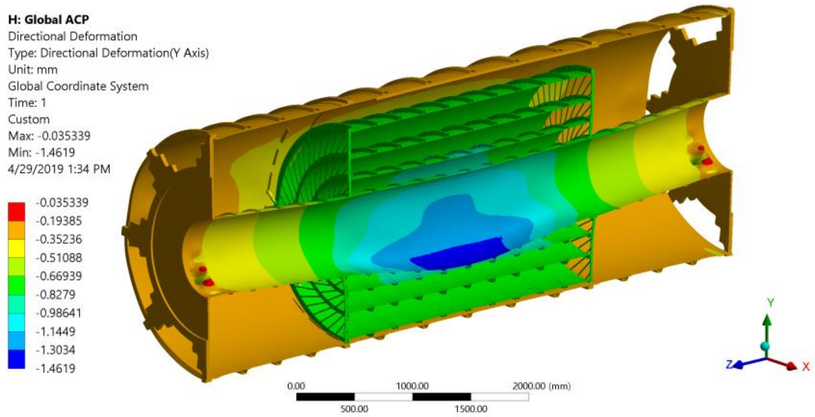

Figure 56 Displacements moving the barrel Pixel loads in correspondence of hat stiffeners.

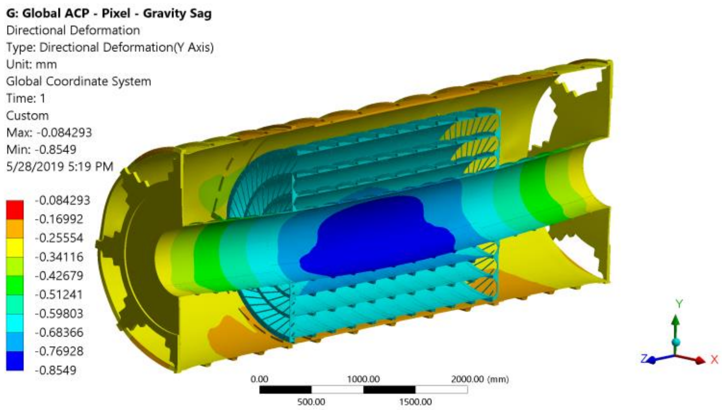

Figure 57 PST deformation after optimization of the CFRP shell, hats and rails lay-ups, and introducing the stiffness of the Pixel barrel.

This document is uncontrolled when printed. Check the EDMS to verify that this is the correct version before use

5 INTEGRATED MODEL ANALYSIS

A detailed model interfacing the outer cylinder, the strip barrel, the structural bulkhead, the pixel barrel and the Pixel Support Tube (PST) was produced. The model mesh is shown in Figure 58. The model allowed to study the effective interaction between the various components and define the interfaces in detail, verifying their performances. The section presents all the assumptions behind the modelling, describing the geometry, the mesh, the connections and the loads applied. The model was used to test the performances of the structure not only under the most critical conditions but also under the variety of loads that will be applied during the detector assembly. The main cases studied were the static deflection during operation, the thermal contraction from room temperature to the operating temperature, the RMS stability study and the strength verification during the lifting of the ITk. Finally, a summary of the results from the simulation of the assembly procedure.

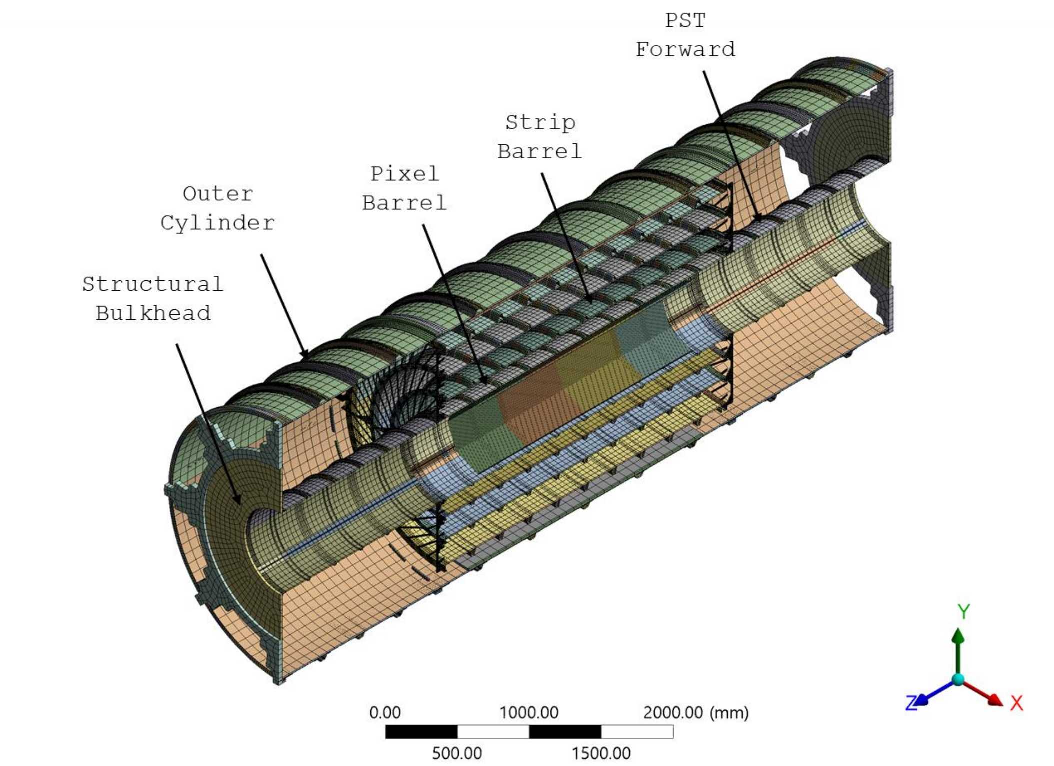

Figure 58 Integrated model mesh and components.

This document is uncontrolled when printed. Check the EDMS to verify that this is the correct version before use

5.1 OC Model Description and Inner Warm Vessel stiffeness update

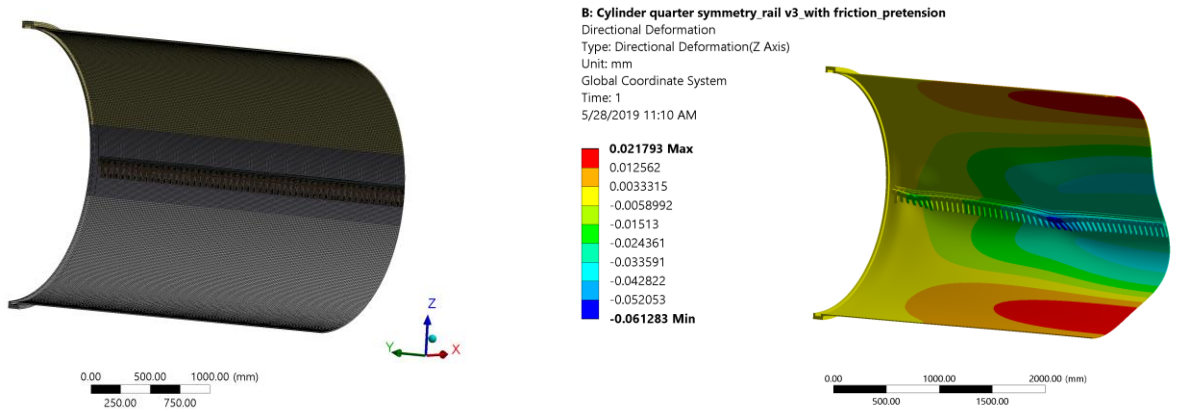

Figure 59 IWV model mesh and vertical deformation under the ITk loads. A vertical load of 1000 N was applied on the two support locations.

As a result of the analysis described in Section 3, the OC radius was increased of 8 mm [X]. This allows to use the shorter bolt and the stiffer of the two possible design solutions presented. The mounting pad thickness was kept at 8 mm.

The model was further developed removing the simplifying assumption of black titanium everywhere, and instead modelling each composite ply by means of the ACP code in ANSYS. The two models results were very similar in terms of static performances, validating the modelling assumption used to design the OC. One important advantage of the composite model is the possibility of verifying accurately the strength of the structure.

The OC model was slightly updated from the one used from the optimization. In particular, the IWV vessel stiffness was updated with a more accurate model, whose mesh is shown in Figure 59 (left). It is important to notice that the deformation of the rails, shown in Figure 59 (right), is a local motion, and that loads applied on the two rail locations do not interact with each other in a meaningful way. This means that our assumptions of schematizing the IWV with separate springs in the integrated model is correct and the introduction of the whole model would not add significant different contribution to the overall performances. The new model allowed to improve the stiffness estimation. The new parameters are:

$$K_A = K_C = 50\ kN/mm$$
$$K_{AM} = K_{MC} = 18\ KN/mm$$

This is slightly higher in the central supports and lower for the extreme ones than the values used for the OC design optimization. In particular, this results in a 44% increase in the middle and 22% reduction at the extremities. The overall effect is beneficial for the overall stability, as the load is now more uniformly distributed and the softer part is stiffened.

This document is uncontrolled when printed. Check the EDMS to verify that this is the correct version before use

5.2 Integrated Model Connections

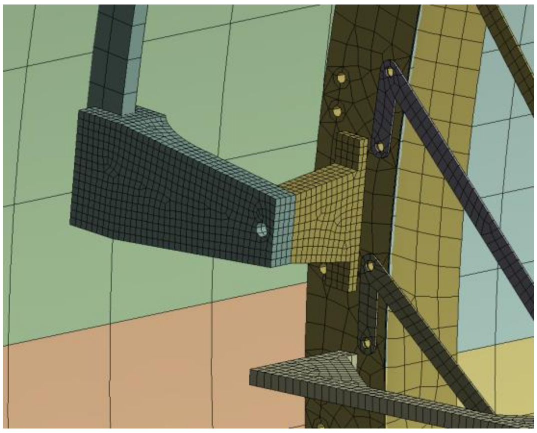

Figure 60 Strip Barrel to Outer Cylinder connection brackets.

The connections between the various parts are introduced by means of bonded connections or MPC links. In particular: the structural bulkhead is glued (bonded contact) to the PST forwards and the OC flange; the PST forward and PST barrel are connected by gluing their facing flanges; the OC and the Strip Barrel are connected with apposite brackets. The brackets are shown in Figure 60. These components are made of two pieces, connected with a hinge that allows their relative rotation across the z-axis. The hinge connection is used to avoid the introduction of a local moment in the Strip Barrel flange. All the hinges but one are also left free in the z-direction: this allows to leave the connection iso-static and avoid the introduction of high local loads in the case of a significant differential thermal contraction between the strip barrel and the OC. The Pixel connection to the Strip Barrel is discussed in the Section 4.

5.3 Weights and External Loads

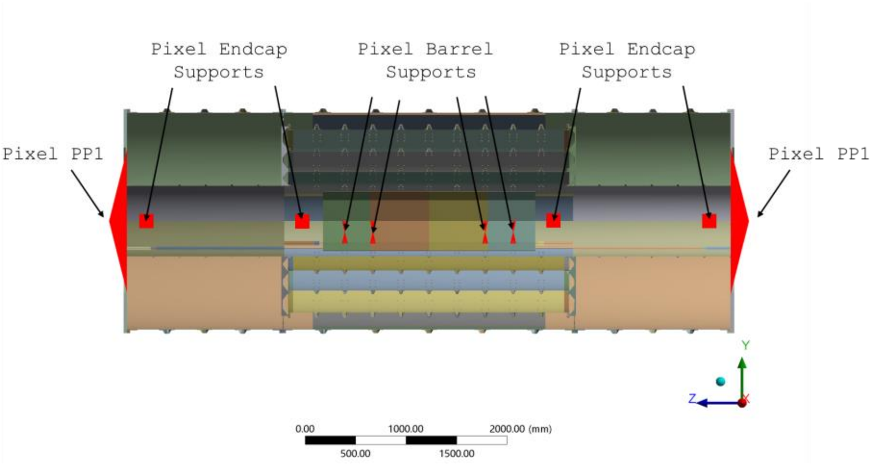

Figure 61 Pixel weights and structural connections locations

The external loads are mostly introduced as point masses, connected via MPC to the main structure. The connection of the Strip Barrel services and End-caps point masses to the OC was described in Section 3. Similarly, the point masses representing the staves connection to the Strip Barrel was explored in Section 4. The weights coming from the Pixel detector are shown in Figure 61, and listed in Table 7. The Pixel barrel is represented by an equivalent beam and attached to the Strip Barrel rail via MPC constraints. This allows to correctly distribute the load among the 8

This document is uncontrolled when printed. Check the EDMS to verify that this is the correct version before use

supports in the 4 longitudinal locations. External loads were applied or removed depending on the load case studied. They are reported in each load case paragraph.

Table 7 Pixel weights and structural connections locations

Name	Structure	Weight	Z
/	/	*kg*	*m*
PP1 z+	BH	150	3163
PP1 z-	BH	150	-3163
Pixel Endcap AA	PST Fwd	50	2720.8
Pixel Endcap AM	PST Barrel	50	1110.4
Pixel Endcap MC	PST Barrel	50	-1110.4
Pixel Endcap CC	PST Fwd	50	-2720.8
Pixel Barrel 1	PST Barrel	50*	832.8
Pixel Barrel 2	PST Barrel	50*	555.2
Pixel Barrel 3	PST Barrel	50*	-555.2
Pixel Barrel 4	PST Barrel	50*	-832.8
Total		680	

**The total weight is applied on the Pixel Barrel (beam)*

5.4 Structural Bulkhead Design

The structural bulkhead design is discussed in [6]. Its design contributes substantially to the longitudinal stiffness of the system, and as a consequence to the first fundamental frequency. It does also increase the stiffness in the vertical plane, reducing the gravity sag. The baseline design (Figure 62, left) considers a honeycomb structure with two CN-60 skins of 1 mm thickness each, and honeycomb core of 16 mm and 32 mm thickness, respectively in the centre and external regions. The decreased thickness at lower radius allows to leave more space to the Pixel services, With the baseline design, the total reaction forces and moments exchanged with the PST forwards for each bulkhead are:

$$F_x = 215\ N$$
$$F_y = 1334\ N$$
$$F_z = 23\ N$$
$$M_x = 310\ Nm$$
$$M_y = 18\ Nm$$
$$M_z = 8\ Nm$$

It is important to notice that the total weight that would be directly applied on the structural bulkhead is the one coming from the Pixel forwards. This is equal to 100 kg in total. The vertical reaction F_y and the corresponding moment M_x should be in this case be much smaller. This means that an important portion of the load carried by the structure is actually flowing through the bulkhead, which significantly contributes in avoid the rotation of the end-surfaces of the detector.

A secondary design is also kept as an option in case an increase of the longitudinal stiffness of the ITk would be required. This design, shown in Figure 62 (right), considers a 36 mm thick core along the whole Bulkhead. The gravity sag with the baseline design is equal to 0.86 mm. The corresponding deformation is shown in Figure 63 (top). The first modal shape is shown in Figure 63 (bot). The relative fundamental frequency is equal to 6.8 Hz. Similar results are shown in Figure

This document is uncontrolled when printed. Check the EDMS to verify that this is the correct version before use

64 for the alternative design. In this case the gravity sag is also equal to 0.86 mm. The first frequency is instead increased to 7.3 Hz (7% increase).

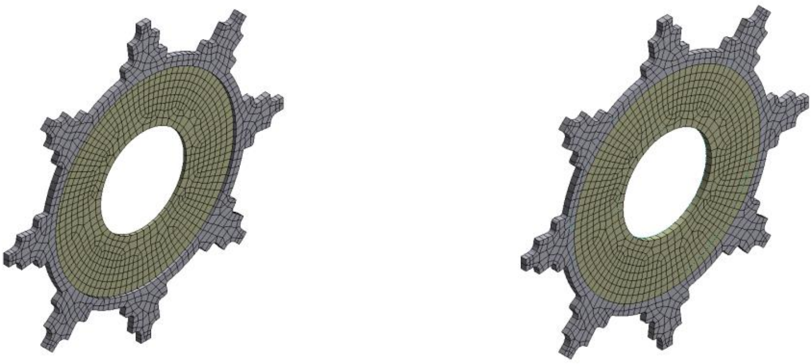

Figure 62 Configuration schemes for the bulkhead: baseline (left) and alternative (right).

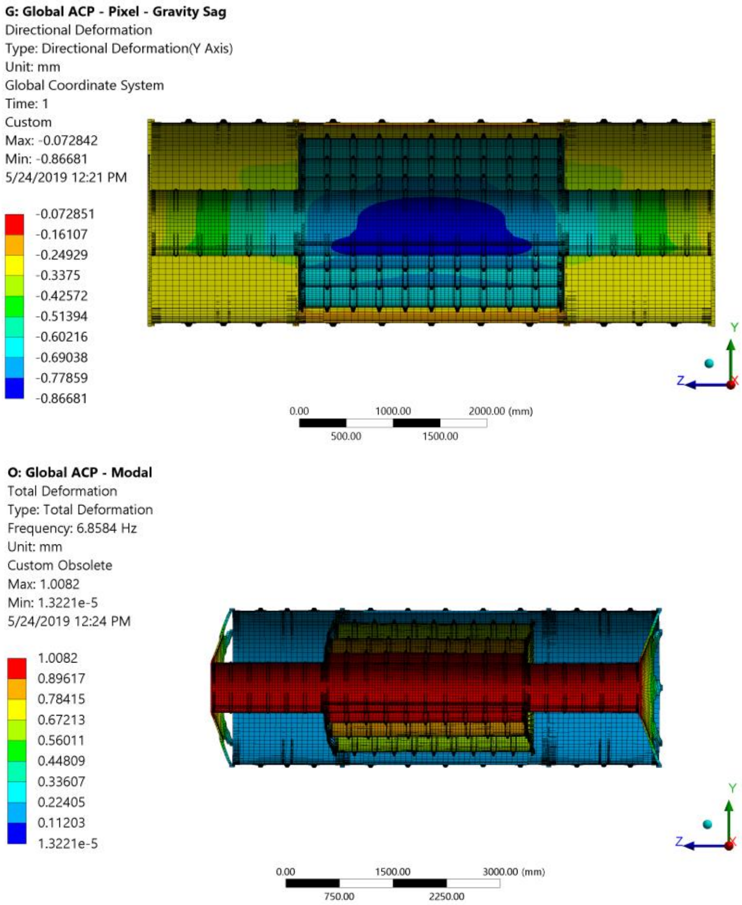

Figure 63 Gravity sag and first mode shape with baseline design

This document is uncontrolled when printed. Check the EDMS to verify that this is the correct version before use

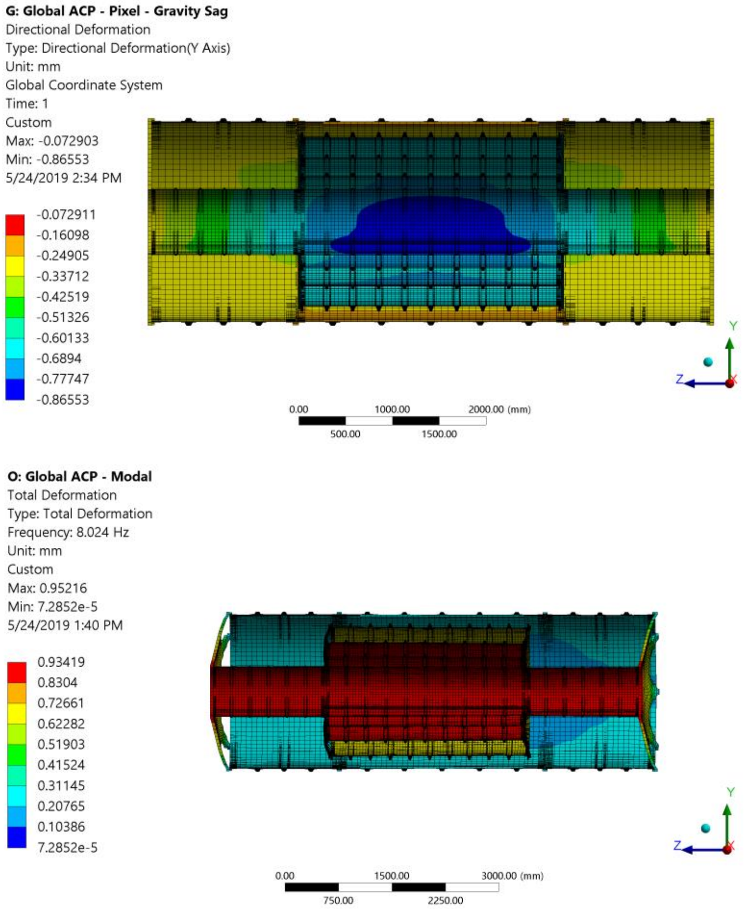

Figure 64 Gravity sag and first mode shape with backup solution for the bulkhead design

5.5 Gravity Sag

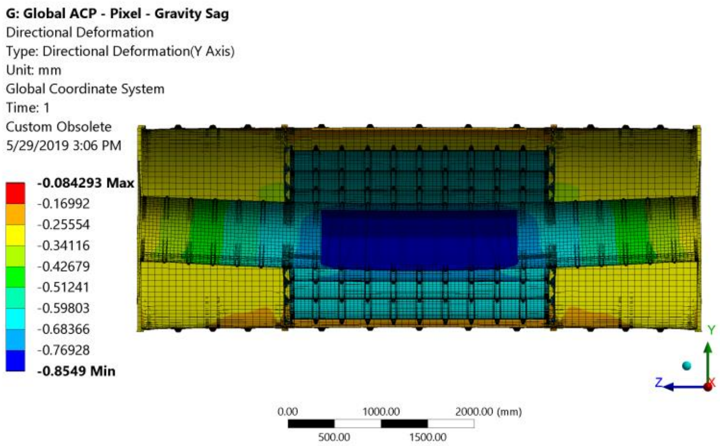

Figure 65 Gravity sag of the integrated model. The maximum vertical displacement is equal to 0.85 mm at the beam representing the Pixel barrel.

The gravity sag results are still used as a comparison. It is also interesting to evaluate the performances when compared to the OC simplified model and finally the contributions to the overall sag from the various components. The deformation at the beam representing the Pixel barrel is equal to 0.85 mm. The displacement contours and the deformed shape (200x) are shown

This document is uncontrolled when printed. Check the EDMS to verify that this is the correct version before use

in Figure 66. It is interesting to study how much each component contributes to this total deformation:

- IWV rails: the deformation is equal to 84 μm at the extreme supports and 170 μm for the central ones. This corresponds to a vertical force of respectively 4216 N and 3040 N on each support.
- OC: the structure deforms of 197 μm. Summing this contribution to the IWV one the displacement at brackets supports is equal to 367 μm.
- OC/SB brackets: the displacement across the brackets is equal to 266 μm. This is due to the local rotation of the OC supports, to the local rotation at the hinge joints between the two parts, and finally to the actual deformation of the joint. A number of preliminary analysis of stiffer brackets was produced. A sample result with a very stiff bracket is shown in Figure 69: the displacement across the bracket in this case is equal to 110 μm. This number represent a limit performance and the contribution of the rotation of the OC supports. The intrinsic deformation of the bracket (also counting the hinge rotation) is equal to 150 μm.
- Strip barrel: the vertical deformation is equal to 243 μm. Most of this deformation is actually introduced in the PST: the vertical deformation at the L1 shell is in fact equal to 699 μm, meaning that the L1, L2 and L3 layers deform in total 87 μm, about one third of the total deformation at the barrel. This significant deformation of the PST is due to the weight of the Pixel barrel, which is applied far from the flanges/interlink/braces system, responsible for most of the Strip Barrel stiffness.

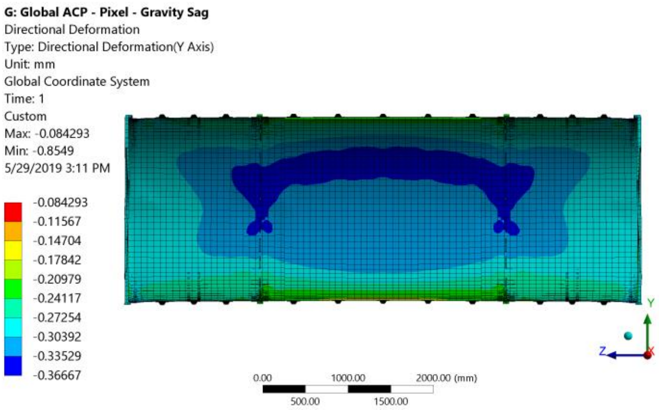

Figure 66 Vertical deformation of the OC and Structural Bulkhead

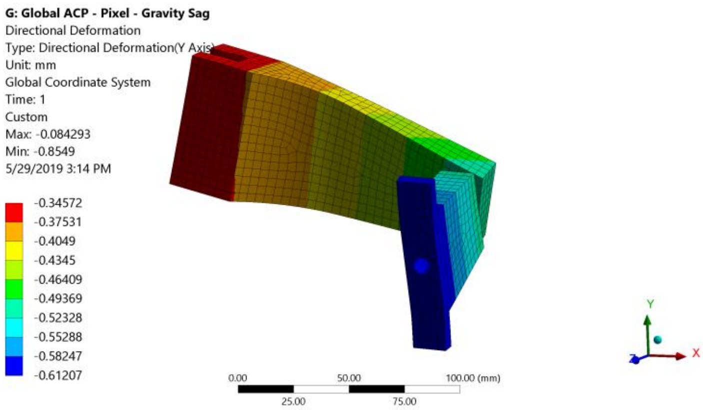

Figure 67 Vertical deformation of the OC/Strip Barrel brackets

This document is uncontrolled when printed. Check the EDMS to verify that this is the correct version before use

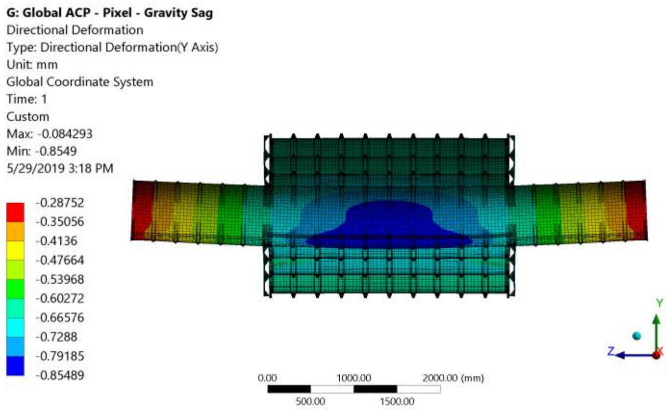

Figure 68 Vertical deformation of the Strip Barrel and PST forwards.

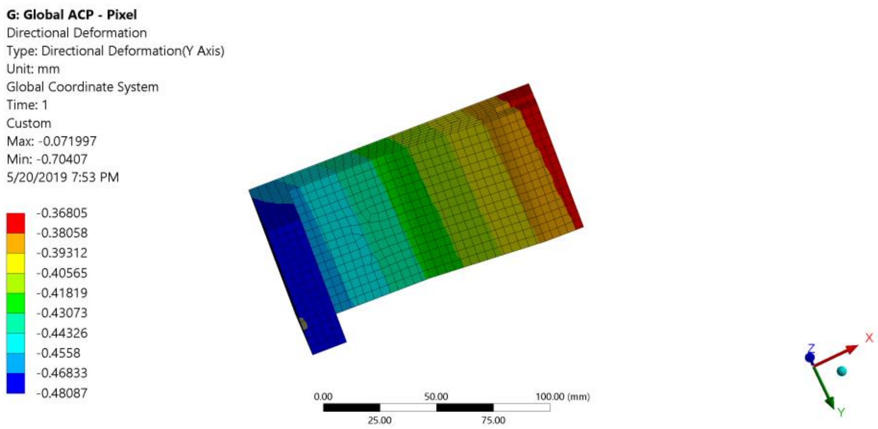

Figure 69 Stiffer design (not compatible with the envelopes) for the OC brackets. With a total deformation of 0.11 mm the design shows a limit case for the performance reachable at the bracket.

5.6 Thermal Contraction Analysis

The operating temperature of the ITk is -40 °C. In the document [3] this temperature is assumed to have variations contained within ±1 °C. The present study aims to check the deformations during the cooldown from room temperature (20 °C) to the operating temperature of -40 °C, verifying the deformations in the various directions and possible . The computed results can then be linearly scaled to the expected total variation of 2 °C.

The first step necessary is to compute the expected thermal contraction of the fibers. The in-plane Coefficient of Thermal Expansion (CTE) of a laminate, simplified to a system of parallel springs, can be computed as:

$$\alpha_x = \frac{\varepsilon_x}{\Delta T} = \frac{A_{22}N_x^N - A_{12}N_y^N}{A_{11}A_{22} - A_{12}^2}$$

$$\alpha_y = \frac{\varepsilon_y}{\Delta T} = \frac{A_{22}N_y^N - A_{12}N_x^N}{A_{11}A_{22} - A_{12}^2}$$

In the normal direction is instead possible to neglect the contribution of the fiber and to assume the contraction to be the same as the one of the matrix. The system behave in this case as spring in series and is possible to neglect the contribution of the fiber. For typical CFRP the fiber has a modulus of 2 orders of magnitude higher than the matrix, and a CTE 2 orders of magnitude lower

This document is uncontrolled when printed. Check the EDMS to verify that this is the correct version before use

and of opposite sign. Figure 71 shows typical CTE values are shown for Pitch and PAN based fibers. The higher the modulus, the higher the negative thermal contraction is. In general, the opposite sign between the resin and fiber CTE brings the total CTE to very low values. It also allows the designer to combine particular fiber/matrix systems to obtain a null thermal contraction.

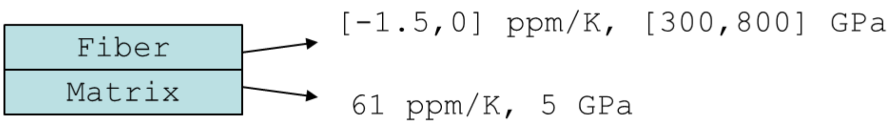

Figure 70 Simplified schematization of the

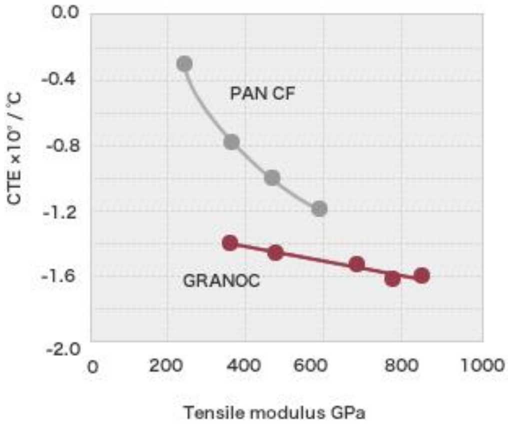

Figure 71 Typical CTE values as a function of the fiber tensile modulus for PAN and Pitch based fibers.

The final CTE depends on the lay-up strategy, the fiber and resin material, and then it could be reasonable to ask for a measurement of this property. As it is very small, it is very difficult to measure it. As a consequence here we limit ourselves to bound the problem with an high value of CTE for the lower modulus fibers (CN-60, M55J), assumed to be equal to +1 ppm/K, and a high (negative) CTE for the higher modulus fibers (CN-80, K13C2U), assumed to be equal to -0.5 ppm ppm/K.

The total deformation of the system is shown in Figure 72. The maximum total displacement is equal to 0.44 mm. Most of the displacement is in the longitudinal direction, and due differential thermal contraction between the PST structure and the OC+SB system that bends outward the bulkhead. The radial displacement is contained within ±130 μm. The azimuthal displacement within ±50 μm, the longitudinal one within ±200 μm. The last one is in particular all negative as the system contracts (the OC has a positive CTE) and the only roller blocked in the z-direction is at the lower z location.

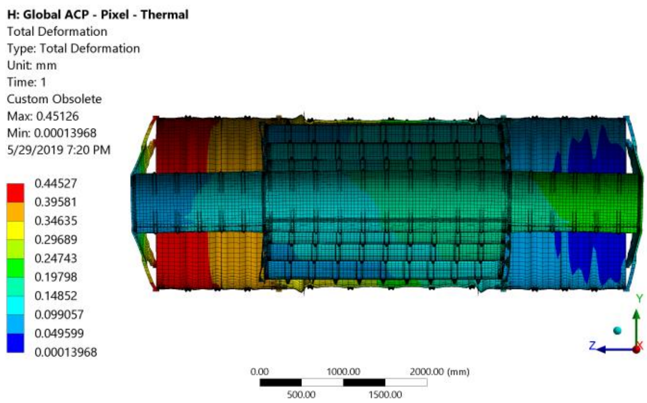

This document is uncontrolled when printed. Check the EDMS to verify that this is the correct version before use

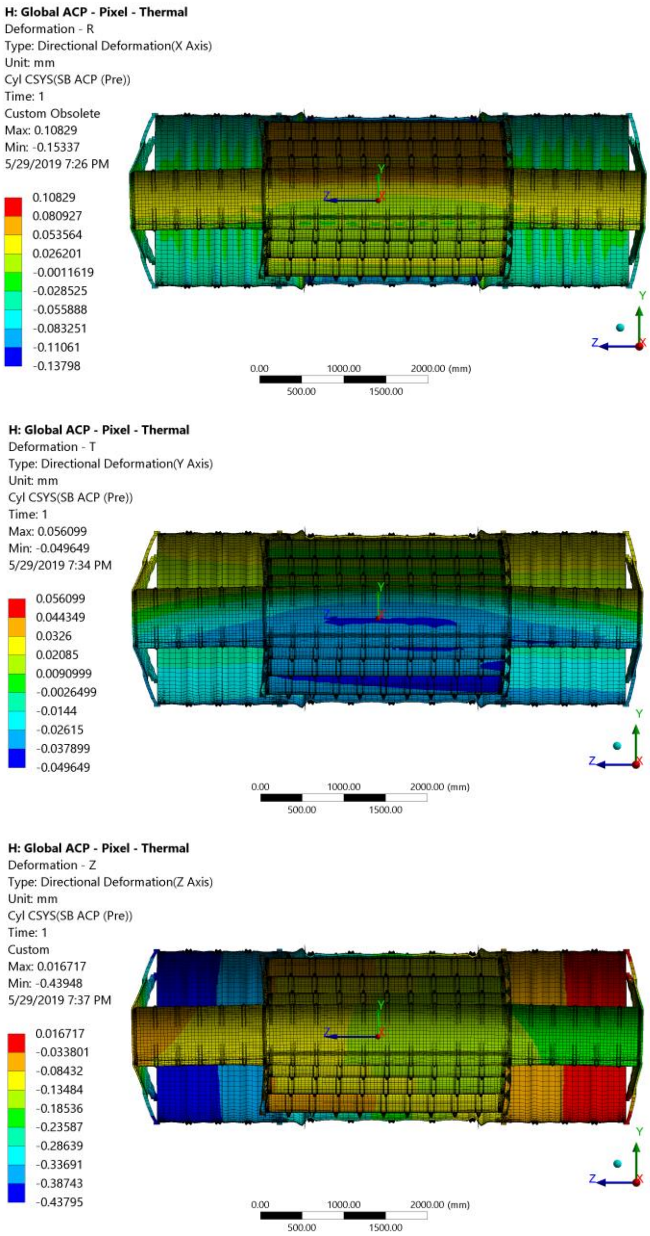

Figure 72 Thermal deformation from 20 °C to -40 °C. The contours show the following deformations (from top to bottom): total, radial, azimuthal, longitudinal.

As the system is linear, these displacements can be scaled to obtain the stability of the system for the specified thermal variations of ±1 °C. Scaling from the simulation ΔT of 60°C this means that the radial stability will be within 4.3 μm, the azimuthal one within 1.6 μm, and the longitudinal one within 6.6 μm. This is lower than the requirement of 2 μm in the azimuthal direction and 20 μm in the radial direction for strips [3]. For the medium period timescale the expected temperature variations are of ±3 °C. In this case the requirement is to contain the azimuthal motions within 5 μm. The analysis produces a value of 4.8 μm. It is important to underline that these result were obtained with very conservative assumptions.

This document is uncontrolled when printed. Check the EDMS to verify that this is the correct version before use

5.7 Moisture Study

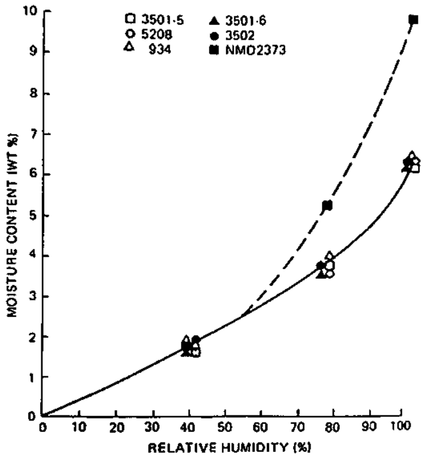

Figure 73 Moisture absorption for various resins from 0% to 100% relative humidity [7]**.**

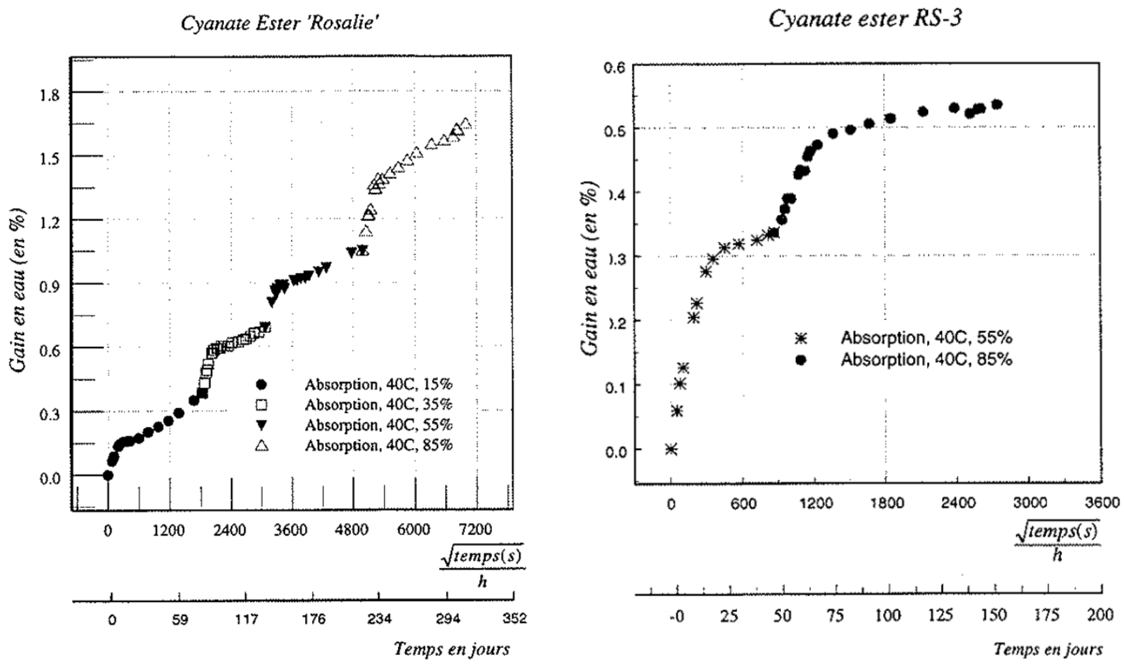

Figure 74 Moisture absorption for two different cyanide ester resins from 0% to 100% saturation [8]**.**

The Coefficient of Moisture Expansion (CME) of a composite plate can be computed following a procedure similar to the one used for the CTE. The main difference in this case is the amount of time needed to produce the deformation, which is much longer for the moisture expansion. A typical CFRP resin expands of about 0.17% from fully dry to completely wet. As the carbon fiber expansion can be instead assumed to be close to 0, and considering a quasi-isotropic laminate we can write the simplified formula:

$$\beta_{tot} = \frac{E_m V_m \beta_m}{E_m V_m + E_f V_f} \frac{1}{V_m}$$

This document is uncontrolled when printed. Check the EDMS to verify that this is the correct version before use

Where β_{tot} is the CME of the laminate in the fiber plane, E_m the modulus of the resin, E_f the modulus of the laminate (conservative assumption), V_m and V_f the volume percentage of matrix and fiber, and β_m the CME of the resin matrix. We have to divide for the matrix volume percentage again as the CME is specific to the mass increase, that is not happening in the laminate. Assuming that in the transverse direction the matrix dominates the contraction we obtain the values reported in Table 8. The values refer to the % of weight increase in the composite. The amount of absorption for some resins is shown in Figure 73, from [7]: the values range up to 10% of absorption in mass. The absorption for two different cyanate ester resins are instead shown in Figure 74. More details on the measurement process can be found in [8]. For our case it is possible to extract for an RS-3 resin a value of 0.55% for an 85% saturation. Extrapolating to 100% this would mean 0.65% weight increase. For a CN-60 plate, using the values in Table 8, the total expansion from fully saturated to fully dry would produce a variation of 156 µm. This is consistent with what was measured in [9]. More conservatively, hereafter we consider a value of 1%.

The CME can be introduced in the ANSYS model as a thermal expansion coefficient. The thermal loads can then be applied only to the composite parts and the resulting deformation can be studied. The temperature variation applied was equal to 1 °C, equivalent to a process going from fully saturated to fully dry. This is clearly a limiting case and in reality the moisture variation will be significantly lower. However, as the analysis results are linear, they can easily be scaled to more representative moisture variation, as for example from 50% saturated to fully dry.

The expected deformation can be roughly computed considering as initial dimension the length of the cylinders (6 m) and their diameter (2.2 m). With a 1% variation, and assuming that all the cylinder is made out of CN-60, the expected variation is equal to 0.48 m in the radial direction and 1.44 mm in the longitudinal direction. Using instead 0.65% we obtain instead 0.31 mm and 0.94 mm.

The computed values are shown in Figure 75: the total variation for the X, Y and Z direction are equal to 0.56 mm, 0.32 mm, and 1.38 mm. This is very close to what was expected from the simple hand calculation explained above. The deformation cannot be simply described as radial in a fixed reference system as the horizontal constraint (V-shape rollers) are only on one side of the detector. As a consequence, the resulting motion is not symmetric. The results can be scaled to a reasonable moisture variation of 0.65%, getting 0.36 mm, 0.21 mm and 0.90 mm in the X, Y and Z direction respectively.

Table 8 CME values for the resin, honeycomb and laminates (weight percentage)

	β_x ppm/%	**β_z** ppm/%	**β_z** ppm/%
Resin	2500.0	2500.0	2500.0
M55J	91.5	2500.0	2500.0
CN-60	240.7	240.7	2500.0
CN-80	192.9	192.9	2500.0
K13C2U	50.8	2500.0	2500.0
Nomex	400.0	250.0	120.0

This document is uncontrolled when printed. Check the EDMS to verify that this is the correct version before use

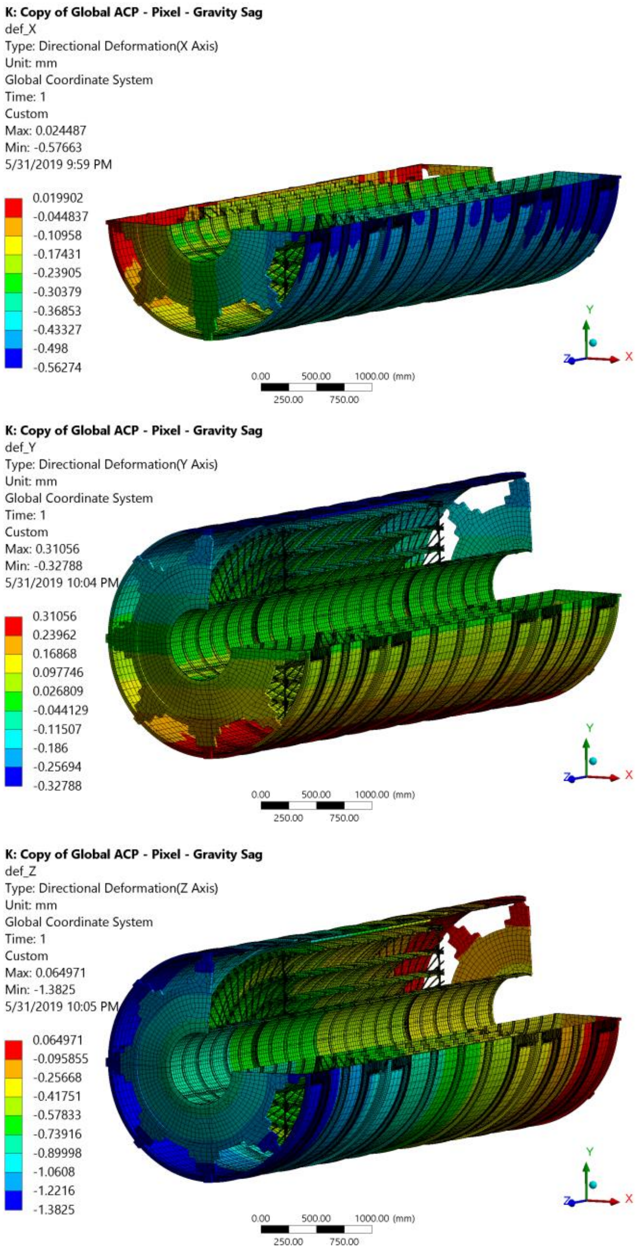

Figure 75 Deformations with a 1% humidity variation. From top to bottom: horizontal (X), vertical (Y), longitudinal (Z). The results can be scaled linearly to the desired humidity variation.

This document is uncontrolled when printed. Check the EDMS to verify that this is the correct version before use

5.8 Alignment Study: Missing Roller Scenario

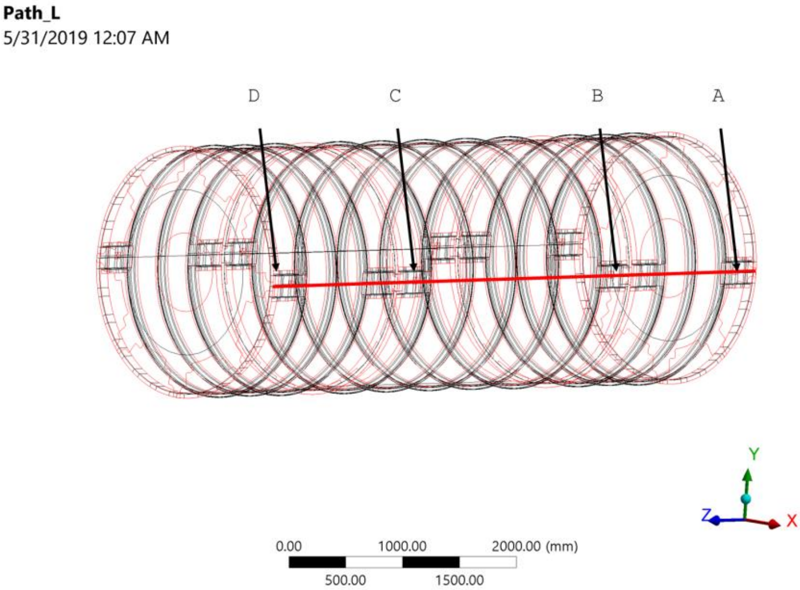

Figure 76 Symbols used to identify the rollers and path used to plot the vertical displacements along the OC shell.

This study tries to estimate the impact of a missing roller on the deflections of the ITk. This extreme case is useful to estimate the local deformation in case of a non-uniform height of the single rails. In other words, the model results obtained in this way can be used to understand reasonable requirements for the alignment of the IWV rails. Two cases are relevant for this analysis: removing a central roller (B or C in Figure 74) and a lateral one (A or D).

- **Case A:** the deformation and vertical displacement contours are shown in Figure 77. The total deformation is increased of about 0.1 mm. The force at the other rollers is equal to: 5170 N, 3947 N, 6121 N. For reference, the forces with all the rollers in contact are: 4216 N, 3040 N, 3040 N**,** 4216 N. This means that, as expected the roller that sees the greater increase in force is the one closer to the missing one.
- **Case B:** the deformation and vertical displacement contours are shown in Figure 78. The total deformation is increased of about 0.x mm. The force on the rollers is equal to: 5110 N, 4256 N and 5723 N. Also in this case the higher increase is in the roller closest to the removed one.

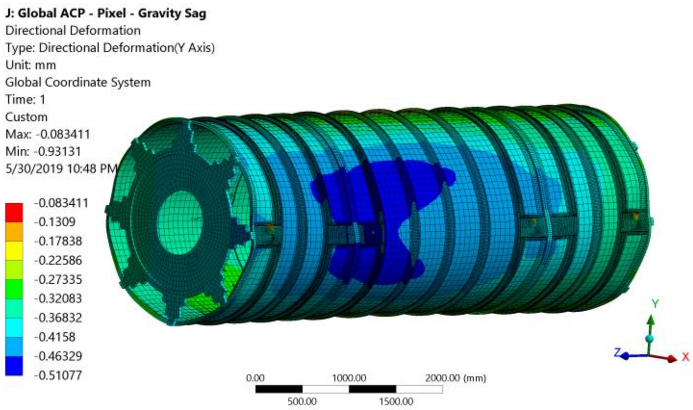

Figure 77 Gravity sag with a missing central roller. The maximum deformation is increased of 0.1 mm.

This document is uncontrolled when printed. Check the EDMS to verify that this is the correct version before use

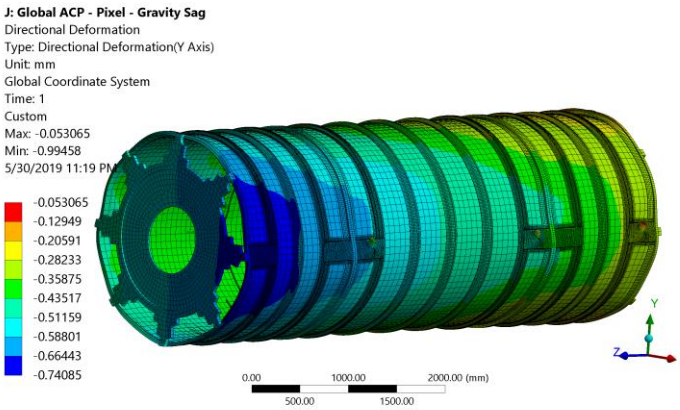

Figure 78 Gravity sag with a missing lateral roller. The maximum deformation is increased of 0.2 mm.

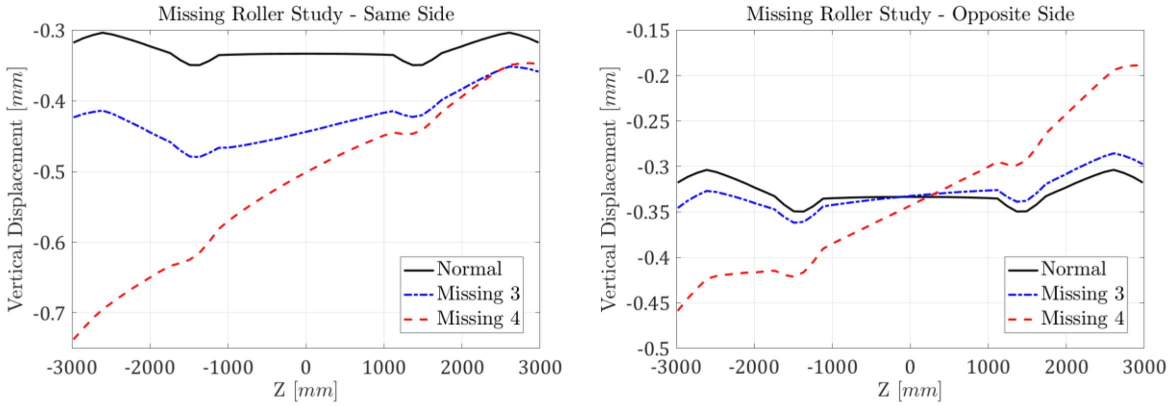

Figure 79 Deformation along the shell (Y=0), on the same side of the missing roller (left), and on the opposite side (right).

A comparison between the displacements along the horizontal plane of the shell is shown in the plot of Figure 79. The results shows that the displacement of the ITk are greater in correspondence of the missing roller, as expected. The increase in displacement is equal to 0.13 mm for the case A, and to 0.39 mm for the case B. The displacements computed on the opposite side show instead that the ITk rotates roughly around the centre to balance the system.

Measurements on the IWV have shown that the rails are aligned within ±0.250 mm. The vertical deflection due to the IWV deformation is always higher than this value, both in the standard cases and even more for the missing roller cases. The consequence is that, considering the measured rail alignment, the rollers are expected to be always in contact with the rails.

5.9 Modal Analysis

5.9.1 Description

The modal analysis is performed on the same model described in Section. However, a number of simplifications were introduced in order to avoid the generation of local low energy modes which are not significant for the stability of the sensors but that can prevent the successful analysis. For example, the masses representative of the services may generate a moment on the flange supports, and this is of relevance for the structural analysis in terms of total deformation and strength. It is however not of interest to study the vibration of these masses, and they were brought closer to their support. The pixel beams were also removed, as their stiffness was evaluated roughly. The load was instead considered as a distributed mass attached to the PST supports.

This document is uncontrolled when printed. Check the EDMS to verify that this is the correct version before use

5.9.2 Modal Solution

A modal analysis was performed for the fully assembled ITk. To compute the modal shapes and fundamental frequencies, the model was mostly kept the same, keeping the IWV springs and various constraints in place. The following simplification were however performed: the Pixel barrel beam was removed, as its own fundamental frequency is not considered of interest for this analysis and the modelling is so simplified that results may be very far from reality; the local masses representing the staves and the strip barrel services were moved close to the structural surface supporting them. This last assumption is necessary to get rid of the less interesting low-energy local modes that would have taken a heavy toll on the computational system, without contributing in a meaningful way to the displacements that are of actual interest for the design of the global structure.

The analysis allowed to optimize the roller positioning strategy: the location of the V-shaped ones has an effect on the first mode detected. In particular, the rotation across the Y-axis. To improve this behaviour is better to place the V-rollers on the first and last bolt. Figure 80 shows the first mode vibration when the x-motion is blocked at the first and last supports of the X+ roller. The same mode is shown in Figure 81 for a condition where the second and third roller are blocked instead. The fact that the supports are now closer reduces the stiffness of the system for an easier rotation across the Y-axis. The model is however neglecting the friction between the flat rollers and the rails: while motions on the x axis are allowed at the rollers, the horizontal force will actually not be 0, thus increasing the overall stiffness of the structure.

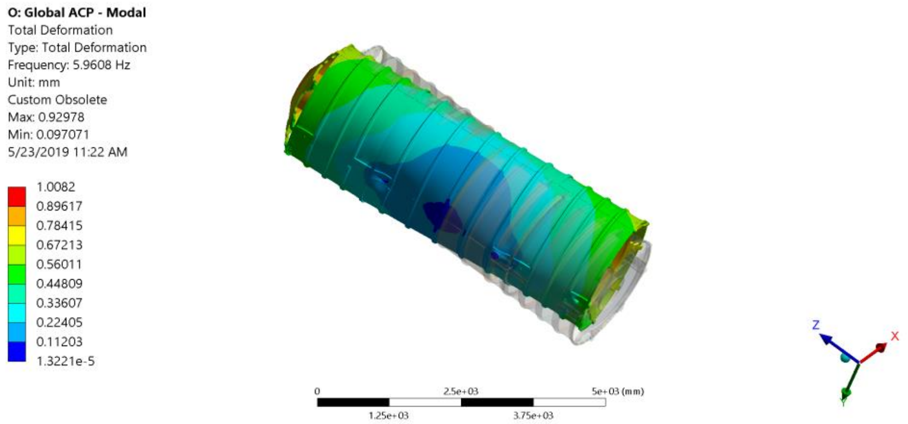

Figure 80 First vibration mode with the x-motion locked at the second and third bolts, X+ side. The small distance between the two bolts provides a relatively low stiffness against the rotation across the Y-axis.

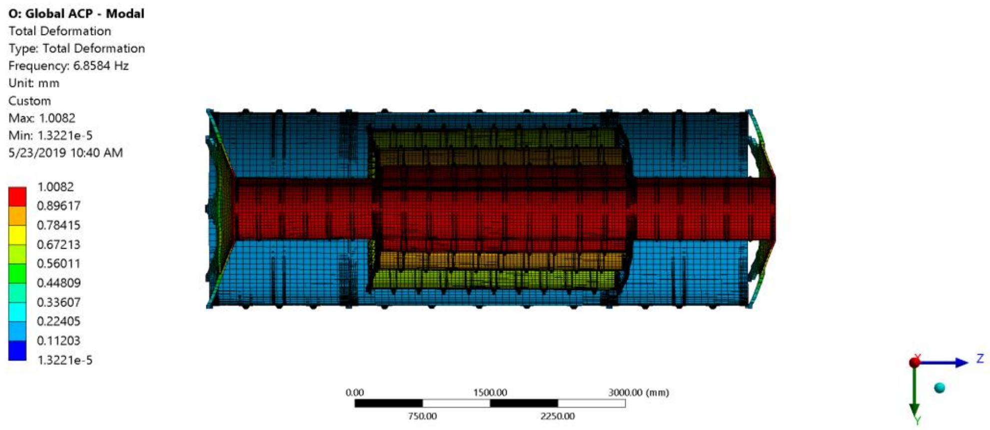

This document is uncontrolled when printed. Check the EDMS to verify that this is the correct version before use

Figure 81 First vibration mode with the x-motion locked at the first and last bolts, X+ side. The increased distance between the supports removes completely the rotation component of the first fundamental frequency.

The overall mode shapes are shown in Figure 82. The first six modes can be described as follows:

- **Mode 1, 6.8 Hz:** this is telescoping mode, mainly acting on the z-direction. As the OC/SB brackets are left mostly free in the z-direction, the only components that keep the various components from a relative motion are the z-braces and the structural bulkheads. The effect of the structural bulkhead thickness on this mode was studied in the previous subsection.
- **Mode 2, 10.9 Hz:** a mode exited in the horizontal plane, moving the whole structure in an almost rigid configuration. The mode is governed by the stiffness of the mount-pads. In reality this mode will likely be much higher in frequency as the friction between the flat rollers and the rails will substantially increase the overall stiffness.
- **Mode 3, 14.0 Hz:** this is the higher order version of the Mode 2. Again mostly a rigid motion in the horizontal plane, this time the mode produces a rotation around the y-axis. Similar considerations are valid as the Mode 2.
- **Mode 4, 17.1 Hz:** higher order telescope mode. The displayed shape involves more significantly the z-braces with respect to mode 1.
- **Mode 5, 20.2 Hz:** this is the first mode acting in the vertical direction. It has a shape very similar to the deflection obtained from the gravity sag study. The frequency is equal to 20.2 Hz. Using the approach proposed in Section 1, and having computed a gravity sag equal to 0.85 mm, the expected frequency would be equal to 17 Hz. This means that the simplified approach based on the gravity sag underestimates the related fundamental frequency of 15%. The sign of the error is due to the fact that in simplifying the system to a 1D oscillator, all the mass is assumed to be moving at the maximum displacement, while in reality that motion is smaller for significant portions of the system. This result confirms the correctness of the approach followed in designing the various components.
- **Mode 6, 20.6 Hz:** this mode mixes different shapes

Higher order modes obtained from the analysis are not reported here. However, it is important to keep them in the simulation for the random vibration analysis reported in the following paragraph, as they can contribute to increase the final stability results. The maximum mode obtained was number 12, with a fundamental frequency of 35 Hz.

This document is uncontrolled when printed. Check the EDMS to verify that this is the correct version before use

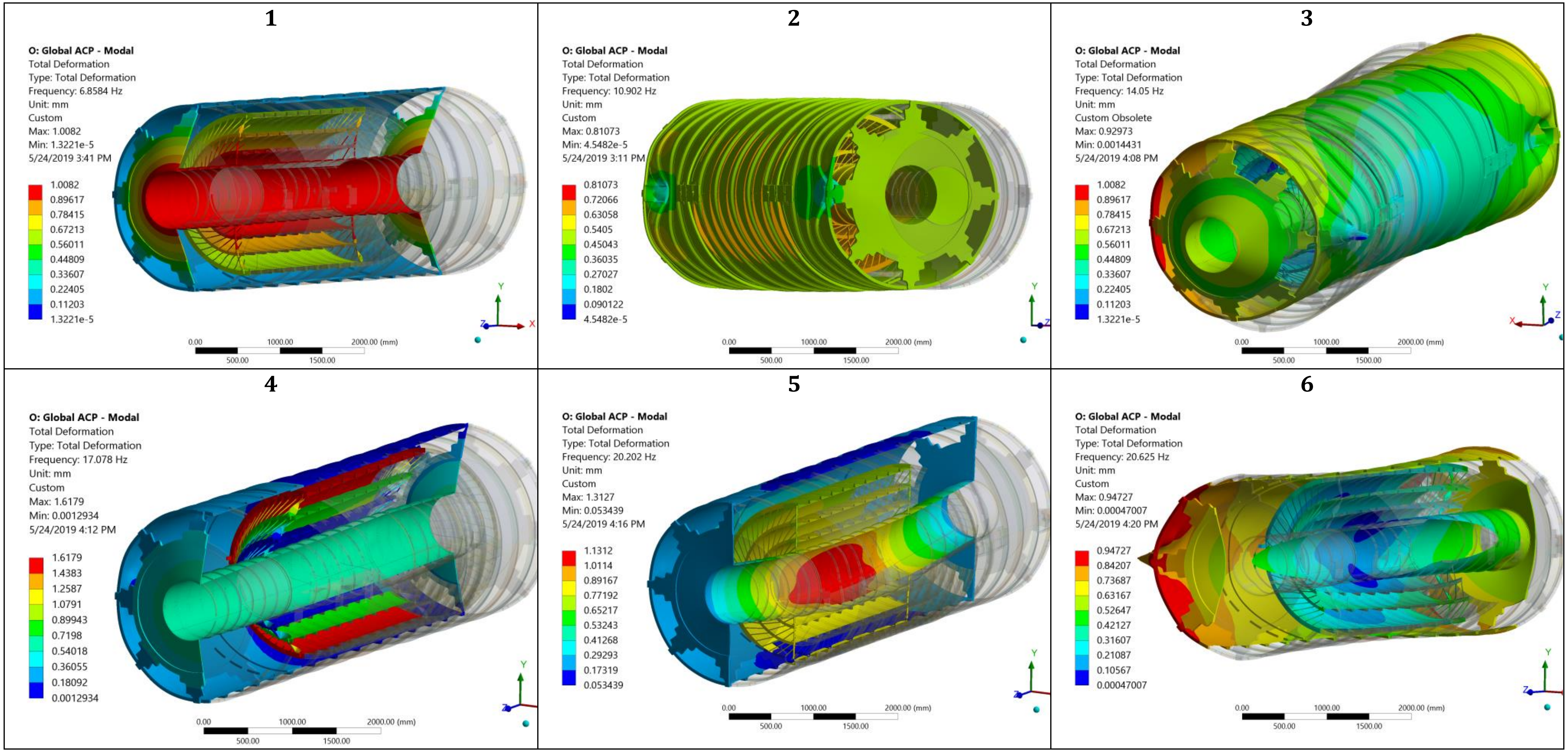

Figure 82 First six vibration mode shapes.

This document is uncontrolled when printed. Check the EDMS to verify that this is the correct version before use

5.9.3 Random Vibration Analysis

The total vibration is estimated extracting the normal distribution of the displacements when a vibration is applied at the boundary conditions. ANSYS computes the results in the solution coordinate system, Cartesian with standard definition for the X, Y, Z axis. This means that a rotation of these would be necessary to compute the results in a cylindrical coordinate system and obtain the results needed to compare the deformation with the required r, phi and z RMS stability. For a standard solution this rotation could be written for the node (i, j) as:

$$u'(x_i, y_i) = [T]u(x_i, y_i)$$

Or:

$$\begin{bmatrix} u'_{Ri} \\ u'_{\theta i} \end{bmatrix} = \begin{bmatrix} \cos\theta_i & \sin\theta_i) \\ -\sin\theta_i & \cos\theta_i \end{bmatrix} \begin{bmatrix} u_{xi} \\ u_{yi} \end{bmatrix}$$

As the output from the PSD analysis is actually the variance of these quantities (equal to the RMS for a normal distribution with null mean), one would need to compute the variance of the above quantities. This is:

$$\sigma^2(u_R) = \sigma^2(u_{xi}\cos\theta_i + u_{yi}\sin\theta_i)$$
$$= \cos^2\theta_i\,\sigma^2(u_{xi}) + \sin^2\theta_i\,\sigma^2(u_{yi}) + 2\cos\theta_i\sin\theta_i\,cov(u_{xi}, u_{yi})$$

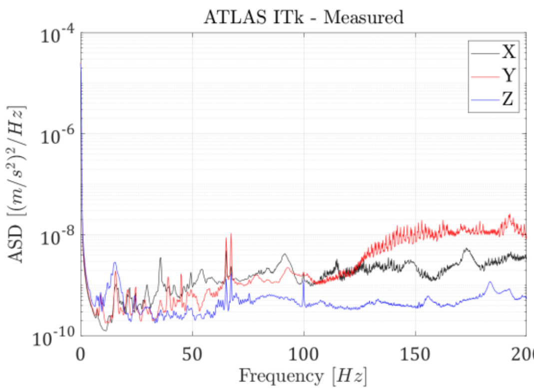

Figure 83 Measured accelerations at one end of the ATLAS IWV

The acceleration data shown in Figure 83 was measured at one end of the ATLAS IWV during the current operation. This data can be used both in the Miles equation (see Section 3), and in the FE model, where it is applied to the boundary conditions (the IWV rails). The Miles equation results are shown in Figure 84: the plot on the left shows the result obtained in the three directions using an amplification factor ζ equal to 0.01. The plot on the right shows instead the average displacement as a function of the amplification factor. The plot clearly shows that, applying the available measurements to the Miles equation, to contain the displacement below 1 µm is sufficient to keep the first fundamental frequency below 4 Hz.

The FE displacements obtained applying the measurements to the modal solution are shown in Figure 85 in the x, y and z direction. The displacements are as expected below 1 µm in all directions. In particular, the RMS displacement in the x-direction is within 0.3 µm, in the y-direction within 0.2 µm, and in the z-direction within 0.8 µm. Clearly the higher displacement in the z-direction is expected, as the lowest fundamental frequencies correspond to the telescopic modes. The small displacements found are of the same order of magnitude of the predictions from Miles equation: the first fundamental frequency, involving mainly motions in the z-direction, is equal to 6.8 Hz, which would correspond to an RMS motion of about 0.3 µm. The 4-th fundamental

This document is uncontrolled when printed. Check the EDMS to verify that this is the correct version before use

frequency contributes to another 0.1 µm. A similar reasoning applies also to the X and Y axis, where the equation also catches the order of magnitude of the displacements, but underestimating them.

A number of analysis was run in order to verify the impact of the number of modes obtained from the modal analysis on the maximum RMS displacements: the displacement variation after the first 6 modes is very low. For example, moving from 6 to 12 modes produces variations in the results lower than 10e-9 m.

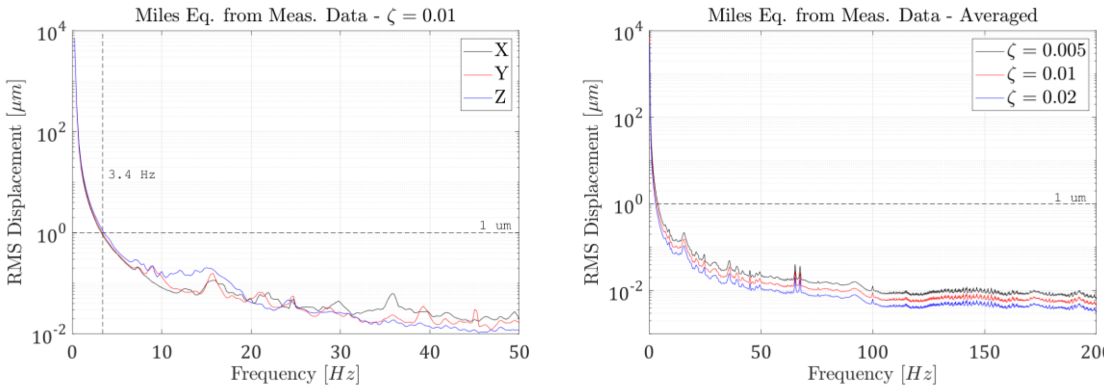

Figure 84 Miles equation results in the three directions with an amplification factor of 0.01, and for the average output as a function of the amplification factor.

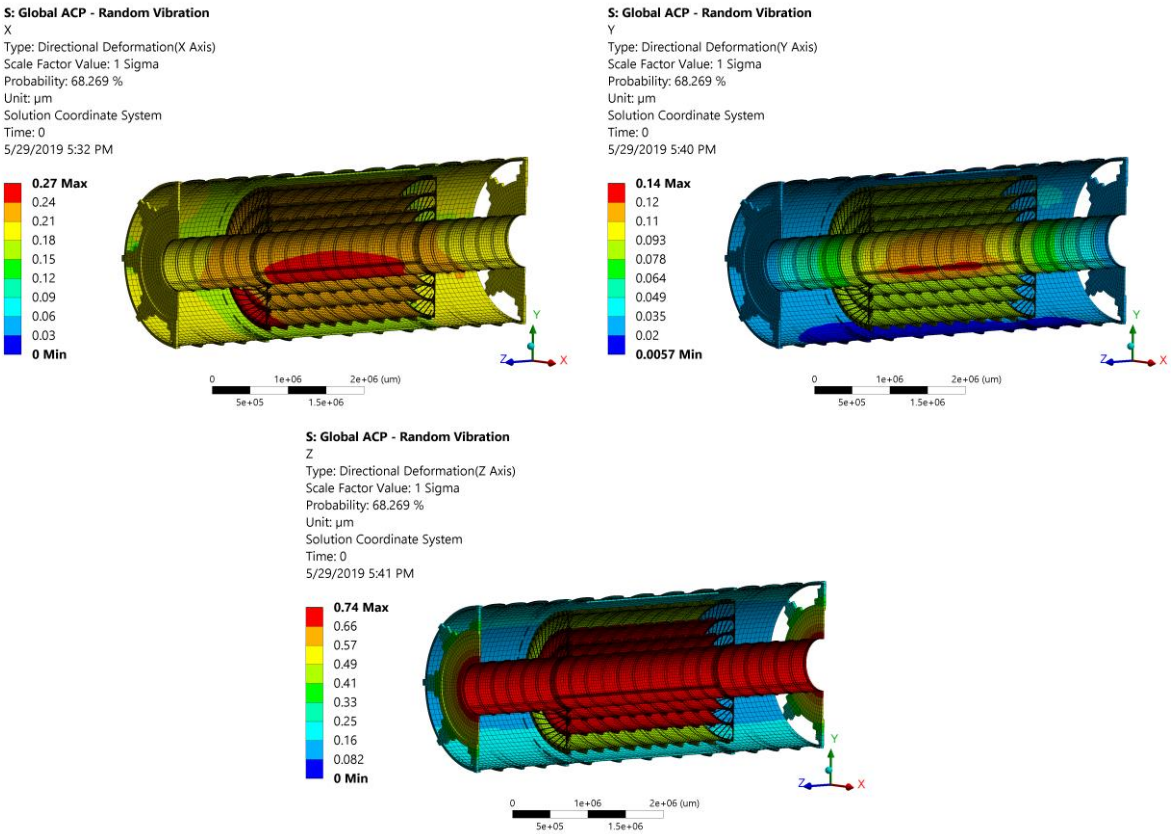

Figure 85 Random vibration response (measured in µm) of the integrated model in the X (top left), Y (top right), and Z (bot) directions. The response is lower than 1 µm in all directions.

This document is uncontrolled when printed. Check the EDMS to verify that this is the correct version before use

5.10 Strength Verification

The strength of the structure was verified during lifting, as this is the most critical load. Past measurements shown that the maximum acceleration applied on the structure would be in the vertical direction and equal to 1.8g. In the computations shown hereafter the acceleration applied was conservatively assumed to be equal to 2g.

The results are used to extract the maximum strain allowed in the composite plies. This allows to verify the structure against the so-called first ply failure criteria: if the maximum strain in the fibers is lower than the critical strain the ply will not fail. This is a rather conservative criteria, as the structure is not expected to fail immediately after the first failure: the other plies could in general be able to carry part of the load after the first-ply failure and increase the actual strength of the laminate. The criteria can be written as:

$$f = \max\left(\left|\frac{\varepsilon_1}{X_\varepsilon}\right|, \left|\frac{\varepsilon_2}{Y_\varepsilon}\right|, \left|\frac{\gamma_{12}}{S_\varepsilon}\right|\right) < 1$$

Where the reference system 1-2-3 is the ply principal coordinate system. If L_f is the failure load, L_a the applied load, we can define the safety factor SF as:

$$SF = \frac{L_f}{L_a}$$

Failure is experienced when the Safety Factor is lower than 1. The Inverse Reserve Factor IRF is then simply defined as:

$$IRF = \frac{1}{SF} = \frac{L_a}{L_f}$$

Failure obviously occurs when the Inverse Reserve Factor is higher than one, and does not occur when it is lower than one. Hereafter we will plot the Inverse Reserve Factor as it allows to highlight show 'dangerous' zones more efficiently (higher values, in red, are more dangerous).

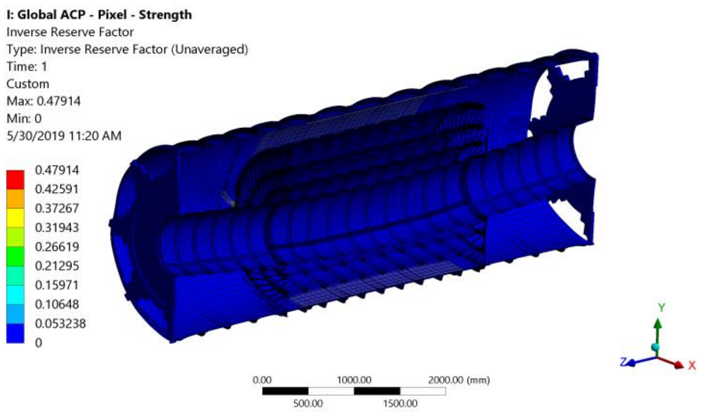

Figure 86 Inverse Reserve Factor overview: the maximum value is equal to 0.47 in this analysis. Most of the components are very far from their strength limits.

This document is uncontrolled when printed. Check the EDMS to verify that this is the correct version before use

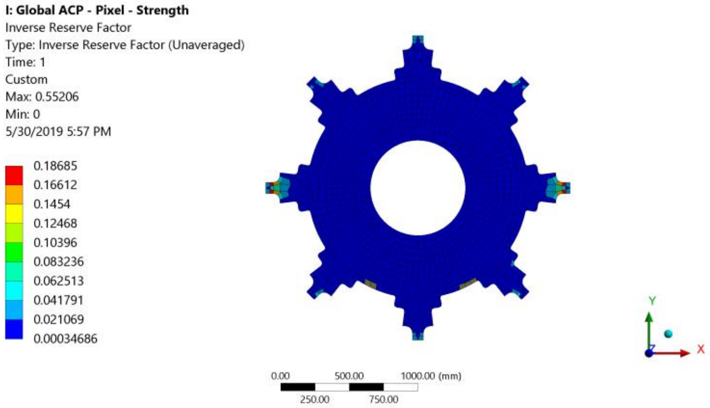

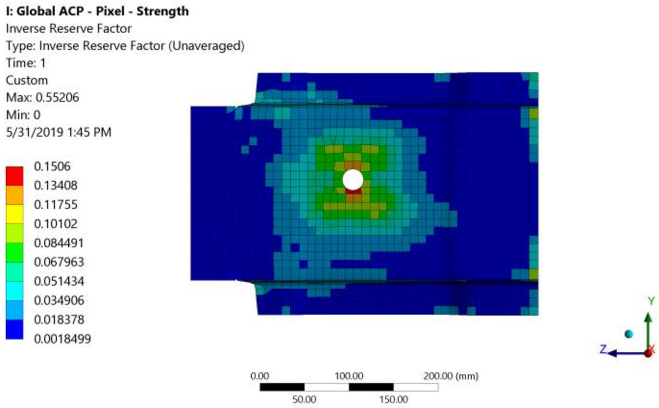

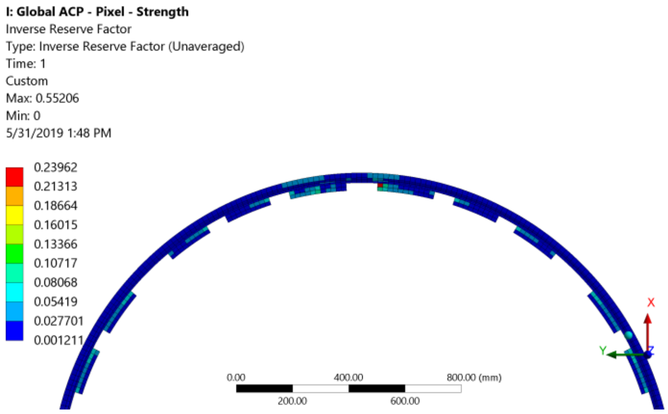

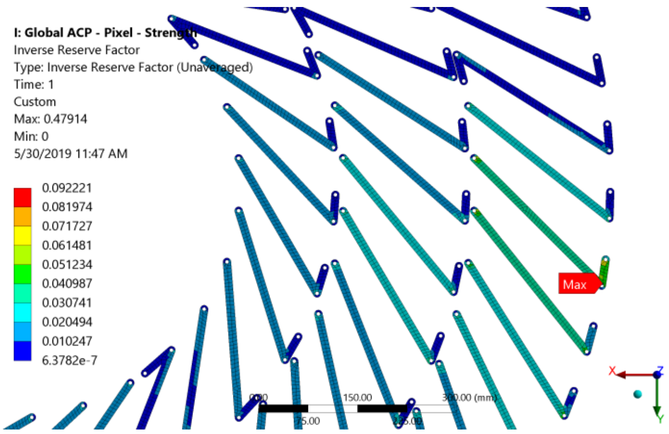

This document is uncontrolled when printed. Check the EDMS to verify that this is the correct version before use

Figure 87 IRF on some of the external components: Structural Bulkhead, OC mount pads, OC Flange, Strip Barrel interlinks.

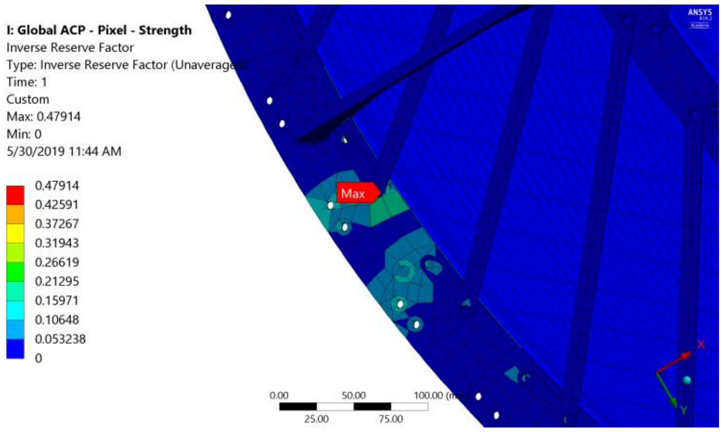

Figure 88 Detail of the most dangerous region in the ITk, the attachment between the strip barrel and the OC. The maximum value of the IRF in this region is 0.48.

An overview of the IRF contours on the whole ITk are shown in Figure 86. A selection of few of the parts carrying the most load is shown in Figure 87. The maximum IRF on the interlinks is equal to 0.1. This result may be optimistic as it assumes that the load will be distributed equally among all the interlinks. Results from a more conservative analysis are presented later.

The most strained region is shown finally in Figure 88. The maximum IRF is equal to 0.48 on the SB flange. It is important to notice that all these values are obtained with a mesh that is sufficiently refined for the stiffness computation, but that may underestimate the maximum strain around local geometry variations. As a consequence, a more detailed analysis of the most dangerous region was carried.

5.10.1 OC/SB Interface Local Analysis

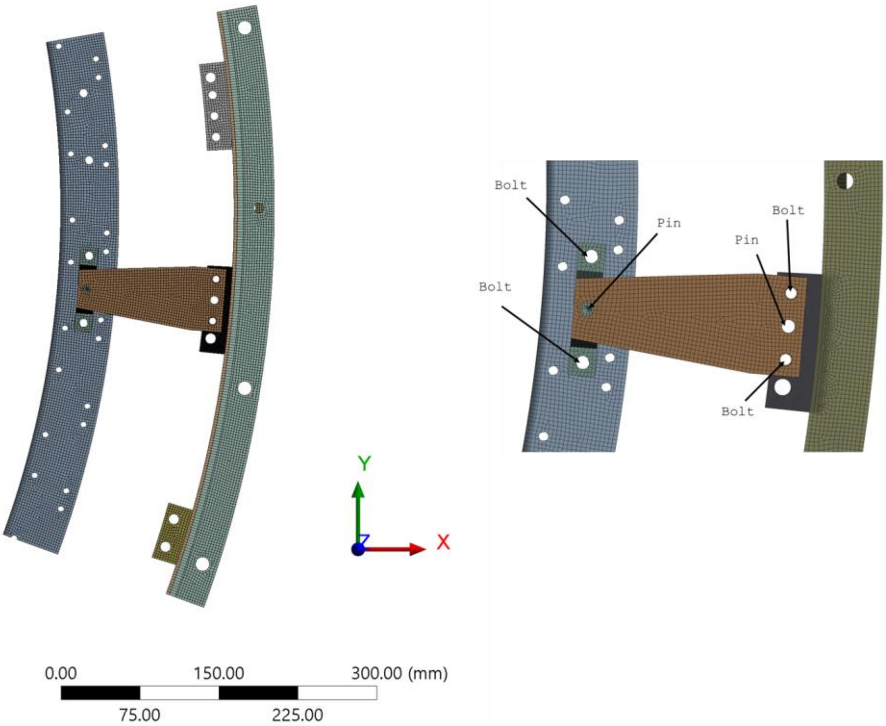

This document is uncontrolled when printed. Check the EDMS to verify that this is the correct version before use

Figure 89 FE mesh of the OC brackets region submodel (left), and a detail view of the bracket area with the connections specification (right). The interlinks were not modelled but introduced as displacement boundary conditions on the strip barrel flange.

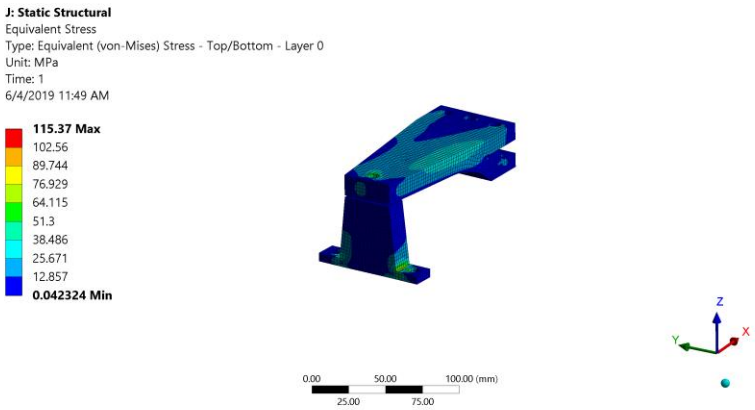

Figure 90 Equivalent stresses (Von Mises) on the bracket.

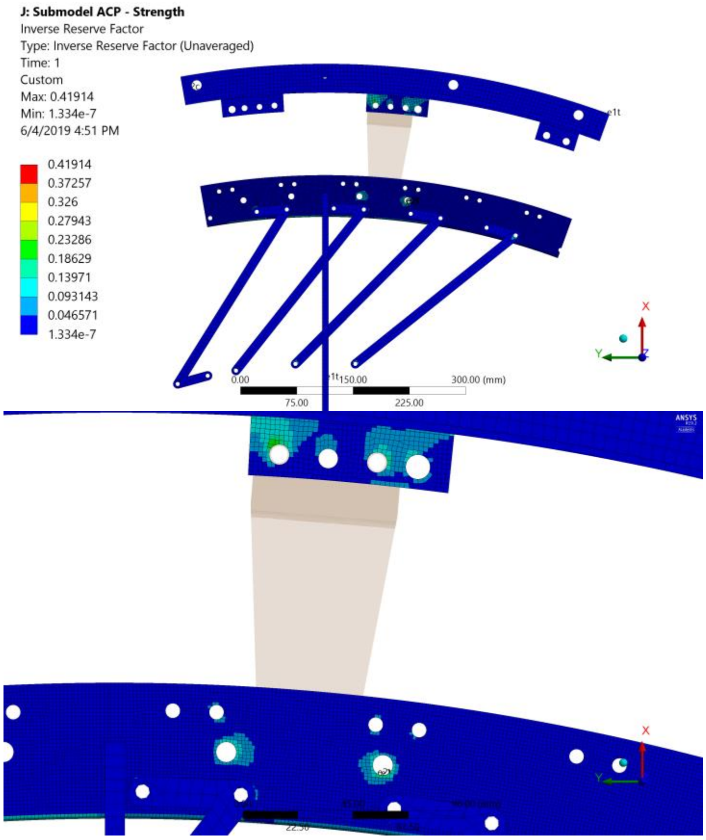

Figure 91 IRF contours on the OC and Strip Barrel flanges, overview (top) and zoom (bot).

A specialized model was produced in order to better analyse the behaviour of the interface region of the Strip Barrel and the Outer Cylinder, which was found to be the most stressed region. In particular, a submodel of this region was produced, using a finer mesh, and adding also the local bolted connections specifications via MPC links. The mesh is shown in Figure 89, along with the specifications used for the connections between the brackets components and the OC and Strip Barrel flanges.

The model was driven by displacements applied at the cut-boundary and extracted from the global FE model results. The case of reference is again the lifting case, with a vertical acceleration of 2g

This document is uncontrolled when printed. Check the EDMS to verify that this is the correct version before use

(Section 5.10.2). The interlinks were not modelled, but the forces exchanged with the flanges were introduced by means of local boundary conditions specifications at the hole edges, also extracted from the global model.

Results are shown in Figure 90, with a Von Mises equivalent stress contour on the bracket, and in Figure 91 with the IRF contours for the OC and Strip Barrel flanges. The results show that there is no real concern for the strength of the titanium brackets. Also, that the actual strains applied are not significantly greater than what was determined by the global model analysis. The maximum IRF for the most strained region, the strip barrel L3 flange, is equal to 0.42. This can be considered close (but lower) of a potential limit load – if we consider a safety factor equal to 2. It is however important to underline that, to further increase the confidence in these results, an experimental strength test for this particular region and load is planned.

5.10.2 Missing interlinks scenario

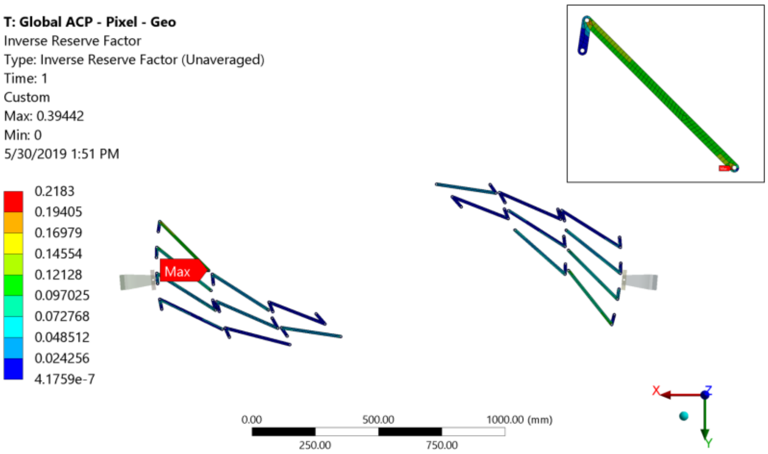

Figure 92 Missing interlinks scenario: the IRF is lower than 0.22.

A more stringent and catastrophic case was run to verify the actual performance of the system when the load is not distributed uniformly among the various interlinks. In particular, the experimental results from Section 4 suggest that, in particular in the radial direction, the load may be flowing only through a small number of interlinks. As shown in Figure 92, the lifting case was run suppressing most of the interlinks and keeping active only the ones in the horizontal plane. The choice of the interlinks left active is due to two reasons: first, these are the ones closer to the OC bracket, second, these are the ones most solicited in bending, which is a more dangerous condition for them. However, the model results, shown in Figure 92, suggest that the system would be safe enough even in this drastic scenario.

It is possible to quickly verify the load that the interlinks would be able to carry avoiding the first ply failure. For a longitudinal load the strain is simply:

$$\varepsilon = \frac{F}{EA}$$

And for the in-plane bending:

$$\varepsilon = \frac{M}{EI}\frac{h}{2}$$

It If we assume a modulus of 100 GPa, and a critical strain of 0.5%, and that the weight of the detector graving of the interlinks (~900 kg) is about symmetrically distributed on the two flanges and on the X+ and X- sides of the flanges, we find that to carry the load fully in bending we would

This document is uncontrolled when printed. Check the EDMS to verify that this is the correct version before use

need 25 interlinks per side, and longitudinally only 0.2. The fact that the interlinks are rotated even in the worst configuration considered above seems to explain why the load factors are so low.

5.11 Load Cases Analysis

To consider all the possible configurations that the detector will experience during assembly and life a load case table was produced. The document containing the table can be found here [10]. A global view is shown in Figure 93. The table lists on the rows (blue) all the components subsequently installed in the ITk, along with the various mechanical loads that the structure will experience during its life cycle. The columns (green) divide the different load cases, ordered where possible in order of time. Finally, the central region (yellow) allows to check which loads are enabled for each scenario.

In this document we do not discuss in detail all the load cases, but merely report the main results for some of them. The previous section provide in fact an in-depth discussion of the most relevant and dangerous cases.

This document is uncontrolled when printed. Check the EDMS to verify that this is the correct version before use

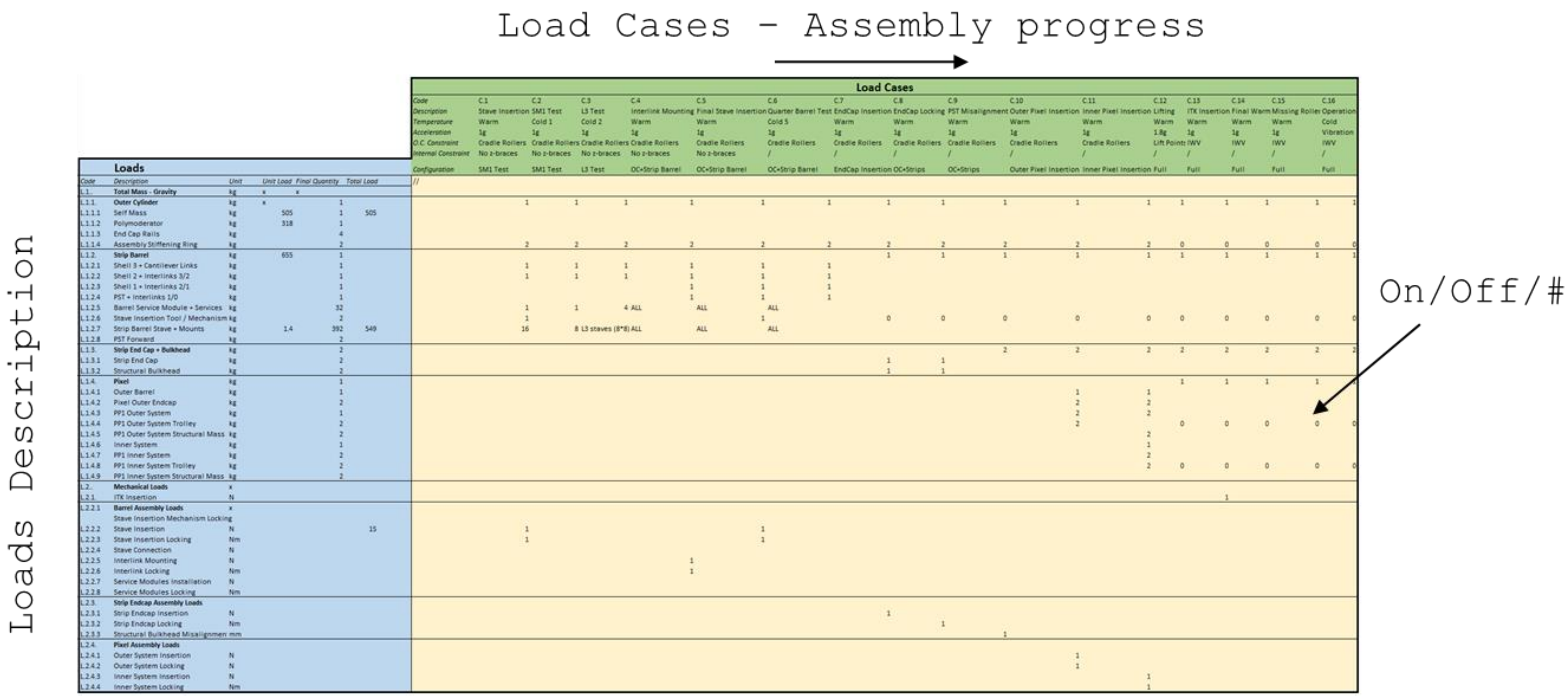

Figure 93 Load cases table overview. The table list all the loads and steps to which the ITk is subject during its assembly and life. The table shows then which loads are active for a particular configuration.

This document is uncontrolled when printed. Check the EDMS to verify that this is the correct version before use

6 PRODUCTION MODEL UPDATE

The model presented in the previous section was subject to a number of changes mostly aimed at improving and facilitating the production and assembly of the detector. In this section we report the main changes, along with the analysis showing the impact of the change on the mechanical performance of the structure. For simplicity, the design presented in Section 5 is referred to as FDR design, as it is the one that was approved by the reviewer at the Final Design Review.

6.1 Hat Stiffeners Simplification and Number Reduction

The FDR design foresaw two different typologies of hat stiffeners depending on the necessity to accommodate or not the mount pads. These stiffeners are then split in 4 pieces for easiness of production. This would have resulted in the realization of three different geometries for the various hat stiffeners pieces, and as a consequence the production of three moulds. To simplify the design and reduce the overall cost the hat stiffeners were made of a single part, always repeated independently to the location. The resulting design is shown in Figure 94. FE results showed that this variation of the geometry does not impact the overall stiffness of the system.

Another reduction in cost was achieved reducing the total number of stiffeners. Figure 95 (bottom) shows that all the hat stiffeners not attached to mount pads were removed. The only one left was the one at z=0, in order to limit the shape change of the shell in this region. The impact of the hat stiffener reduction and geometry variation is shown in Figure 95: the total gravity sag variation is in the order of few microns.

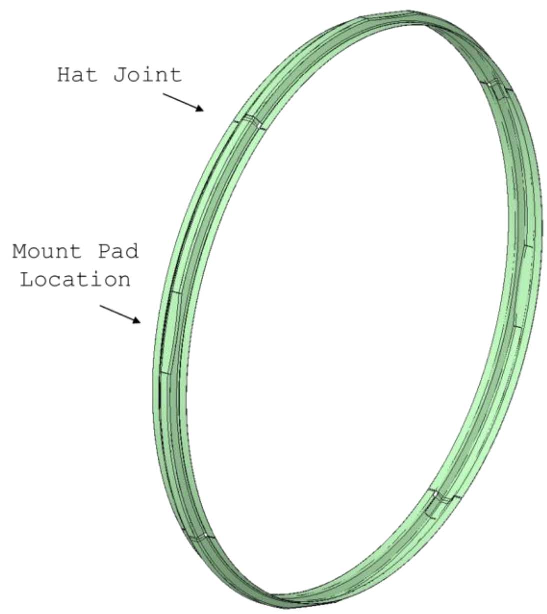

Figure 94 Hat stiffener design simplification.

This document is uncontrolled when printed. Check the EDMS to verify that this is the correct version before use

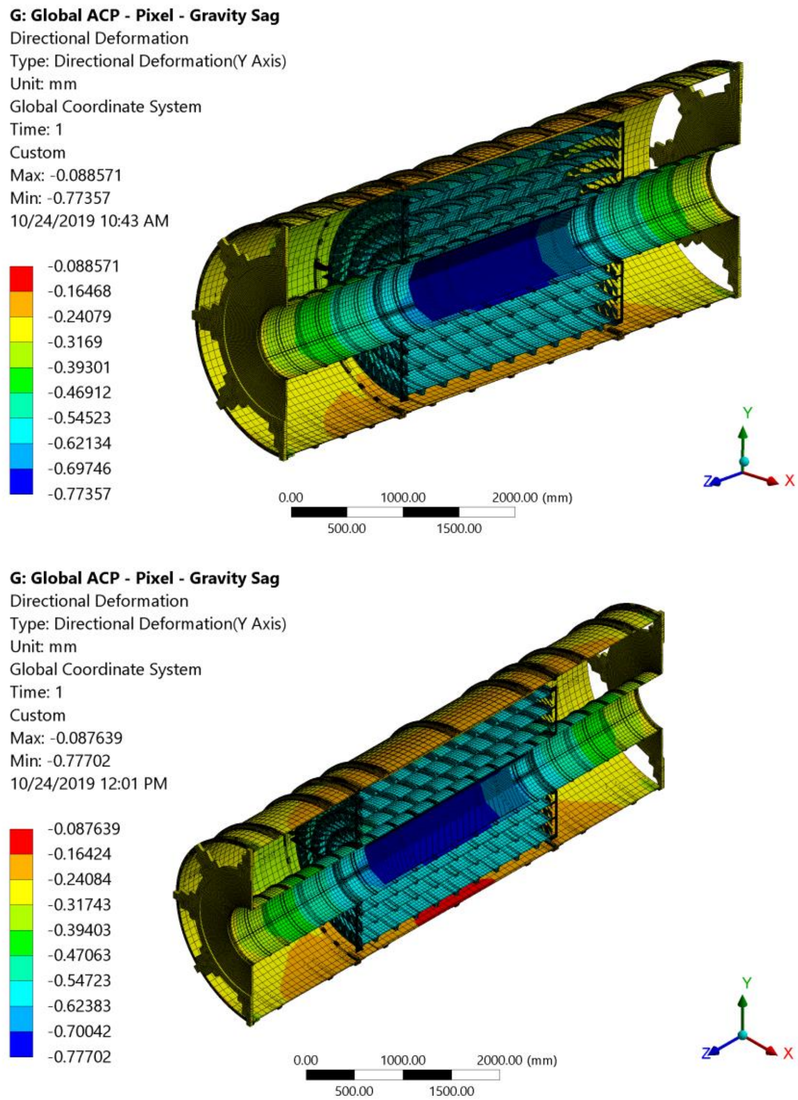

Figure 95 Gravity sag of the integrated model: (top) FDR design; (bottom) new design.

This document is uncontrolled when printed. Check the EDMS to verify that this is the correct version before use

6.2 Flange Geometry Variation

The OC flanges used to connect the OC barrel region to the OC forwards had, in the FDR design, a set of protrusions apt to support the strip barrel brackets and the strip barrel modules. The protrusion was only present on the barrel side of the flanges. In the new design, the barrel and forward flanges are now symmetric, and the supports for the brackets and modules are instead introduced by an auxiliary ring. This design is shown in Figure 96: the ring is connected to the two flanges by a series of bolts.

With this design variation, the mass load is now introduced on the floating ring that is held in place by the friction resulting from the two flanges. A dedicated model was created to verify that the bolt preload will avoid any sliding of the flanges. In particular, to verify that no sliding is allowed when the load is introduced. The FE model used to study this system is shown in Figure 96. Only half of the flange subsystem is represented due to the problem symmetry. The simulation is performed in two steps: in the first step the bolt preload is applied. In the second step, the bolts are locked and the load resultants are applied to the OC bracket supports. These loads were extracted from the lifting simulation performed with the integrated model.

The resulting contact condition in the flanges is shown in Figure 97, left. The sliding at the maximum load is shown on the right. Using the M8 bolts specified, the sliding is contained within 3 µm at the worst point. The model was also tested with M4 and M12 bolts. The sliding in these case is respectively 6 µm and 2 µm (see Figure 98).

The sliding in the support region could be completely removed by inserting a hole closer to the supporting region. However, this is not possible because that space is already occupied by the mount pads.

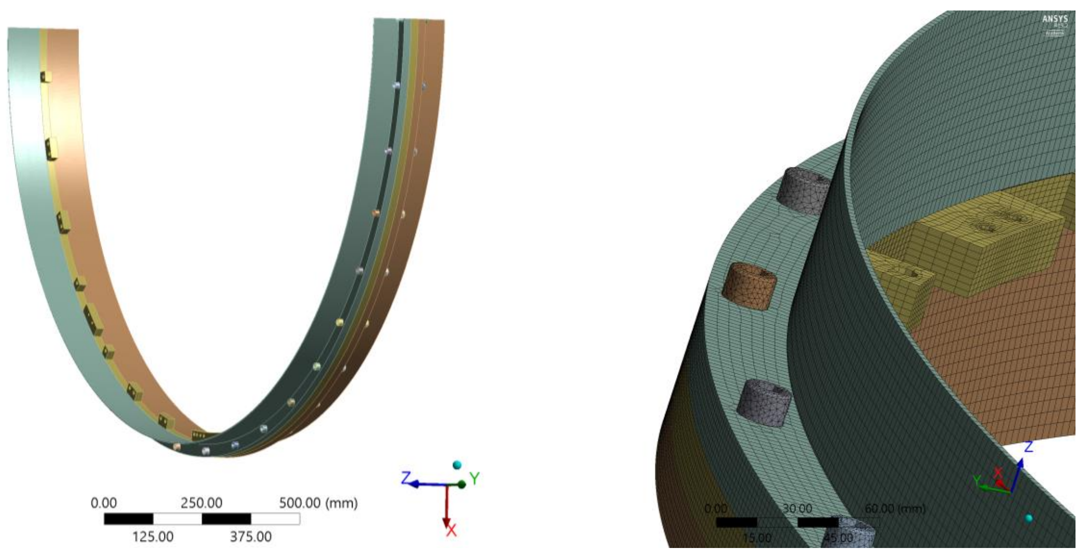

Figure 96 Geometry (left) and mesh detail (right) of the FE model of the OC flange subassembly.

This document is uncontrolled when printed. Check the EDMS to verify that this is the correct version before use

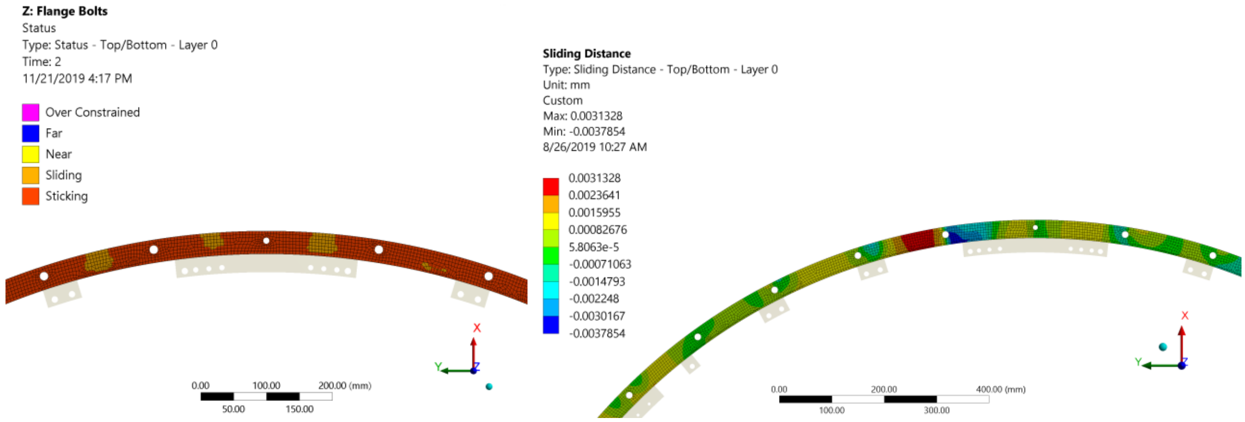

Figure 97 Left: contact status of the flange subassembly during lifting. Right: Sliding at the contact elements on the support module. The sliding is less than 3 µm everywhere.

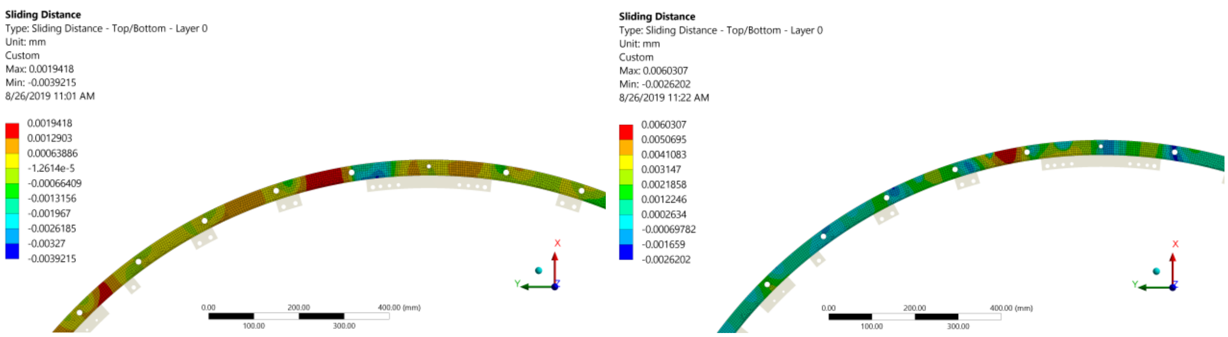

Figure 98 Sliding results for 4 mm (left) and 12 mm (right) bolts.

6.3 OC/SB Brackets

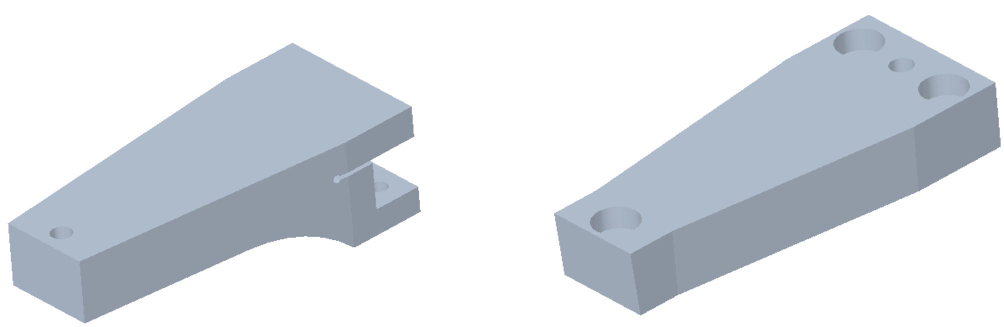

Figure 99 Bracket design variation: the clamp configuration was removed and the OC bracket thickness was reduced.

The bracket design was subject to a number of iterations. The main driver for these iterations was the need to create further space for the strip barrel services. The main difference between the FDR design

This document is uncontrolled when printed. Check the EDMS to verify that this is the correct version before use

and the new is the removal of the clamping geometry. Figure 99 shows the original design and the new updated design.

6.3.1 *Bracket thickness*

A parametric analysis studying the impact of the bracket thickness on the gravity sag was performed. The following values were considered: 12 mm, 16 mm and 24 mm. The overall computed increase of the gravity sag at the pixel beam is equal to 7% when going from 12 mm to 24 mm. The middle case was picked. The gravity sag for this design is shown in Figure 95 and well within the limit of 1 mm.

Going from a double clamp to a single clamp configuration reduces the overall bending stiffness of the bracket. This corresponds to an 8% increase of the vertical deflection of the detector (8 μm). If required, this decrease in stiffness might be solved by increasing the thickness of the mount pads. However, as the estimated performances are well within the requirements, this was not considered necessary.

6.3.2 *Impact of the clamp configuration*

On the other hand, the removal of the clamp configuration decreases the overall solidity of the joint between the bracket and the outer cylinder support ring. To verify that the connection performs as intended, a detailed model of the connection area was created. The geometry of this model is shown in Figure 100: the symmetry of the problem was exploited and only half of the flange was modelled. The bracket was connected to the support ring with two bolts and a pin. The flanges were glued together and frictional contacts were applied between all the other parts. The bracket stand-off was modelled with a beam element. A spring was added to introduce the stiffness of the strip barrel. The spring stiffness was computed applying a unit displacement to the 4 bracket holding regions of the barrel, as shown in Figure 101. The force required to deform the SB of 1 mm per side is equal to 11.975 kN.

The simulation is run in two steps: in the first one the preload is applied to the bolts, in the second one a vertical displacement was applied to the ends of the spring representing the strip barrel (see Figure 100, left). The total reaction was used then to compute the amount of force required to cause this displacement. Obviously, applying a force would produce the same effects in reality. However, 'controlling' in displacement the model allows to easily reach the numerical convergence.

For simplicity, it was assumed that each bracket is carrying a quarter of the strip barrel weigth and the portion of the pixel weight not carried by the forwards, equal to 238 kg. This is conservative, as part of this load will be flow to the structural bulkheads and transferred via the corresponding mount-pads. Considering the lifting acceleration (2g), this means that the total force on each bracket is equal to 4670 N.

This document is uncontrolled when printed. Check the EDMS to verify that this is the correct version before use

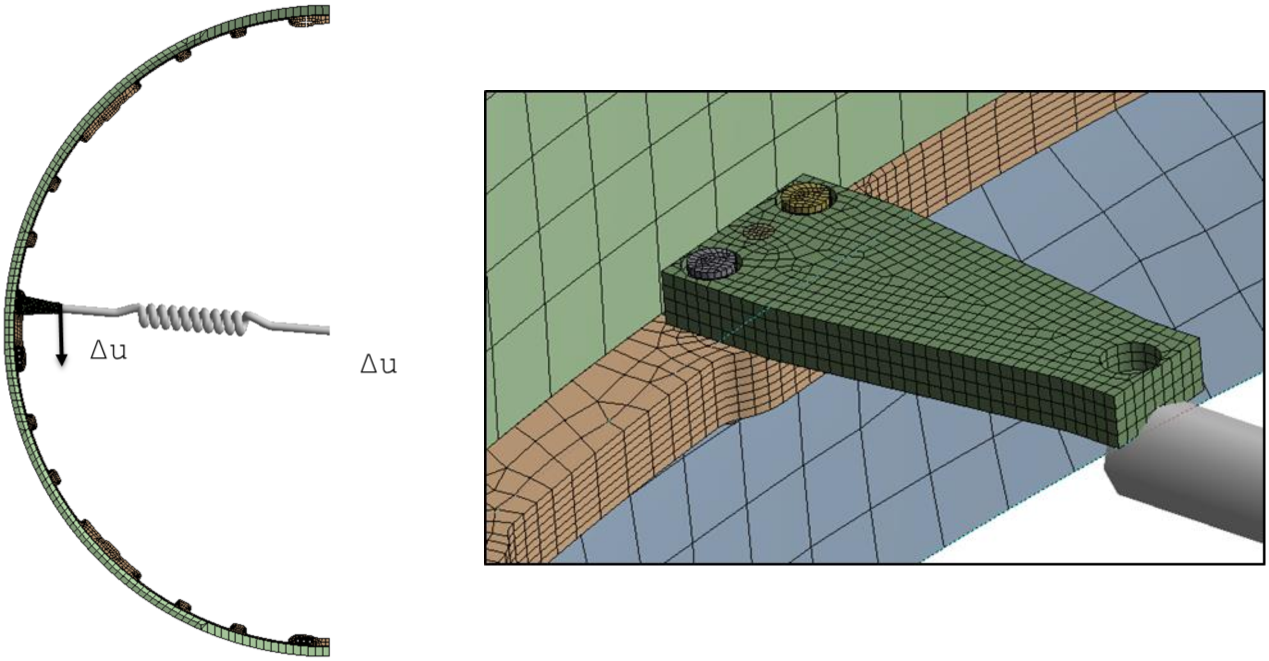

Figure 100 Bracket/Flange subsystem FE model geometry and mesh detail.

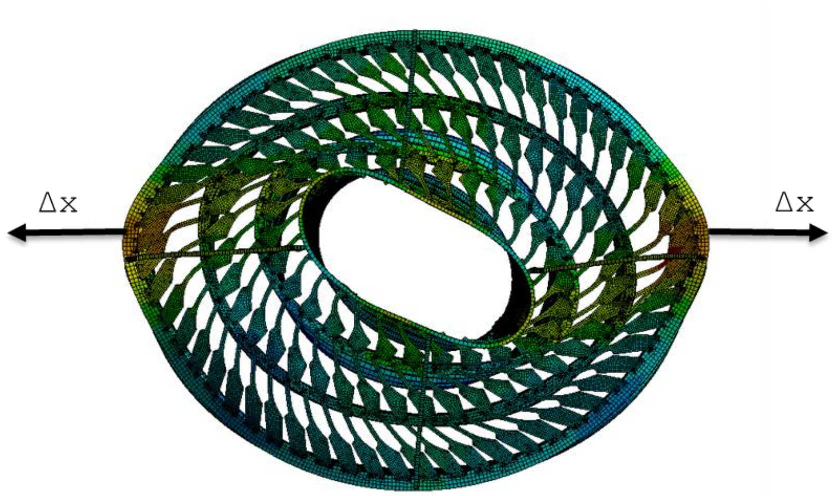

Figure 101 Strip barrel stiffness estimation for the bracket/flange subsystem model.

The analysis was performed with a conservative friction coefficient between the flanges and the bracket of 0.1. In this very conservative scenario, the FE analysis shows that the bracket starts to slide until the bolt start touching the bracket wall. The vertical sliding can be computed taking into account the available radial gap and the geometry of the bracket. With reference to Figure 103 (right), we can write:

$$dy = dr_b R_1/R_2$$

This document is uncontrolled when printed. Check the EDMS to verify that this is the correct version before use

In our case, this corresponds to a vertical displacement of 1.3 mm. This is not affecting stability, as the forces acting are orders of magnitude smaller and cannot provoke this sliding, but only a small motion during lifting.

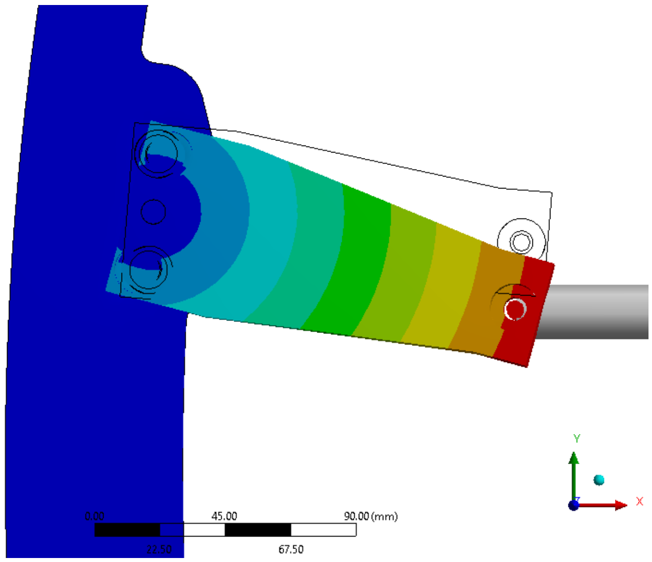

Figure 102 Displacement at the bracket (magnified) during the sliding.

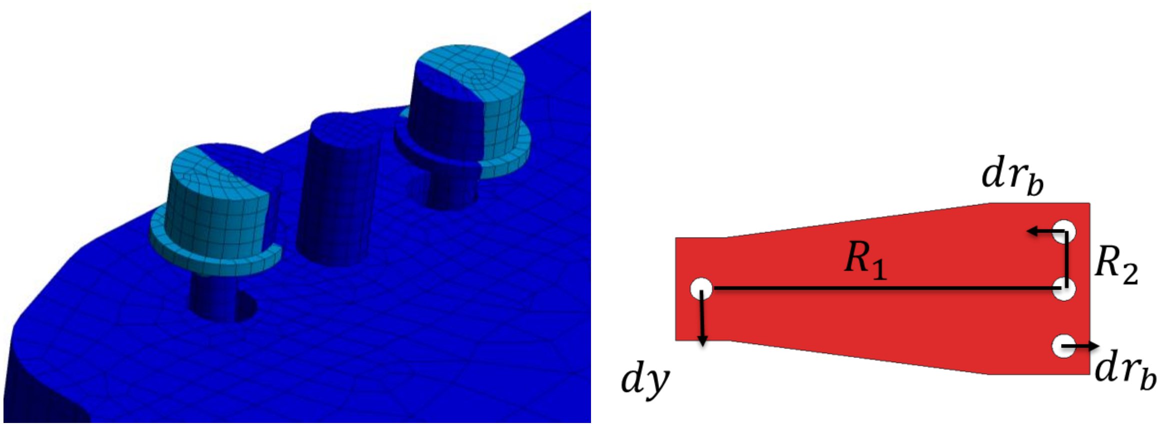

Figure 103 (Left) Deformation of the bolts in case of sliding at the bracket/flange interface. For visualization purposes. The bolts here are smaller than in the real case to magnify this effect. (Right) Deformation direction during the bracket sliding.

This document is uncontrolled when printed. Check the EDMS to verify that this is the correct version before use

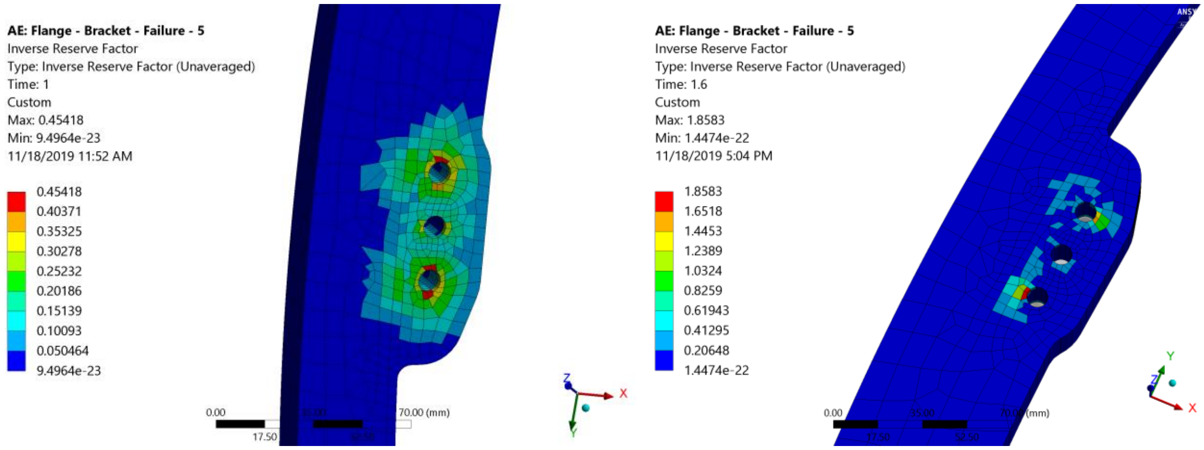

Figure 104 IRF at the flange after bolting (left) and during lifting (right).

Even if this sliding event is not likely, the various parts have to be able to withstand the corresponding loads. As the bolt starts to touch the flange, these see a significant increase of the applied strain. The resulting IRF is shown in Figure 104, along with the status after bolting. The value above 1 means that the flange might fail in this scenario.

6.3.3 Design improvement

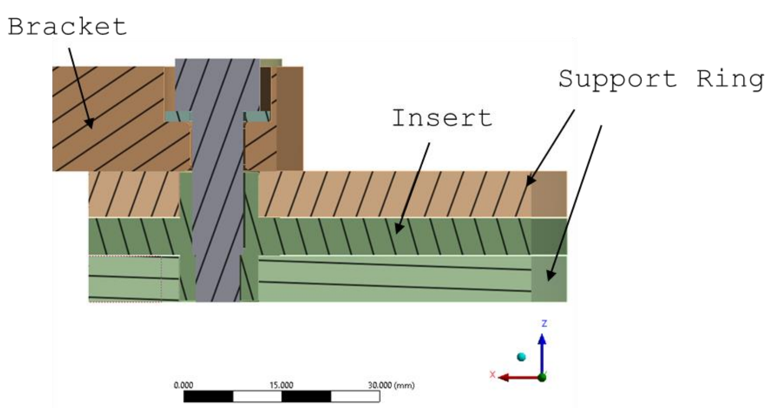

Figure 105 Cross section of the new bracket/support ring design.

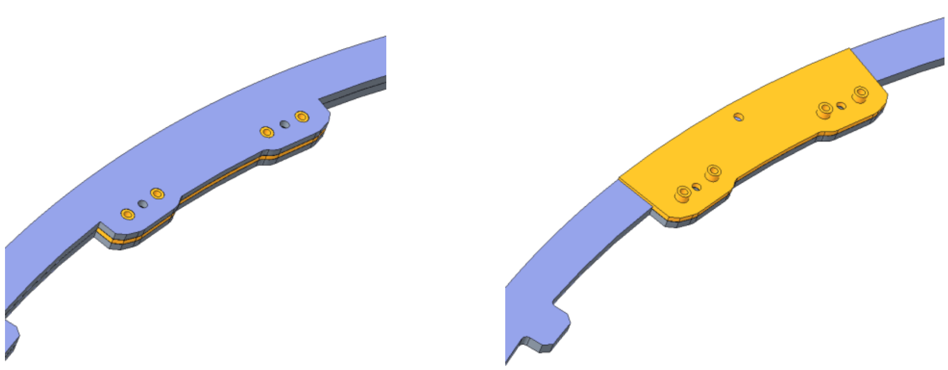

Figure 106 Support ring and insert assembly (left), and same assembly with top part of the ring hidden (right).

This document is uncontrolled when printed. Check the EDMS to verify that this is the correct version before use

The support ring design was then improved adding a Titanium insert. The new design is shown in Figure 105 and Figure 106. With this new configuration, the eventual motion of the bolt would bring it in touch with the bracket or the insert. This is expected to reduce significantly the high strains on the support ring CFRP.

This new configuration was studied in a model similar to the one described in the previous section. The resulting IRF is shown in Figure 107: the increase during the lifting operation is very small, equal to 0.06. This configuration might also produce severe loads in the Titanium parts, verified with an elasto-plastic analysis. The total strain on these components is shown in Figure 108. No plastic strain was detected in the model results. The system will be further validated with prototypes to ensure that it can carry the design load.

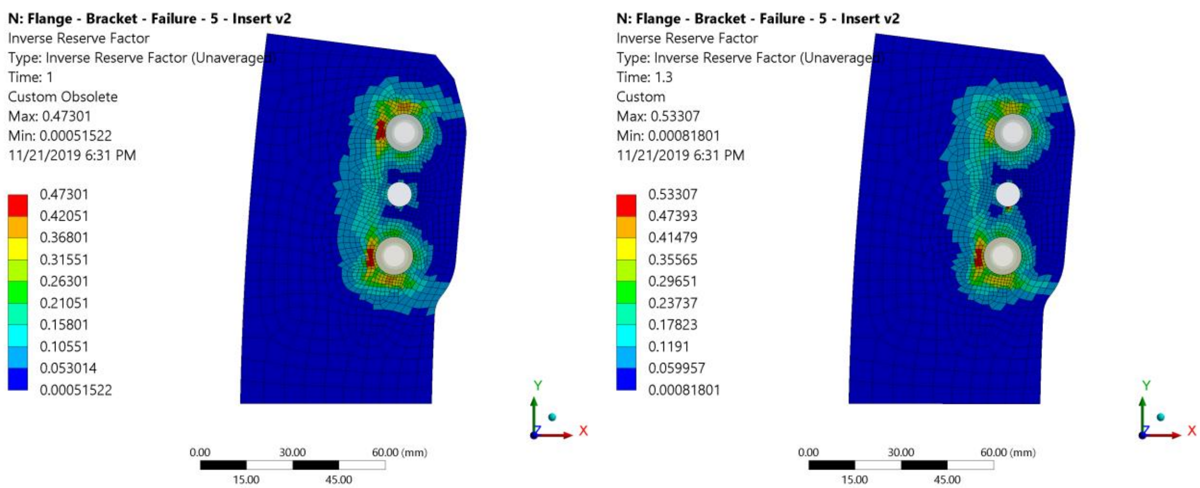

Figure 107 IRF at the support ring after bolting (left) and during lifting (right). The increase due to the lifting operation is negligible.

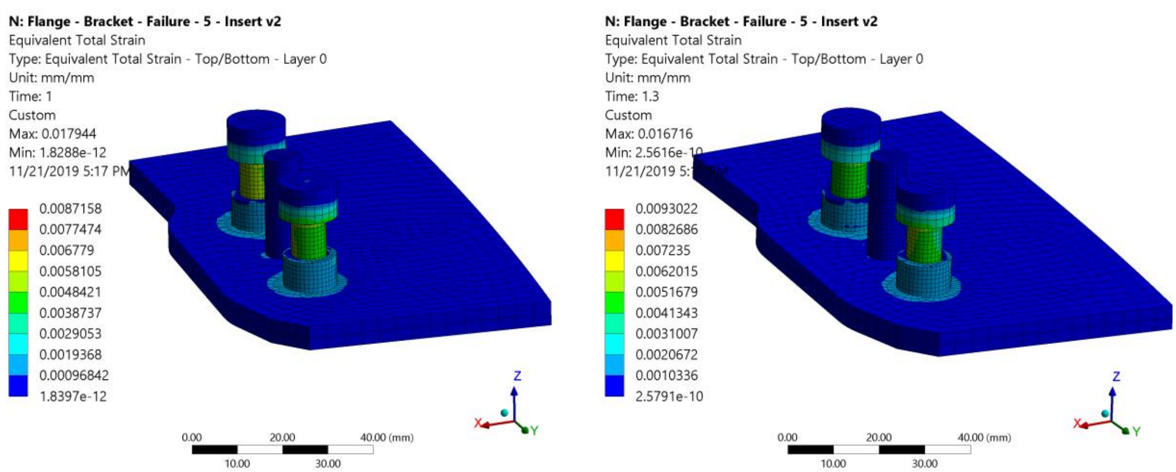

Figure 108 Total strain at the bolts and insert. No plasticization was detected on the various components.

This document is uncontrolled when printed. Check the EDMS to verify that this is the correct version before use

6.3.4 Back-up solution

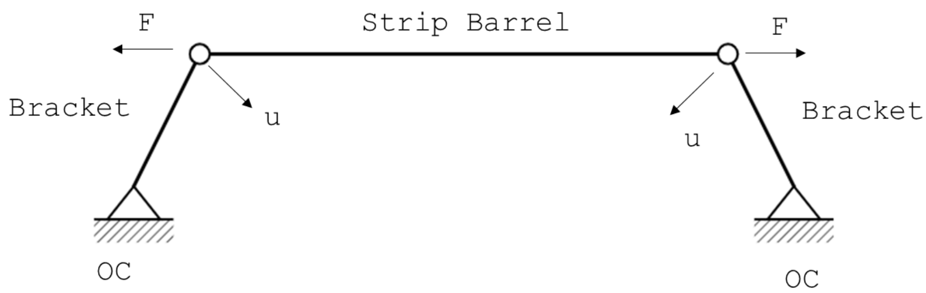

Figure 109 Simplified representation of the Strip Barrel / OC system.

This sliding configuration could be in principle avoided by exploiting more the fact that the OC/SB connection creates a degenerate quadrilateral that, if the strip is assumed to be rigid, should not be able to move. This configuration is schematized in Figure 109: the potential rotational motion u of the bracket around the pin connecting it to the OC (hinge in the drawing) is counteracted by the force required to compress the strip barrel. However, as the SB support points are almost in line with the OC ones, the deformations of the bracket attempt to create a force that is almost only horizontal. In this case the assumption that the strip barrel is very rigid is not valid anymore. This is closer to the case of the present design, where either the friction or an additional pin (or the contact of the bolts with the bracket/flanges) is required to generate a torque opposing to this rotation.

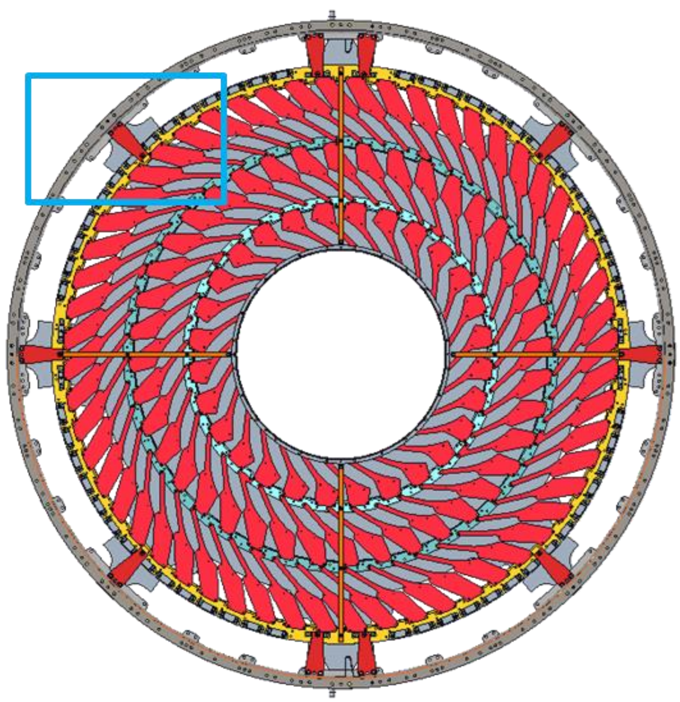

Figure 110 Alternative location for the OC/SB brackets.

This document is uncontrolled when printed. Check the EDMS to verify that this is the correct version before use

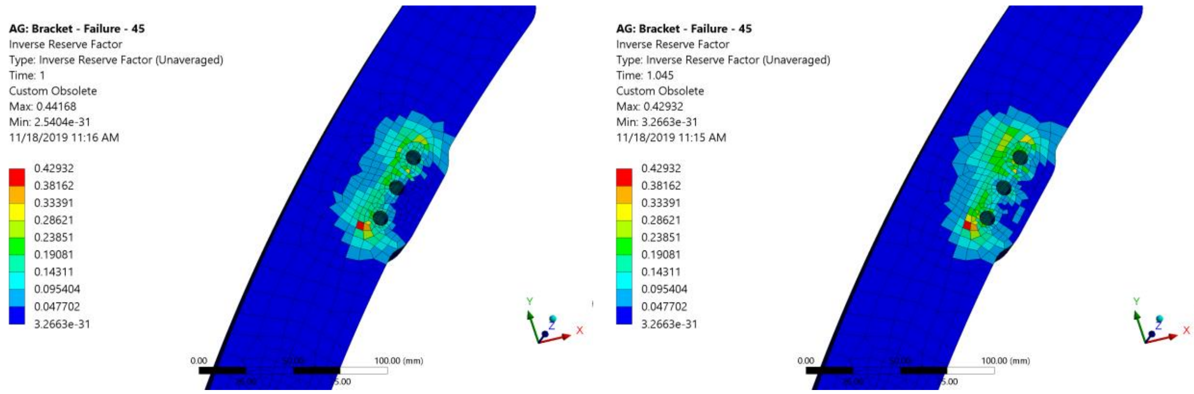

Figure 111 IRF factor at the flanges during bolting (left) and lifting (right) for the alternate configuration.

It is possible to get rid of this issue by moving the location of the brackets of 45°, as shown in Figure 110. In this case the approximation of a very rigid strip of Figure 109 is much closer to reality. In this scenario the pin is expected to carry all the force and no contact between the bolts and the flange can be expected.

This configuration was again tested with the same modeling strategy of the previous paragraph. The resulting IRF is shown in Figure 111: during the lifting operations there is no increase of the strains in the flanges in the regions surrounding the bolts. As expected, a small increase is instead present around the pin. This is not critical, as in this case we can guarantee that the force will be distributed uniformly across the whole flange/pin interface (cylindrical surfaces).

The gravity sag obtained by moving the brackets is shown in Figure 112: this is about 0.1 mm larger than the one expected with the bracket at 5°. A similar reduction in stiffness is found with the modal analysis. The fundamental frequencies reported in Table 9: the longitudinal and horizontal frequencies are not affected. There is a reduction of 2 Hz of the gravity sag mode. It is worth to notice, however, that the current design provides a wide margin for mechanical stability, and that this increase cannot bring the short term stability over the requirements.

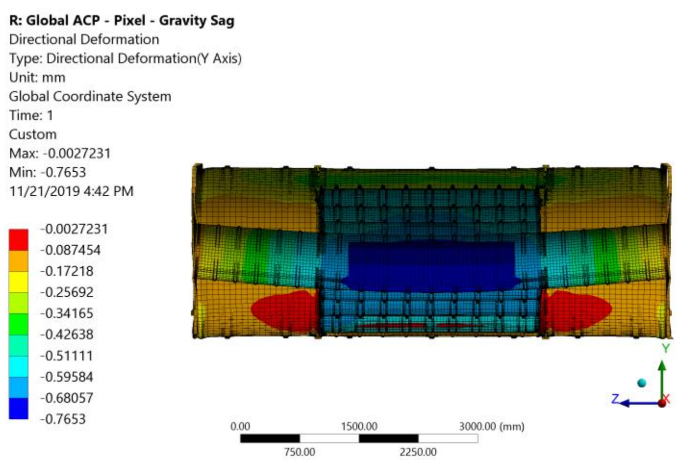

Figure 112 Gravity sag for the alternate configuration. The overall deflection increases of about 0.1 mm, but is still within the requirements.

This document is uncontrolled when printed. Check the EDMS to verify that this is the correct version before use

Table 9 Fundamental frequencies comparison varying the OC/SB bracket position.

Mode	Frequency	
	Flange 5°	*Flange 45°*
	Hz	*Hz*
I	5.8	5.8
II	11.0	10.9
III	14.5	14.7
IV	19.9	19.3
V	22.4	20.4
VI	23.0	23.2

6.4 Updated results and performance

The following paragraphs provide the results from the main integrated model computations performed as explained in Section 5. The summary of the results is provided by Table 11 in Section 7.3.

6.4.1 Gravity sag

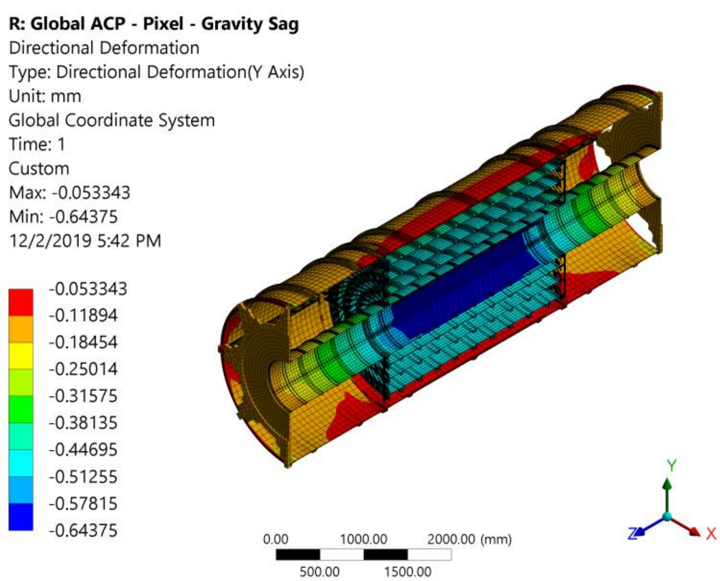

Figure 113 Gravity sag of the integrated model.

The vertical deflection of the structure is now 0.643 mm. This is lower than the performance achieved by the previous FDR design. The increase is mostly due to the increase of the mount pad thickness and the increased surface area of the interlinks.

This document is uncontrolled when printed. Check the EDMS to verify that this is the correct version before use

6.4.2 Thermal stability

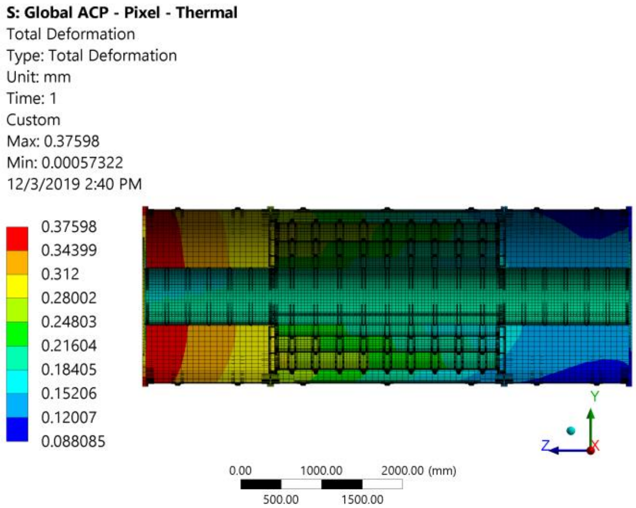

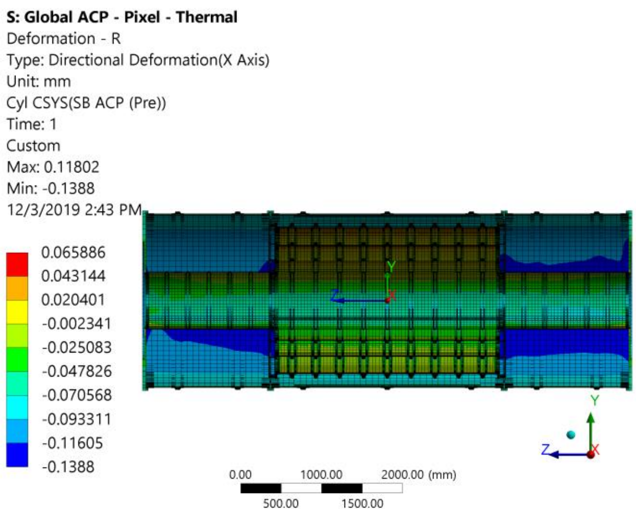

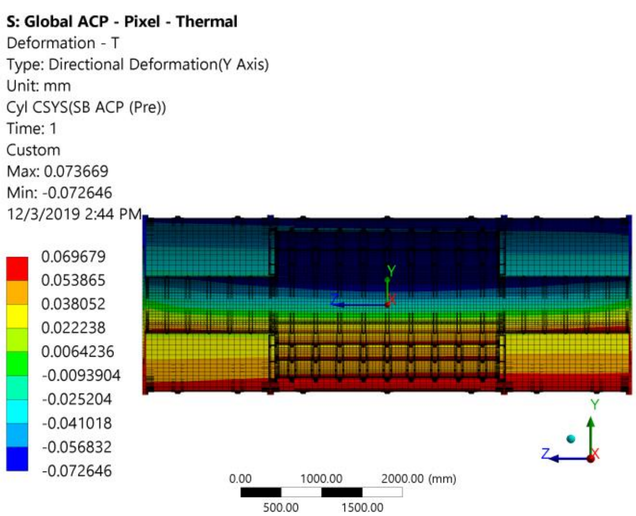

This document is uncontrolled when printed. Check the EDMS to verify that this is the correct version before use

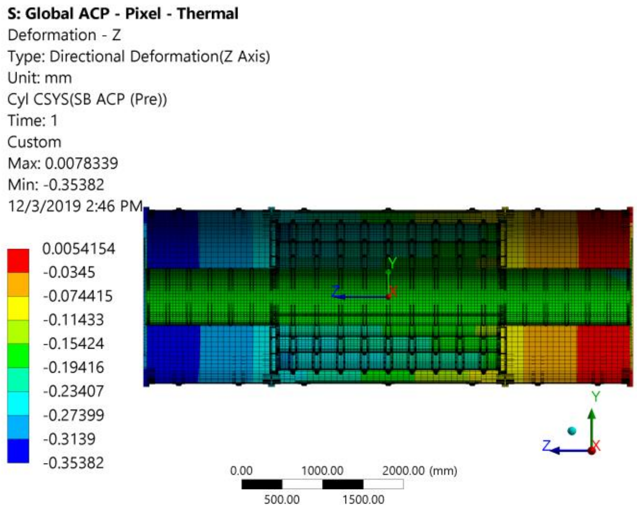

Figure 114 Thermal deformation from 20 °C to -40 °C. The contours show the following deformations (from top to bottom): total, radial, azimuthal, longitudinal.

The deformation of the system is shown in Figure 114. The maximum total displacement is equal to 0.38 mm, lower than the one for the FDR design. The radial displacement at the worst point is 138 µm. The azimuthal displacement is 73 µm, the longitudinal one 353 µm. Scaling to variations of ±1 °C we obtain: ±2.3 µm, ±1.2 µm and ±5.9 µm. For temperature variations of ±3 °C we obtain: ±6.9 µm, ±3.65 µm and ±17.7 µm.

This document is uncontrolled when printed. Check the EDMS to verify that this is the correct version before use

6.4.3 Moisture effects

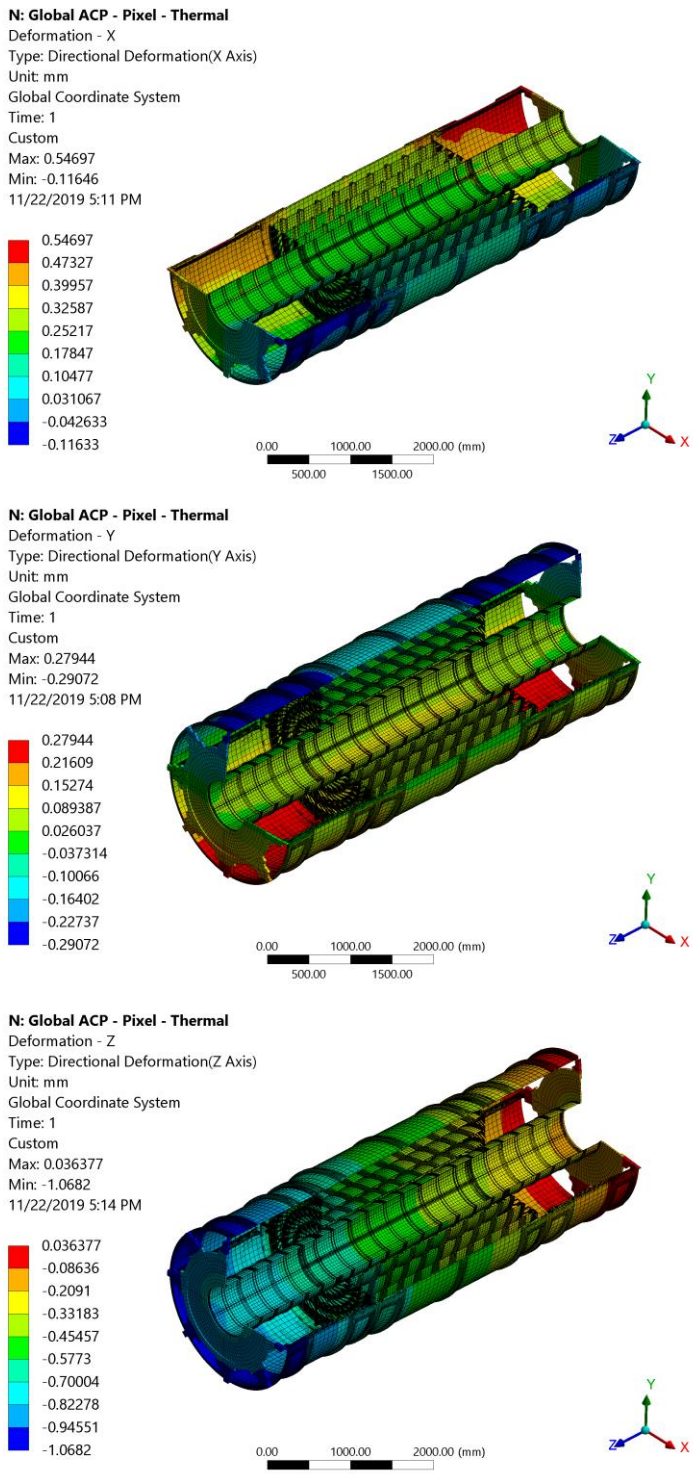

Figure 115 Deformations with a 1% humidity variation. From top to bottom: horizontal (X), vertical (Y), longitudinal (Z). The results can be scaled linearly to the desired humidity variation.

This document is uncontrolled when printed. Check the EDMS to verify that this is the correct version before use

The computed deformations due to a 100% moisture variation are shown in Figure 115. The total variation in the X, Y and Z direction are equal to 0.55 mm, 0.29 mm and 1.0 mm. This is slightly better than what obtained from the FDR model. The expected deformation can be scaled to a more reasonable moisture variation of 0.65%, resulting in 0.36 mm, 0.19 mm and 0.65 mm in the X, Y and Z direction respectively. For reference, with the FDR model this was instead 0.36 mm, 0.21 mm and 0.90 mm.

6.4.4 Modal analysis

The updated modal shapes are provided in Figure 116, along with the new fundamental frequencies. The model performs similarly to the FDR one. A detailed comparison is provided in Table 10. There is a slight decrease of the performances in the z direction, considered less important than the ones in the r-phi plane. This decreased the fundamental frequency of the 1st mode and of the 4th mode, now 2nd. The stiffer mount pad increases the horizontal performance, with the two corresponding modes fundamental frequency increasing of about 4 Hz. Also the 'gravity sag' vertical mode is increased of about 3 Hz, as the mixed one.

Table 10 Comparison of the fundamental frequencies of the FDR and updated (PRR) design.

Mode	FDR		PRR	
	Type	Freq.	Type	Freq.
		Hz		*Hz*
I	*Telescope*	6.8	*Telescoping*	5.8
II	*Horizontal*	10.9	*Telescoping*	11
III	*Horizontal*	14	*Horizontal*	14.5
IV	*Telescope*	17.1	*Horizontal*	19.9
V	*Gravity sag*	20.2	*Mixed*	22.4
VI	*Mixed*	20.6	*Gravity sag*	23

This document is uncontrolled when printed. Check the EDMS to verify that this is the correct version before use

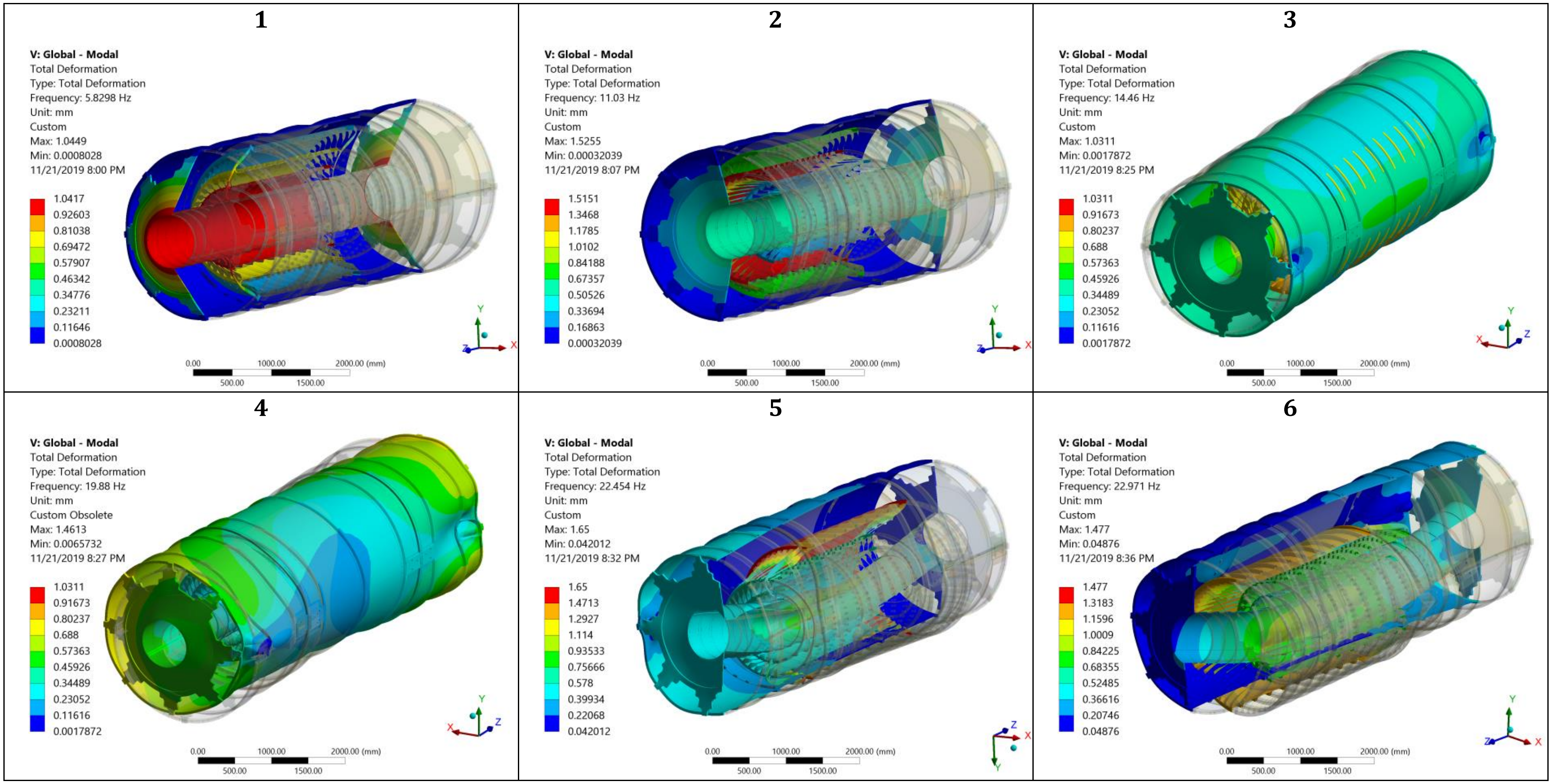

Figure 116 Modal shapes of the updated model.

This document is uncontrolled when printed. Check the EDMS to verify that this is the correct version before use

6.4.5 Random vibration

The random vibration analysis was performed from a starting pool of 12 modes. The last mode frequency considered in this modal analysis is equal to 38 Hz. The higher stiffness of the system improved significantly the mechanical stability.

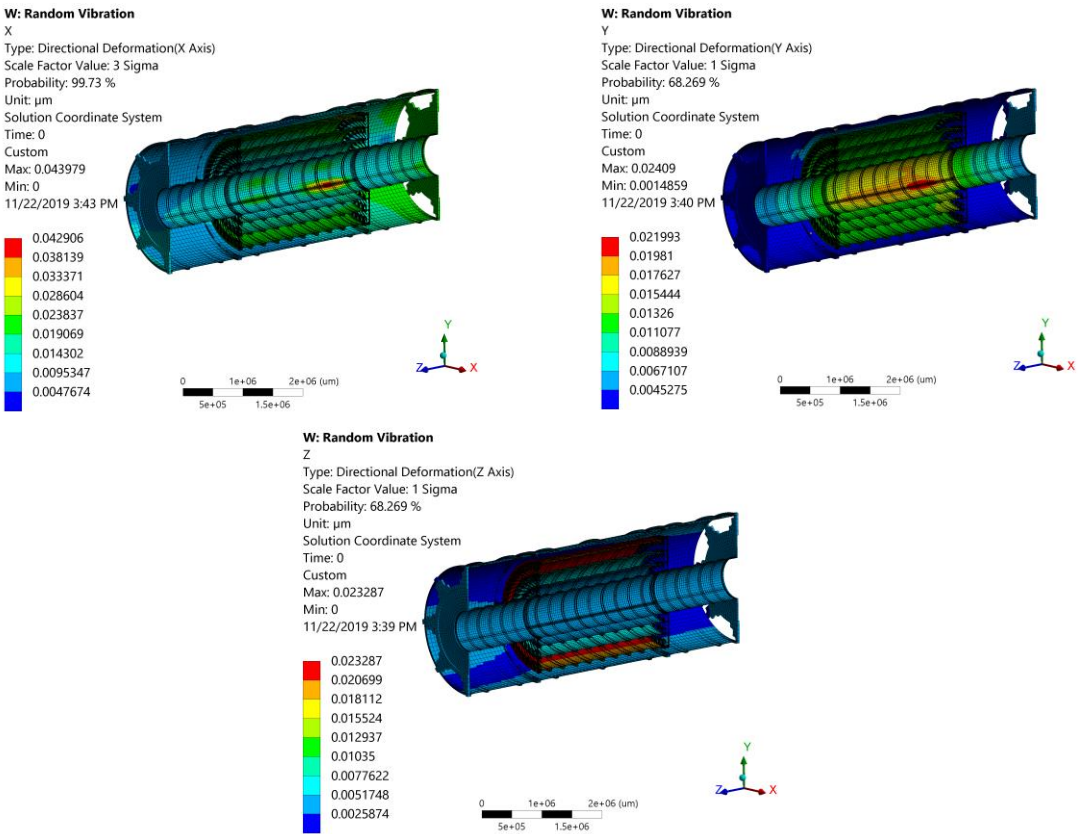

Figure 117 Random vibration response (measured in µm) of the integrated model in the X (top left), Y (top right), and Z (bot) directions. The response is lower than 1 µm in all directions.

6.4.6 Strength

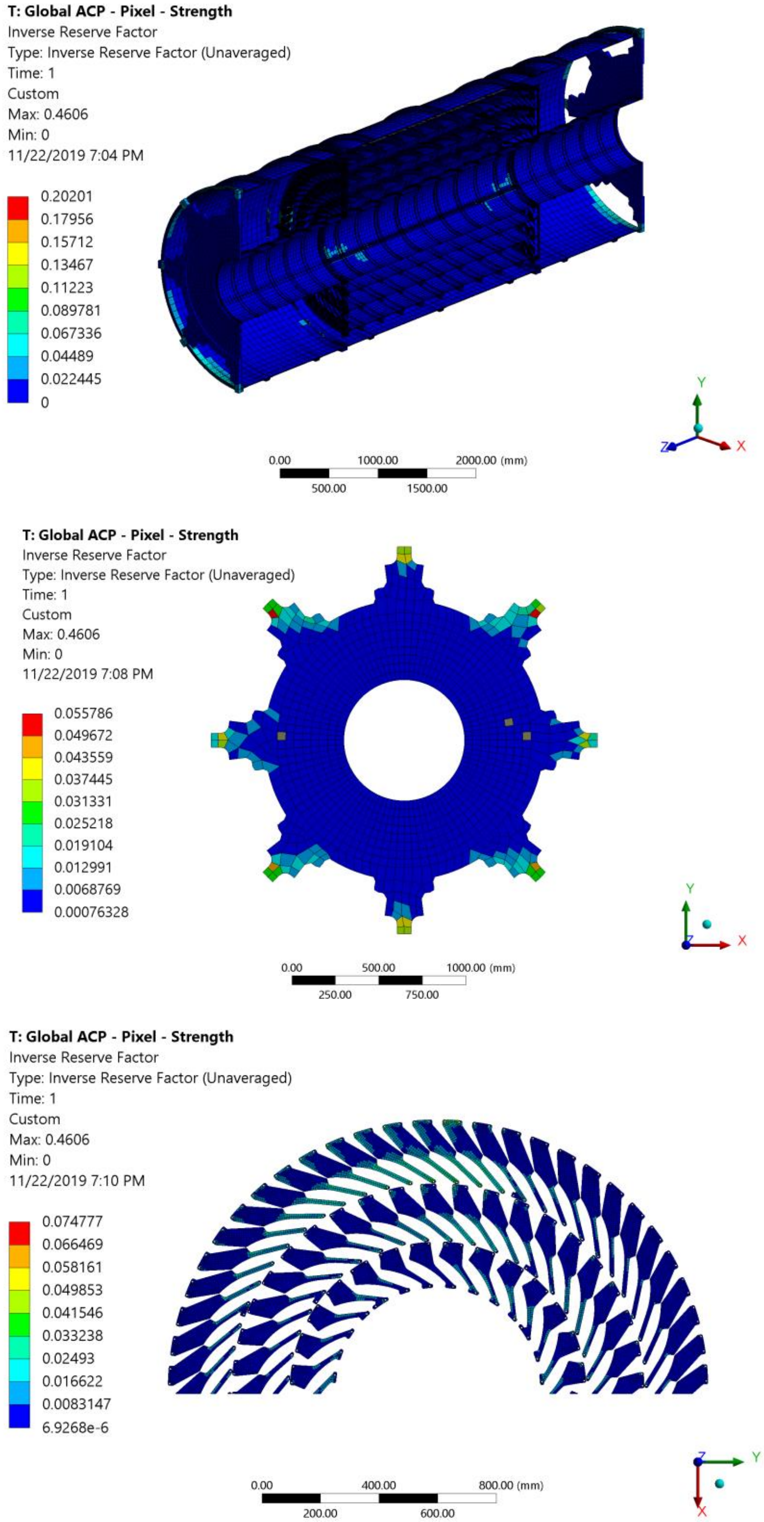

Figure 118 IRF from the integrated model analysis. From top to bottom: all, structural bulkhead, interlinks. More detailed analysis are provided for other components.

This document is uncontrolled when printed. Check the EDMS to verify that this is the correct version before use

The IRF values from the global model are shown in Figure 118. The overall values are significantly lower than in the FDR model thanks to the increase of stiffness of the mount pad. The interlinks are also less strained, and their IRF is lower than before. This is due to their significant size increase: the previous modelling strategy was conservative and tried to use a minimal profile for the interlinks to be sure that the deformation and strains would always be contained within the requirements. The flange/bracket strains are not presented here as they were studied with a dedicated model in the previous subsection.

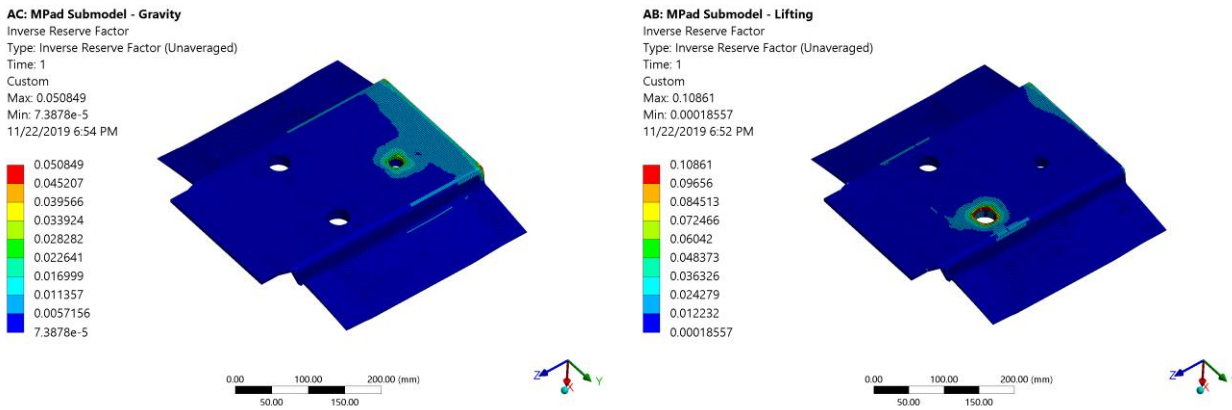

Figure 119 IRF on the mount pad submodel in the IWV (left) and during lifting (left).

The mount pad assembly stiffness is the main driver of the stability performances of the detector. An increase of thickness of this component comes to a relatively low cost in material (compared for example to an increase of the shell thickness). It was then decided to maximize the thickness using all the space available. The maximum thickness of the mount pad is now equal to 20 mm.

A detailed analysis of the mount pad region was performed, applying at the boundaries the displacement during lifting and when the detector is installed. The analysis result, showed in Figure 119, suggest that in both cases the strength of the mount pad is higher than required. The maximum value of the IRF is in fact equal to 0.1 during lifting.

This document is uncontrolled when printed. Check the EDMS to verify that this is the correct version before use

7 RESULT SUMMARY AND ACTION ITEMS

7.1 Action Items

The action items from the FDR, relevant for this document, are listed here. The list provides also a reference to the document/section where the action is treated in detail. The action items are extracted from the Report of the Final Design Review of the ATLAS ITk Common and Strip Global Structures, available here [11]. To help the reader, the reviewers' recommendations and actions are marked in *italic*, the action (**A**) or recommendation (**R**) number in **bold**, and the answers in normal.

7.1.1 Outer Cylinder

FDR1. *Optimize the OC geometry and design, in order to increase the envelope (…)*

The OC radius was increased of 8 mm. The change is discussed in the relative ECR [12].

FDR2. *Request a formal proposal from TC on how possible misalignments (…) between the ITk and accelerator will be handled.*

Discussed inside ECR [12].

FDR3. *Work out the kinematics interface between different ITk systems. A full calculation model for the full ITk support chain (…) shall be carried out.*

See Section 5, where the integrated model of all the relevant ITk systems is treated.

FDR4. *Clarify the CTE of the OC (…), expected short-term temperature variations of the OC (…) and resulting thermal deformations (…)*

See Section 5.6, where the thermal deformations during cooldown and due to the operative temperature variations (short and mid-term) were threated.

FDR5. *More generally, thermal deformation calculations on the OC should be done studying different thermal load conditions (…)*

The assumptions of Section 5.6 seems conservative enough to ensure that with the current design the short and medium term stability would be satisfied with reasonable temperature variations across the detector.

FDR6. *Verify thermal bridges through OC support points*

Calculations were performed. They show that this is not a problem. Results will be presented at the review.

FDR7. *The current design of the thermal barrier consists of heaters around the OC; the consequences of heater failures and power losses, and system reliability should be assessed. The requirement of thermal neutrality towards the Liquid Argon detector should be understood and taken into account as well.*

See **A6**.

FDR8. *Show calculations (or test results) on OC laminate stresses, on flanges, stiffeners and OC support pads*

Results are provided in Section 5, for the most dangerous scenario for the detector (lifting). The report also provides the evaluation of the IRF for the detector when only few interlinks are active. The results will be corroborated in the future by an experimental tests of the most solicited region.

FDR9. *Update the OC Design Report to describe the OC support strategy, taking into account that the support is based on 4 rollers per side and weight is assumed to be equally distributed, which may not fully represent real conditions. (…) include the effects (…) of some possible misalignment (…).*

This document is uncontrolled when printed. Check the EDMS to verify that this is the correct version before use

The misalignment was studied in Section 5.8, where the two extreme configurations were considered: missing lateral and missing central roller.

FDR10. *Control that the lifting interface of the OC is compatible with the lifting tool and process constraints during lifting.*

The lifting interface compatibly was verified with TC. The lifting accelerations were applied to the FE model, and results are reported in Section 5.10.

FDR11. *Assess transport and installation loads (…)*

The lifting/landing, which constitutes the only dangerous load during transport, was studied in Section 5.10.

FDR12. *Show calculations on the strength and buckling margins for the (…) IWV (…)*

Responsibility of TC.

FDR13. *Selected sealing techniques must be lab-tested and validated against clear leak-rate specifications*

Discussed in the SB design report [6].

R1. *The OC flanges proposed are made of Titanium (…)*

Flanges are now made in CFRP (CN-60).

R2. *Revise insertion rails for the strip EC's (bonded to the OC before EC insertion) to allow Barrel extraction in case it would be needed during surface assembly*

Deemed unnecessary by the project.

R3. *Bulkhead to OC connections need to be designed and validated. Bolted joints with sufficient clearances in the bolt holes seems appropriate. Use of pins (with counter-drilled holes or in-situ glued inserts) can be an option, too, if considered structurally necessary and if the Bulkheads 'never' need to be removed and reinstalled again.*

Discussed in [6].

R4. *Avoid metallic honeycomb in relation to quench forces*

For all the sandwich structures the current design uses Nomex Honeycomb.

7.1.2 Strip Endcap Global Mechanics

FDR14. *The inclined interlinks between the Barrel layers must be made quite precisely to CTE=0, otherwise they will introduce torsions to the Barrel tracker (including Pixels) at any temperature changes. Friction locking of bolted interlinks by pre-load should be validated by testing potential cause and effects of any loss of pre-tension. This design approach has never been tested at this scale, the projects needs to do prototyping to address these issues.*

The potential issues due to CTE are studied in Section 5.6, with conservative assumptions for the actual CTE values of the various components. It is important to underline that the actual measurement of this property for CFRP are very challenging.

The friction locking of bolted interlinks was instead investigated both numerically and experimentally. Results are provided in Section 4.2.

FDR15. *The design of the main structural supports between Strips Barrel and OC could be optimized. The interplay between these two large structures needs to be addressed. The connection brackets must be able to carry the loads when the OC and/or the Bulkhead are deforming at any stages of the assembly and use, including for transport and installation in ATLAS. Consider also changing the stainless steel in the support brackets to a lower CTE material, like titanium.*

This document is uncontrolled when printed. Check the EDMS to verify that this is the correct version before use

The OC to strip barrel brackets were investigated extensively. The impact of this component design on the overall performances are reported in Section 5.5. The present design is a compromise between having the most possible structure possible and avoiding important local solicitations on the OC and strip barrel flanges.

The present design uses as bracket material a Titanium alloy.

FDR16. *Assess activation vs requirements when large number of bolts are adopted for the design.*

The bolts will be in Titanium to minimize the activation. The number and size is the minimum required by the design.

FDR17. *Clarify installation issues for operators when installing staves at critical locations: clarify access, ergonomics and potential clashes.*

Will be presented at the review.

7.1.3 Strip Endcap Global Mechanics

Not treated here.

7.1.4 ITk Common Aspects

A22. *Safety aspects (…).*

Documents will be produced by PRR.

A23. *The ITk Grounding and Shielding policy (EDMS AT2-I-EP-0001) implementation was clearly presented; the ITk Faraday cage is defined by the outer wall of the OC and beampipe as the inner wall. The OC CF structure is not thick enough and needs Cu cladding applied. Present the partial tests that can validate the chosen G&S implementation strategy.*

Discussed in Section 2.3.3.

A24. *Services trays: provide further details of the design and envelope compliance, and design validation by testing the leak tightness at PP1; provide evidence that no cooling is indeed required for electrical services, address possibility of adding lines for improved flushing of environmental gas to avoid local condensation, and/or making the service trays structures open for gas flow and diffusion.*

Service trays shall be perforated.

A25. *Many results were shown from individual CAD models and FEA of the different structures. It is necessary to produce an overall global model of the full ITk support structure (including OC, SB, Strip Endcap and Barrel with PST) to understand all of possible issues and dependencies.*

FEA model results were shown trough Section 5. An integrated CAD model was produced.

A26. *At system level, support deflection (and bolted connection compliance) for the overall sag of the Barrel Strip structure and connected elements, as the PST and the Pixel, should be assessed. Calculations of stress levels (not only deflections and frequencies) for all assembly, main structural elements and detailed connections (not just for bracket supports to the OC) should be presented.*

See Section 3 for a discussion of the OC/EC interface, Section 4 for a discussion of the Strip Barrel interfaces (interlink and flanges, SB to Pixel), and Section 5 for a discussion of the interfaces between OC and Strip barrel.

A27. *Clarify if stress-strain induced effects on the Barrel Strip Structure and Staves appear during insertion of the EC's into the OC.*

Discussed in the review.

A28. *There is a dependence of the overall designs presented in this review (OC, SB, Strip Global Mechanics) on uncertainties in the Pixel services design, including total Pixel tracker weight, loading of PST during insertion, and of course the Pixel inner/outer PP1 design (volume, mass, etc.). It should*

This document is uncontrolled when printed. Check the EDMS to verify that this is the correct version before use

be understood how these dependencies will be addressed by the Pixel team on the timescale of the FDR for the SB where all ITk global and Strip global mechanics issues will be again discussed and presented for validation.

The dependence of the design to the Pixel tracker weight and design was studied in Section 4. The structure design will be optimized again when the Pixel design will be finalized.

A29. *The analysis of the overall global model of the full ITk support structure and upcoming work on prototypes may reveal that some specifications are not met (some FEA results presented show already small margins to the deflection required with quite optimistic modeling assumptions). Compensatory measures should then be addressed. Those measures should exclude additional attachment points to the OC in order to avoid any further constraints transferring forces and deformations from the OC to the Barrel Strips.*

The model analysis shows that the specifications are met. The design went through a number of iterations to achieve this result. The modelling assumptions of Section 3 were mostly confirmed by the results from the integrated model (Section 5).

7.2 Reccomendations from FDR follow-up (June 2019)

FDR18. *Mounting brackets - it would be nice to see prototypes and test them to failure.*

The prototypes are planned

FDR19. *Test long-term behavior of interlinks (preload loss with time)*

The interlinks bolts preload was measured as a function of time and temperature cycles. No significant reduction was found within the available time. Results are provided in Section 4. It is, however, important to notice that the FE model does not show a decrease in the stability of the detector with a decrease of the bolt preload.

7.3 Result Summary

The results from the previous sections are summarized in Table 11. The table also shows the relative requirement from [3] and section where the model results are studied in this document.

This document is uncontrolled when printed. Check the EDMS to verify that this is the correct version before use

Table 11 Results and performances summary, with reference to the section from this document and the actions from the FDR report.

Section		Load Case		Actions	Requirement					Performance			
#	*Title*	*#*	*Name*	*Id*	*Type*	*R (um)*	*Phi (um)*	*Z (um)*	*Other*	*R (um)*	*Phi (um)*	*Z (um)*	*Other*
5.5	Gravity Sag	DC2	OC Bracket Study	A15	N.A.				2 mm				0.66 mm
5.6	Thermal Contraction Analysis	C16	Cooldown	A3, A4, A5, A14	Positioning	Assembly Tolerance				138	73	353	
5.6	Thermal Contraction Analysis	C17	Op. Thermal ±1 K	A3, A4, A5, A14	Short Term Stability	20	2	20		2.3	1.2	5.9	
5.6	Thermal Contraction Analysis	C17	Op. Thermal ±3 K	A3, A4, A5, A14	Medium Term Stability	50	5	50		6.9	3.65	17.7	
5.7	Moisture Study	C16	Cooldown	A3, A4, A5, A14	Positioning	Assembly Tolerance				360	190	650	
5.8	Alignment Study: Missing Roller Scenario	DC3	Missing Roller	A9	Alignment				>250 µm				>300 µm
5.9	Modal Analysis	C18	Op. Dynamic	A3, A4	RMS Stability	20	2	20		<1	<1	<1	
5.10	Strength Verification	C12	Lifting	A3, A10	IRF				0.5				0.20
5.10.1	Missing Interlinks Scenario	DC1			IRF				0.5				0.22

This document is uncontrolled when printed. Check the EDMS to verify that this is the correct version before use

8 REFERENCES

[1] "Functional requirements for VI interfaces with ITK detector | Document AT2-IC-ES-0001 (v.4)".
[2] A. Smith, "ATL-IP-ER-0008 v.1 PST Heater System".
[3] "ATU-SYS-ES-0027 (v.1) - Alignment and positioning requirements for the ATLAS phase II tracker." .
[4] "AT2-IG-ES-0001 (Outer Cylinder Specification)".
[5] "ATLAS ITk Strip Barrel Design Report".
[6] "Structural Bulkhead Design Report | Document AT2-IG-ER-0002 (v.1)".
[7] E. G. Wolff, *Introduction to the Dimensional Stability of Composite Materials*. DEStech Publications, Inc, 2004.
[8] P. Kanouté, "Etude du comportement hygromécanique de matériaux composites à matrice polymérique: Application à l'analyse de la stabilité dimensionnelle de structures de détecteurs de particules," 1999.
[9] A. Poenninger and B. Defoort, "Determination of the coefficient of moisture expansion (CME)," *Eur. SPACE AGENCY-Publ.-ESA SP*, vol. 540, pp. 567–572, 2003.
[10] "Integrated Model - Load Register | Document AT2-IG-EN-0001 (v.1)".
[11] "Report FDR ITk Common and Strip Global Structures | Document ATC-R-MR-0012 (v.1)".
[12] "Outer Cylinder Radius Engineering Change Request | Document AT2-IG-EC-0001 (v.1)".

This document is uncontrolled when printed. Check the EDMS to verify that this is the correct version before use